



PROGRAMME OF  
THE EUROPEAN UNION



# Validation Report: Third Update

SERVICES SUPPORTING THE EUROPEAN  
ENVIRONMENT AGENCY'S (EEA)  
IMPLEMENTATION OF THE COPERNICUS  
EUROPEAN GROUND MOTION SERVICE –  
PRODUCT VALIDATION.



Date: 02/06/2025

Doc. Version: **3.0**

Kongens Nytorv 6  
1050 Copenhagen K  
Denmark  
Tel.: +45 336 7100  
Fax: +45 3336 7199  
[eea.europa.eu](http://eea.europa.eu)



## Document Control Information:

<b>Document Title</b>	EGMS Validation Report
<b>Project Title</b>	Services supporting the European Environment Agency's (EEA) implementation of the Copernicus European Ground Motion Service – Product validation.
<b>Document Authors</b>	Fifamè Koudogbo, Malte Vöge, Joana Esteves Martins, Daniel Raucoules, Marcello de Michelle, Filippo Vecchiotti
<b>Project Owner</b>	Lorenzo Solari
<b>Project Manager</b>	Fifamè Koudogbo
<b>Validation consortium</b>	Product validation is performed by the validation consortium led by Sixense, in partnership with NGI, TNO, BRGM, GeoSphere, and Terrasigna. Data suppliers are CNR-IREA, CSIC-IGME, CNIG, IGN, Geopartner, DTU, CGS, and LNEG.
<b>Document Code</b>	D7.3_Validation_Report.docx
<b>Document Version</b>	3.0
<b>Distribution</b>	Public
<b>Date</b>	02/06/2025

## Document Approver(s) and Reviewer(s):

Name	Role	Action	Date
Lorenzo Solari	Project owner	Approved	02/06/2025

## Document history

Revision	Date	Created by	Short description of changes
Draft	07/04/2025	Fifamè Koudogbo	Draft version
Final	27/05/2025	Fifamè Koudogbo	Final version



# Content

Document Control Information:.....	2
Document Approver(s) and Reviewer(s): .....	2
Document history .....	2
<b>1 Executive summary.....</b>	<b>5</b>
<b>2 Introduction .....</b>	<b>7</b>
2.1 European Ground Motion Service.....	7
2.1.1 2019-2023 update – the quality control protocol.....	8
2.1.2 Validation – Additional point density evaluation.....	9
2.2 Principles of the validation.....	12
2.3 Methodologies for external validation.....	13
2.3.1 EGMS Consistency and Accuracy .....	13
2.3.1.1 <i>Validation by comparison with GNSS data.</i> .....	13
2.3.1.2 <i>Validation by comparison with in-situ data .</i> .....	15
2.3.1.3 <i>Evaluation of XYZ and time series with CRs.</i> .....	16
2.3.1.4 <i>Validation sites</i> .....	16
2.3.2 EGMS Applicability and Usability .....	19
2.3.2.1 <i>Validation by comparison with other Ground Motion Services (GMS)</i> .....	19
2.3.2.2 <i>Validation by comparison with inventories of phenomena.</i> .....	20
2.3.2.3 <i>Validation by consistency checks with ancillary data.</i> .....	21
2.3.2.4 <i>Validation sites</i> .....	22
<b>3 Results – Consistency and Accuracy .....</b>	<b>26</b>
3.1 Velocity and time series validation by comparison with GNSS.....	26
3.1.1 La Palma (Spain) .....	26
3.1.2 Gran Canaria (Spain).....	30
3.1.3 Guadalentín basin, Lorca Region (Spain).....	34
3.1.4 Jutland peninsula (Denmark) .....	38
3.2 Velocity and time series validation by comparison with in-situ data .....	43
3.2.1 Lorraine (France) .....	43
3.2.2 Turow (Poland).....	47
3.2.3 Guadalentín basin, Lorca Region (Spain).....	50
3.2.4 Navis (Austria) .....	53
3.3 Height and position validation by comparison with CRs.....	57
3.3.1 Thyborøn (Denmark) .....	57
3.3.2 Indre Nordnes, Jettan and Gámanjunni (Norway) .....	61
<b>4 Results - Applicability and Usability Validation .....</b>	<b>66</b>
4.1 Landslides .....	66



4.1.1	Comparison with other GMS.....	66
4.1.1.1	<i>Aosta Valley (Italy)</i> .....	66
4.1.1.2	<i>Tuscany (Italy)</i> .....	68
4.1.2	Comparison with inventories of phenomena .....	70
4.1.2.1	<i>Alpes Maritimes (France)</i> .....	70
4.1.2.2	<i>Rules reservoir (Spain)</i> .....	72
4.1.2.3	<i>Arcos de la Frontera (Spain)</i> .....	74
4.2	Mining and post-mining .....	75
4.2.1	Comparison with inventories of phenomena .....	75
4.2.1.1	<i>French inventory (Lorraine region)</i> .....	75
4.2.2	Comparison with geo-information.....	76
4.2.2.1	<i>La Unión (Spain)</i> .....	76
4.2.2.2	<i>Silesia (Czech Republic)</i> .....	80
4.3	Urban.....	82
4.3.1	Comparison with other GMS.....	82
4.3.1.1	<i>Thyborøn (Denmark)</i> .....	82
4.3.1.2	<i>Po delta (Italy)</i> .....	85
4.3.2	Comparison with geo-information.....	89
4.3.2.1	<i>Oslo (Norway)</i> .....	89
4.3.2.2	<i>Tagus Valley (Portugal)</i> .....	94
4.4	Groundwater exploitation.....	97
4.4.1	Comparison with geo-information.....	97
4.4.1.1	<i>Lorca (Spain)</i> .....	97
4.5	Volcanism .....	98
4.5.1	Comparison with other GMS.....	98
4.5.1.1	<i>Etna Volcano (Italy)</i> .....	98
5	<b>Conclusion.....</b>	<b>101</b>
6	<b>References.....</b>	<b>102</b>
7	<b>List of Abbreviations .....</b>	<b>104</b>
8	<b>List of Figures.....</b>	<b>105</b>
9	<b>List of Tables.....</b>	<b>109</b>



# 1 EXECUTIVE SUMMARY

Since 2022, the European Ground Motion Service (EGMS) has served a wide user community by providing unique, calibrated, and harmonised ground deformation products at the Pan-European level within the Copernicus Land Monitoring Service (CLMS) portfolio. This document reports the results of the validation performed for the 2019-2023 EGMS update.

The validation activities, performed across various sites in Europe, aim to measure the agreement between EGMS and reference data (ground-based and Earth Observation). Two key criteria are considered: (1) Consistency and Accuracy, and (2) Applicability and Usability. The Consistency and Accuracy assessment focuses on comparing EGMS measurement point (MP) velocities and time series with GNSS and in-situ data, as well as evaluating geocoding accuracy and time series behaviour of EGMS points in relation to corner reflectors (CR). The Applicability and Usability assessment examines the qualitative consistency of EGMS measurements with other Ground Motion Services (GMS), inventories of phenomena, or geo-information. This is achieved using the concept of Active Deformation Areas (ADAs) derived from EGMS MPs.

Overall, this report demonstrates that EGMS products meet the required technical specifications and are suitable for supporting various applications related to ground motion monitoring and analysis:

- The EGMS Basic/L2a and Calibrated/L2b products have proven effective in delineating ground motion polygons representing landslide phenomena. For example, in the Alpes Maritimes (France), Rules and Arcos de la Frontera (Spain), approximately 50% of EGMS ADAs intersect inventory polygons. In three regions of Italy, EGMS results are compared with other GMS, and although some differences are found (e.g., spatial overlap between moving areas), all major landslide areas are identified, and the time series show an overall good agreement. The geo-positioning and height of EGMS MPs are also assessed with CRs and GNSS installed in test sites located in mountainous areas of Norway. The results show, for each CR, a good correlation of velocity estimation between EGMS and GNSS measurements.

Despite the low density of points in some areas due to vegetation cover, EGMS can detect landslides and accurately follow their deformation trends. Furthermore, in the Alpes Maritimes, more than half of the potential landslides identified by EGMS are not recorded in the up-to-date national landslide inventory, particularly slow-moving landslides, presenting interesting perspectives for improving national inventories.

- EGMS is also capable of detecting motion induced by large-scale active mining and post-mining effects, as evidenced by the comparison with piezometric data in the Turow mine area. In La Union, Spain, EGMS moving points location show significant overlap with mine waste sites; however, this is not true for tailings, suggesting that EGMS can help differentiate the state of activity of tailings.
- EGMS results' consistency and accuracy are further assessed in cases of groundwater over-exploitation. In Lorca, Spain, EGMS-derived velocity and time series are compared to GNSS, piezometric level information, and other geo-information. Despite the technique's limitations in capturing strong non-linearities, EGMS products demonstrate high-quality results and accuracy in velocity estimation, reaching less than 1 mm/year when compared with GNSS. EGMS also effectively follows the seasonality induced by groundwater exploitation in water table oscillations. A strong correlation has been identified between subsidence rates and the increasing thickness of the soft-soil layer in the Lorca case.
- Additionally, EGMS offers high MP density in urban areas, effectively capturing significant man-made construction settlements, as demonstrated near the Oslo central station in



Norway. In Thyborøn, Denmark, the coastal area is affected by subsidence; velocity offsets of less than 1 mm/year are observed when comparing EGMS with data produced by the Technical University of Denmark. In the Tagus Valley, Portugal, several ADAs align with fault lines that act as geological barriers and produce favourable conditions for detecting displacements (e.g., groundwater exploitation).

- Finally, EGMS results are compared with GNSS in La Palma (Spain) and with other GMS products in Etna. Given the occurrence of a volcanic eruption in La Palma in 2021, these comparisons encompass challenging cases. Results show that despite the complexity of the ground motion dynamics, the EGMS Basic/L2a products perform well, showing an average velocity difference of 0.8 mm/year compared to GNSS across all stations and demonstrating a good ability to replicate the displacement signatures observed in the GNSS time series. It is worth highlighting that, given the non-linear nature of displacements associated with volcanic eruptions, Basic/L2a products have proven to be the most reliable option for comparison with in-situ data. In the case of Etna, although disparities exist between EGMS and IREA products, the correlation between the datasets remains strong for such a dynamic volcanic system and a relative velocity difference of about 21% was observed. Overall, the analysis demonstrates the EGMS's capability to reliably map displacements under volcanic challenging conditions.



## 2 INTRODUCTION

Congalton and Russell (2001) state that validation is a crucial part of mapping projects using Earth Observation data. By that statement, the validation exercise described in this report measures the agreement between reference data (ground-based and Earth Observation) and the EGMS. This report refers to the **2019-2023 EGMS update**.

The validation exercise is conducted in a set of areas distributed throughout Europe. The datasets used in this validation exercise are detailed in [D3-Validation Data Collection](#) along with the environmental and geological characteristics of each site as reported in [D5-Validation Areas](#).

The EGMS validation aims to achieve specific goals based on key concepts:

- It investigates the **Consistency and Accuracy** of the product and assesses whether its quality meets technical specifications across various domains and applications, and if the quality level is adequate to support these applications. It also verifies the conclusions of the [EGMS Quality Assurance and Control Report](#).
- It verifies the **Applicability and Usability** of the data for different applications according to the *initial user requirements* and with respect to the *fields of application* foreseen by the [EGMS Product Specifications](#) and the [EGMS End User Requirements](#) documents.
- It ensures data products are complete, consistent, and accurate.

It is important to note that the validation of EGMS products involves comparing datasets of different nature and sources. Consequently, complete agreement is unlikely, and any observed discrepancies may not indicate a quality issue.

The present document reports the outcomes of the validation activities and is organised into five main sections, structured as follows:

- The remainder of Section 2 introduces the EGMS project and evaluates the performance of the 2019-2023 update, focusing on measurement point (MP) density. The second part of the section provides a concise overview of the methodology and processes implemented for EGMS validation, summarizing the information from the [D6-Validation Methodologies](#) document.
- Section 3. Results – Consistency and Accuracy presents the results of the validation activities assessing the consistency and accuracy of key parameters, including velocity, time series, and positioning. The findings are organized by validation methodology and validation site.
- Section 4. Results - Applicability and Usability Validation evaluates the applicability and usability of EGMS products. The results are organized by geohazard type, with the corresponding validation sites structured accordingly.
- Finally, Section 5. Conclusion provides a summary of the key findings and main results presented in the previous sections.

### 2.1 European Ground Motion Service

Since 2022, the European Ground Motion Service (EGMS) has supported a broad user community by providing unique, calibrated, and harmonised ground deformation products across Europe. These products are delivered as part of the Copernicus Land Monitoring Service (CLMS) portfolio.



EGMS comprises continental-scale, homogeneous maps of ground motion in mm-per-year precision measuring ground and infrastructure displacements, including those caused by landslides, subsidence and tectonics. The underlying methodology utilises state-of-the-art SAR Interferometry techniques, multi-interferogram time series analysis of high-resolution Sentinel-1 data, to reduce noise and derive ground displacement and average velocity at specific MPs. EGMS outputs are made available to users in the form of three products:

- *Basic/L2a* provides InSAR displacement data in the satellite Line-of-Sight (LOS), with annotated geo-localization and quality measures for each MP.
- *Calibrated/L2b* is considered the main EGMS product, as it serves the needs of most users. It is fundamentally the same as the Basic product but enhanced by referencing the InSAR MP displacement values to a model derived from Global Navigation Satellite System (GNSS) time series data, thereby converting the InSAR measurements to absolute.
- *Ortho/L3* exploits the information provided by ascending and descending orbits of the EGMS Calibrated to derive two additional layers: one representing purely vertical displacements (EGMS Ortho Vertical), and the other capturing purely east-west displacements (EGMS Ortho East/West).

Please refer to [EGMS Product Specifications](#) for detailed information.

From both a user perspective and given the Pan-European scale of the service, harmonization of EGMS products is mandatory and indispensable. For this reason, each EGMS product undergoes a rigorous quality control protocol to ensure consistency and optimal quality. More information is provided in the [EGMS Quality Assurance and Control Report](#).

### 2.1.1 2019-2023 update – the quality control protocol

Quality control (QC) within EGMS is critical to the success of the service. In particular, the main scope of the QC protocol is to guarantee reliability, i.e., to deliver measurements which fully meet the expected accuracy and can be trusted by users, and are consistent in terms of MP density, accuracy, precision, and calibration.

To provide the user with a product that meets EGMS specifications, quality assurance and control activities are performed by the production consortium. The applied QC protocol considers and respects the different nature and characteristics of the Basic, Calibrated and Ortho products to accurately evaluate their quality and fitness for purpose. Table 2.1 summarises the relevant quality criteria, as extracted from the EGMS Quality Assurance and Control Report for the 2019-2023 EGMS update, which is available [here](#).

Table 2.1: Quality criteria for the QC checks (see [EGMS Quality Assurance and Control Report](#)).

QC step	Test Criteria	Product	QC passed conditions
MP density	MP density for specific CLC18 ( <a href="#">Corine Land Cover 2018</a> ) classes. The densities will be evaluated on areas sufficiently large in order to guarantee an adequate statistic per each CLC18 class.	Basic/L2a	<ul style="list-style-type: none"><li>• class 1.1.1: &gt; 5000 MP/km<sup>2</sup></li><li>• class 1.1.2: &gt; 1000 MP/km<sup>2</sup></li><li>• class 1.2: &gt; 1000 MP/km<sup>2</sup></li><li>• class 3.3: variable depending on the number and correctness of the polygons of these classes</li></ul>
Noise	Root Mean Square (RMSE) with respect to the cubic + sinusoidal model is calculated for each MP.	Basic/L2a	Nominally ≤5 mm. An RMSE >5 mm may be required in rare circumstances where the model does not sufficiently represent the actual deformation

Formatting	Ensure common standards used throughout for e.g., units, scaling, tiling, etc.	Basic/L2a Calibrated/L2b Ortho/L3	
------------	--	---	--

## 2.1.2 Validation – Additional point density evaluation

As part of EGMS product validation, an evaluation of the MP density across different land cover types is performed. The methodology complements the internal QC by targeting a more refined land cover/land use (LC/LU) classification (Urban Atlas) with the scope of proposing a target-based (urban areas) evaluation of point density. The evaluation considers 12 urban areas and their surroundings, strategically distributed across different latitudes in Europe to enhance statistical representation. LC/LU distribution is based on the 26 classes defined by the [Urban Atlas](#). Figure 2.1 shows the 12 selected sites along with their LC/LU coverage according to Urban Atlas 2018 classification. Additionally, Figure 2.2 presents a diagram illustrating the distribution of LC/LU types across the considered sites, showing a higher proportion of agricultural land and forests.

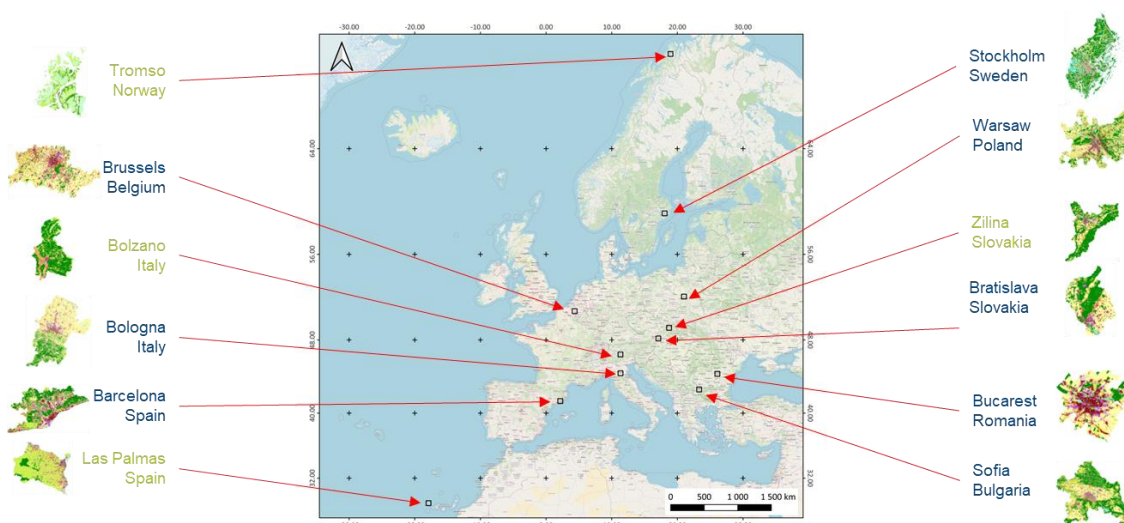


Figure 2.1: Land cover and land use classes for Urban Atlas 2018 at the 12 sites selected to verify MP density.

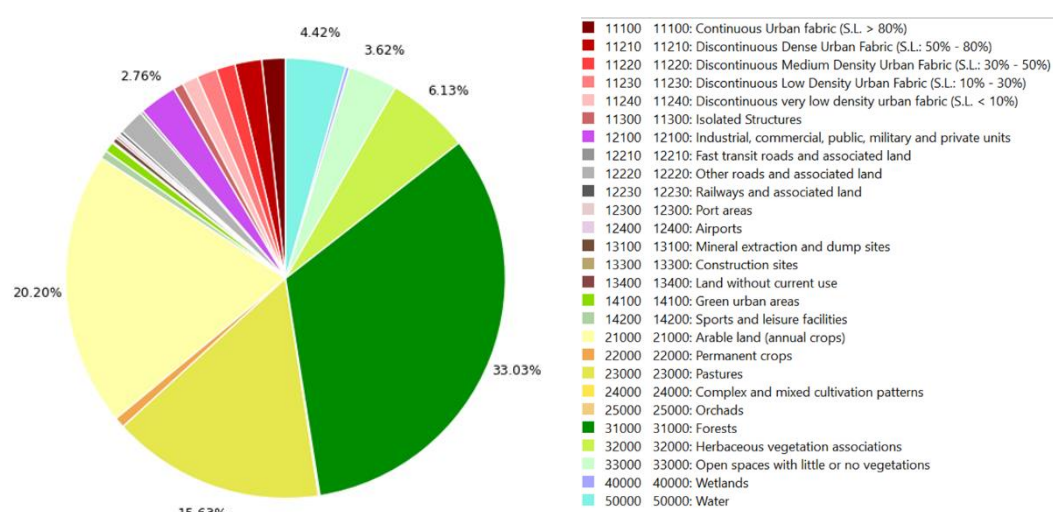


Figure 2.2: Global land cover type distribution over the 12 sites selected to verify MP density.

The primary activity aims to verify that EGMS product specifications for MP densities are met by using a different LC/LU product. The tests performed are suitable for both Basic/L2a and Calibrated/L2b products, while Ortho/L3 product is not checked because of its resampling nature. Figure 2.3 confirms that all minimum requirements are met for the third EGMS update, with performance significantly exceeding expectations in certain categories.

The observed MP distribution further confirms that densities adapt to surface properties; artificial surfaces, such as the urban built-up environment, exhibit the highest point densities, while surfaces characterized by frequent changes, such as agricultural areas and forests, yield lower MP densities.

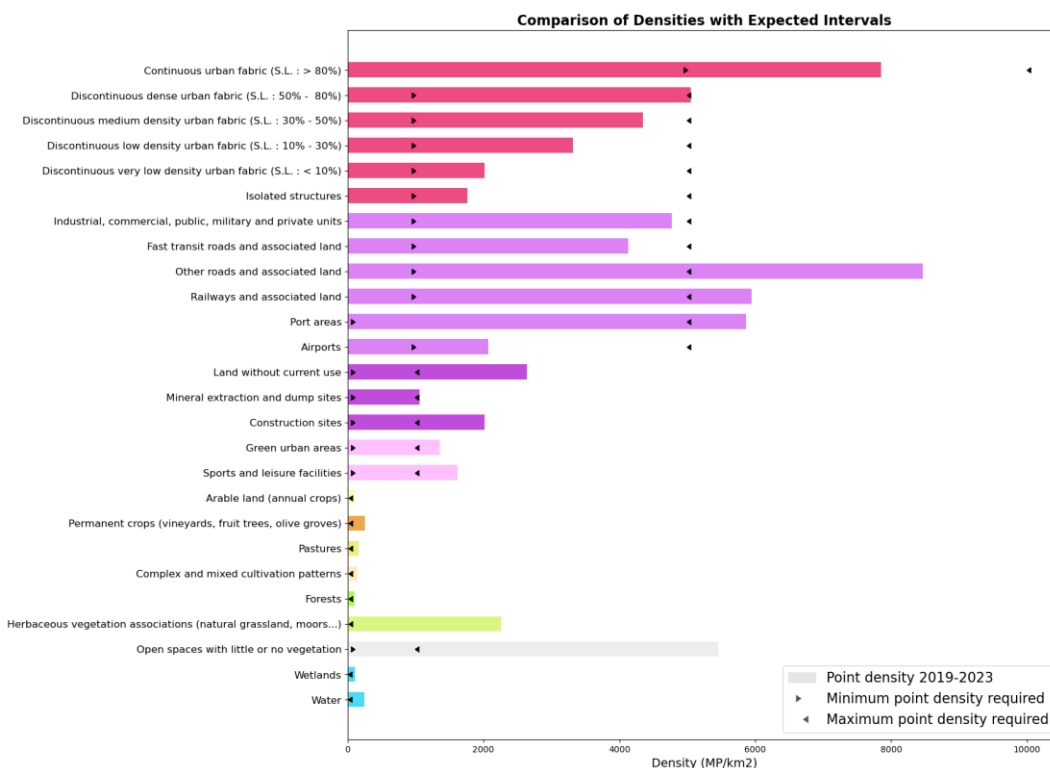


Figure 2.3: MP density over the 12 sites selected for specific UA18 classes based on the Basic/L2a and Calibrated/L2b products.

The diagram of Figure 2.4 shows the differences in density for the 26 Urban Atlas classes represented for both ascending and descending orbits. The figure reveals that point densities are generally higher in the ascending orbit, except for permanent crops. This may be attributed to the acquisition geometry and conditions, with the ascending path occurring in the late afternoon and the descending path in the early morning over Europe.

In Figure 2.5, the EGMS 2019-2023 update MP densities per class are compared to the [2018-2022 release](#). To simplify the analysis, the Level 2 classes of the Corine Land Cover are used to group the Urban Atlas nomenclature. MP density is substantially increased between the two updates, even though similar duration periods are considered. The density in categories such as "Permanent crops" and "Heterogeneous agricultural areas" has increased by up to 40%.

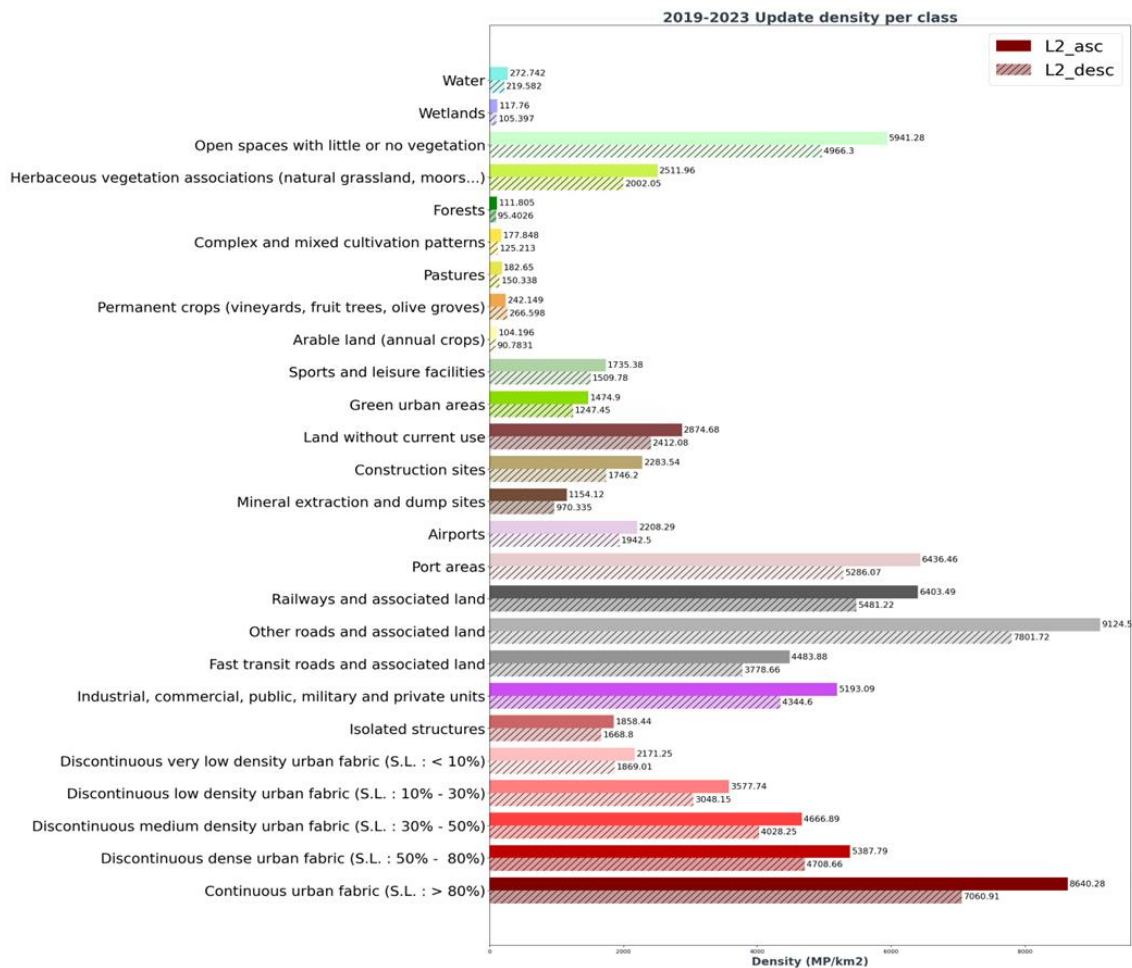


Figure 2.4: EGMS 2019-2023 results – Comparison of ascending and descending Basic/L2a MP densities for the Urban Atlas classes over the selected 12 sites.

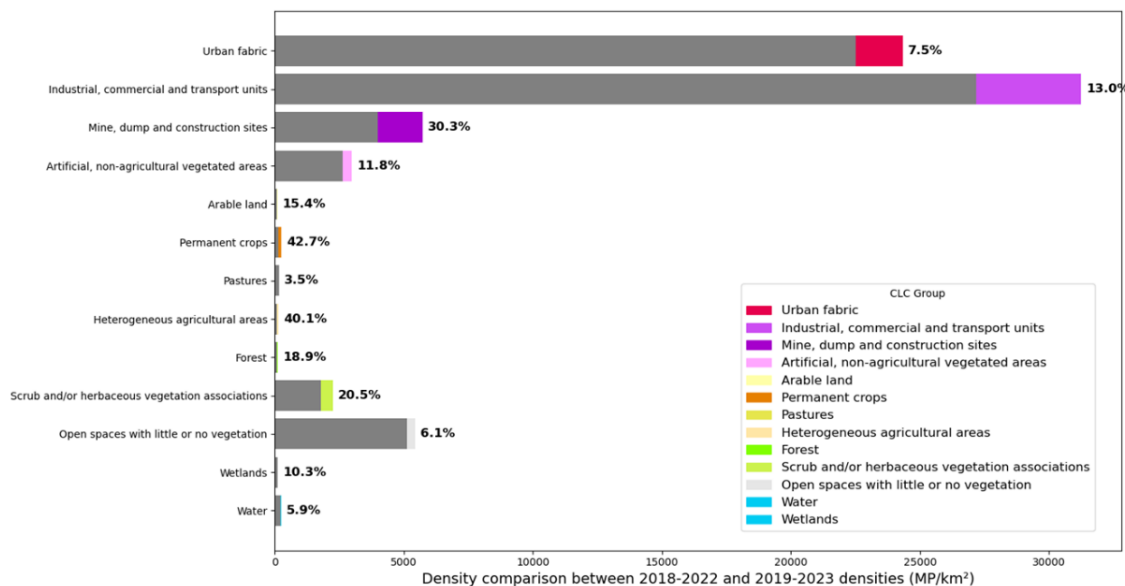


Figure 2.5: EGMS MP density for Basic/L2a and Calibrated/L2b products across the 12 selected sites. The previous release 2018-2022 density values (grey) with the increase percentages in the current update (indicated by coloured bars and numerical labels). LC/LU classes from the Urban Atlas are grouped according to the 2<sup>nd</sup> level of the CLC nomenclature.

## 2.2 Principles of the validation

The aim of the validation is to assess the EGMS products based on **two key criteria: Consistency and Accuracy, and Applicability and Usability**.

Figure 2.6 summarises the main components of the validation process.

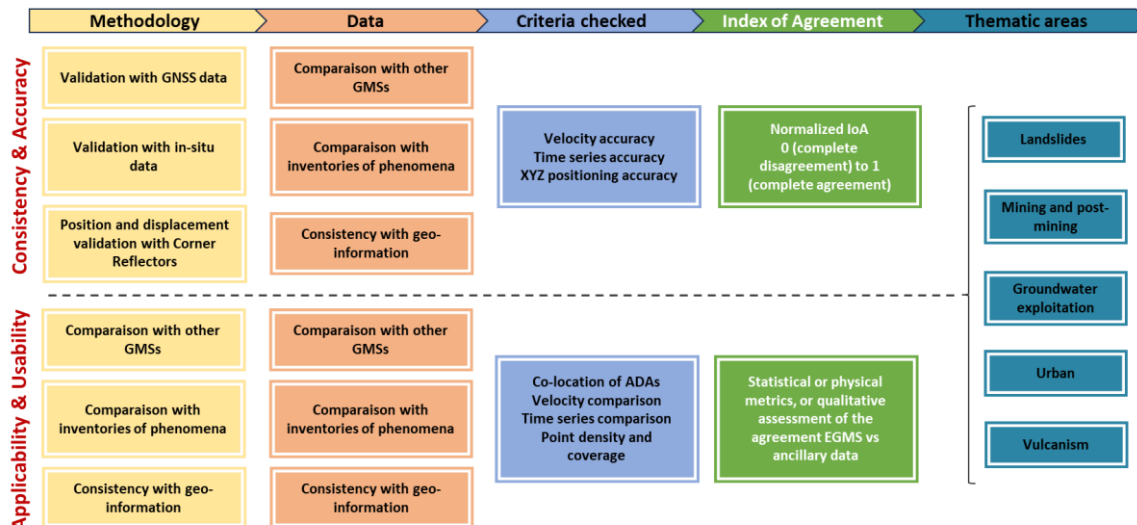


Figure 2.6: Overview of the main components of the EGMS validation framework.

Four different principles are followed for each of the key validation criteria, according to Figure 2.6:

- Methodology

Various procedures have been implemented as part of the validation process. Those procedures ([D6-Validation Methodologies](#)) use as inputs the EGMS products and independent datasets available for each selected validation sites ([D3-Validation Data Collection](#) and [D5-Validation Areas](#)).

- Data

In-situ data are essential for the validation of EGMS products. In case of time series datasets, such as levelling, data were collected to ensure significant temporal overlap with the EGMS time series (aiming for more than 85%). The properties of these datasets, including their licenses, formats, and coverage, are documented in [D3-Validation Data Collection](#) and [D5-Validation Areas](#).

- Validation criteria

Various criteria are used to compare EGMS products and validation datasets. For instance, certain methods focus on analysing velocity and displacement rates, while others evaluate the XYZ positioning of the EGMS MPs or their density. Activities assessing the usability of the EGMS product involve, in some cases, expert-based thresholds and qualitative assessments based on available ancillary data. The validation criteria are outlined in [D6-Validation Methodologies](#).

- Index of Agreement (IoA)

The concept of the IoA, documented in Section 2 of [D6-Validation Methodologies](#), was defined to ensure the inter-comparability and reproducibility of the EGMS external validation. For Consistency and Accuracy checks, the validation outputs are normalized IoAs ranging from 0 (complete disagreement) to 1 (complete agreement). For Applicability and Usability checks, IoAs are either expressed as statistical or physical metrics, or qualitative assessments based on expert

interpretation of the agreement between EGMS and ancillary data. Along with expert knowledge and literature, IoAs aid in understanding the applicability of EGMS ground motion data.

The reproducibility of the validation workflows is ensured by exploiting the Jupyter Notebook environment and scripts, which convert methodologies into code using validation site data as inputs. The Notebooks will be published in Q3 2025.

The methodologies applied to assess the two key validation criteria are described in the following subsection.

## 2.3 Methodologies for external validation

### 2.3.1 EGMS Consistency and Accuracy

Comparisons with three types of external data were conducted to assess the Consistency and Accuracy of EGMS products. Reproducible IoAs have been derived for each validation activity. A detailed description of the methodologies is available in [D6-Validation Methodologies](#). Key aspects are summarized below.

#### 2.3.1.1 Validation by comparison with GNSS data

##### a) Objectives and validation steps

The objective is to use GNSS measurements to evaluate the displacement accuracy of EGMS MPs. EGMS velocities and time series are compared with GNSS data, and their differences are statistically analysed. The workflow outlining this methodology is presented in Figure 2.7, with each step described in detail below:

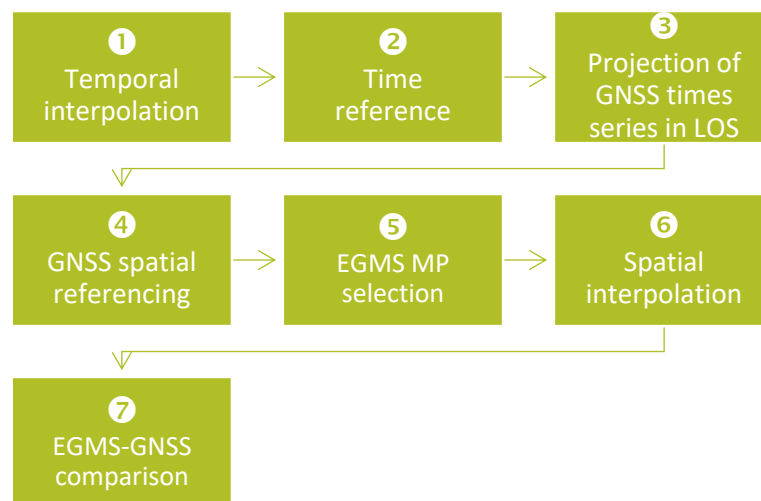


Figure 2.7: Overview of the workflow used for EGMS and GNSS data comparison.

- Temporal interpolation: GNSS time series are aligned with EGMS acquisition dates to cover the same periods. A 12-day interpolation window is used.
- Time reference: Both GNSS and EGMS time series are aligned to the same reference date.
- Projection of GNSS time series to LOS: For comparison with EGMS Basic/L2a and Calibrated/L2b products, GNSS displacement is converted to radar LOS, in accordance with the observation geometry.
- GNSS spatial referencing: For Basic/L2a data, a GNSS station is selected as a reference station for each validation site. The time series difference between the reference station and the other stations is then calculated. For Calibrated/L2b and Ortho/L3 products, velocity



differences between the GNSS reference frame and the reference frame used in the Calibrated/L2b and Ortho/L3 products (i.e., the A-EPND velocity model) are computed and subtracted from the GNSS time series.

- **EGMS MP selection:** MPs are selected to be compared with GNSS based on proximity (MPs are selected within a 100m radius from the GNSS station) and height criteria.
- **Spatial interpolation:** Spatial interpolation is done using the selected EGMS MPs at the GNSS location, with errors estimated based on MP accuracy. Double differences are applied exclusively to Basic/L2a products, as they refer to a virtual reference point. This step is unnecessary for Calibrated/L2b and Ortho/L3 products since they already use the same reference system, ETRF 2000.
- **EGMS - GNSS comparison:** The correlation between GNSS and EGMS time series is calculated, along with the standard deviation of the differences between the two. Only the overlapping segments of the EGMS and GNSS time series are considered. The BLUE model (Best Linear Unbiased Estimation) [Teunissen, 2000a, Teunissen, 2000b] is used to estimate the variance of the parameters.

### b) IoA definition

Different metrics are used to compare EGMS and GNSS velocity, time series, and seasonal signals; they are listed in Table 2.2. It is important to note that all IoA metrics are normalized across the entire spectrum of GNSS stations and product datasets to ensure an aggregated evaluation of the EGMS products.

Table 2.2: IoAs defined for the validation by comparison with GNSS measurements.

IoA	Metric calculation and interpretation	EGMS products
Time series: correlation	<u>Correlation</u> : Time series correlation (after normalization). IoA closer to 1 indicates higher correlation.	Basic/L2a, Calibrated/L2b and Ortho/L3
Overall model test (OMT) for time series	<u>Statistical test</u> : The OMT is a global check to identify inconsistencies (or outliers) between the EGMS and GNSS time series. An IoA (Index of Agreement) value of one indicates that the time series successfully passes the test, while an IoA value of zero indicates that the time series fails to pass the test.	Basic/L2a, Calibrated/L2b and Ortho/L3
Velocity differences	<u>Difference between measures</u> : Percentual difference between the EGMS and GNSS velocities. IoA values near 1 indicate stronger agreement.	Basic/L2a, Calibrated/L2b and Ortho/L3
Velocity t-test	<u>T-test</u> : Statistical test used to compare EGMS and GNSS velocities. An IoA (Index of Agreement) value of one indicates that the time series successfully passes the test, while an IoA value of zero indicates that the time series fails to pass the test.	Basic/L2a, Calibrated/L2b and Ortho/L3
Seasonality: Correlation of detrended signals	<u>Correlation</u> : Evaluated after linear trend removal (detrending). IoA values near 1 indicate stronger agreement.	Basic/L2a
Seasonality: Standard deviation of differences of the detrended signals	<u>Error</u> : Difference between EGMS and GNSS after removing linear trends. Higher IoA values (close to 1) indicate lower error.	Basic/L2a, Calibrated/L2b and Ortho/L3



<b>Seasonality: Mean of differences of the detrended signals</b>	Mean difference of detrended GNSS signals. Higher IoA values (near 1) signify less significant differences.	Basic/L2a, Calibrated/L2b and Ortho/L3
<b>Seasonality: RMS of differences of the detrended signals</b>	Root mean square of detrended GNSS signal differences. Higher IoA values (near 1) mean the difference is less significant.	Basic/L2a, Calibrated/L2b and Ortho/L3

### 2.3.1.2 Validation by comparison with in-situ data

#### a) Objectives and validation steps

This validation activity evaluates EGMS ground motion data with in-situ measurements such as levelling, piezometers, and geodetic data. The objective is twofold: to evaluate both EGMS velocities and time series.

- To compare velocities, in-situ XY measurements are converted to LOS. EGMS MPs within 50 or 100 m buffers surrounding the in-situ measurement locations are collected. The averaged velocity values of these EGMS MPs are used to evaluate the accuracy and precision of the EGMS in comparison to the in-situ measurements.
- The same pre-processing steps employed for the velocity analysis is applied to the time series data. Both EGMS and in-situ data are aggregated at intervals (6-day, monthly, yearly). Outlier and seasonality extraction assess trends, accelerations, decelerations, and seasonal variation impacts on time series comparison.
- The method proposed by Boni et al., 2016 is applied for comparison with piezometer data, expressed in the following equation:

$S = \text{Vel}_{\text{EGMS}} / \text{Vel}_{\text{piezometer}}$ , where  $S$  is the storage coefficient,  $\text{Vel}_{\text{EGMS}}$  is the minimum EGMS velocity calculated for the MPs falling inside the buffer around each station, and  $\text{Vel}_{\text{piezometer}}$  is the piezometer velocity.

Moreover,  $\Delta d = S \times \Delta h$  relation, with  $\Delta h$  representing the original time series, is used to calculate the monthly deformation rate  $\Delta d$  (for the time series) adjusted for the head of the groundwater change.

#### b) IoA definition

Different metrics are used to compare EGMS and GNSS time series, velocity, and seasonal signals, as reported in Table 2.3.

Table 2.3: IoAs defined for the validation by comparison with in-situ measurements.

IoA	Metric calculation and interpretation	EGMS products
<b>Time series/velocities correlation</b>	$R^2$ : Comparison between deformation time series (EGMS/in-situ). IoA values near 1 indicate stronger agreement.	Basic/L2a, Calibrated/L2b and Ortho/L3
<b>Time series/velocities Error</b>	Mean Absolute Error (MAE): Measures the difference between deformation time series (EGMS/in-situ). Higher IoA values (close to 1) mean lower error.	Basic/L2a, Calibrated/L2b and Ortho/L3
<b>Time series/velocities agreement</b>	Time series and Velocity agreement ( $d$ ): Time series quality metric assessing the degree of correspondence between EGMS time series and in-situ measurements. The agreement is dimensionless and ranges from 0 to 1, where a value of 1 signifies a perfect match, and a value of 0 indicates no correspondence.	Basic/L2a, Calibrated/L2b and Ortho/L3



<b>Normalized mean</b>	Combined index: an average of the three indexes mentioned above with equal weight.	Basic/L2a, Calibrated/L2b and Ortho/L3
------------------------	--	--

### 2.3.1.3 Evaluation of XYZ and time series with CRs

#### c) Objectives and validation steps

The purpose of this activity is to evaluate the precision of the EGMS time series with respect to location, height, and measured motion. The following characteristics are investigated:

- **Geo-positioning accuracy (XY):** The product specifications require the geo-positioning accuracy to be below 10 m. To verify this, GNSS local observations are used due to their high accuracy in horizontal positioning. The accurate positions of the CRs are known, and a 25-meter buffer is created around each CR to isolate all proximate EGMS MPs, followed by a meticulous selection of EGMS MPs with similar time series behaviour. Finally, the distance (offset) between each CR and its nearest MPs is calculated to verify the geo-positioning accuracy.
- **Height estimation (Z):** For this task, CRs with known heights derived from levelling campaigns are used. If these data are not available, GNSS measurements in correspondence with the CRs are considered. Differences between orthometric and geometric heights are considered negligible, given the small distances between CRs. A 100-m buffer is taken to collect all EGMS MPs surrounding each CR. Then, the relative heights of the CRs are compared with the closest EGMS MPs, using statistical testing to determine if the differences are significant, considering their corresponding standard deviations.
- **Quality of the EGMS time series:** To evaluate the quality of EGMS time series displacements, GNSS stations located at selected CR sites or levelling measurements are used. The same procedures described in “comparison with GNSS data” are applied.

#### d) IoA definition

For CRs, IoAs similar to those in GNSS time series comparisons are used to focus on time series agreement. An additional IoA assesses geo-positioning accuracy. All metrics are summarised in Table 2.4.

Table 2.4: IoAs defined for the validation by comparison with CRs.

IoA	Metric calculation and interpretation	EGMS products
<b>Time series quality and velocity of time series with CR</b>	Quality assessment of how well the EGMS time series agree with those at the CR locations.	Basic/L2a
<b>Positioning accuracy estimates</b>	Position difference: X, Y, Z accuracies or geo-positioning and height accuracies. How close the estimated EGMS heights and locations are to the measured CRs heights and locations.	Basic/L2a

### 2.3.1.4 Validation sites

The validation of EGMS products relies on a set of validation sites ([D5-Validation Areas](#)). Nine of them are used for the validation activities dedicated to EGMS product consistency and accuracy assessment. An overview of the selected sites is presented in Table 2.5 and in Figure 2.8. These locations were chosen for their broad geographic distribution and the diverse nature of the geohazards affecting them.

Table 2.5: Overview of validation sites (Consistency/Accuracy).

Methodologies Geohazards	Validation with GNSS data	Validation with in-situ data	Position and displacement validation with CR
Landslides	-	Tyrol (AT)	Indre Nordnes, Jettan and Gamanjuni (NO)
Mining and post-mining	-	Turow (PL) Lorraine (FR)	-
Urban / Anthropogenic	Gran Canaria (ES) Jutland (DK)	-	Thyborøn (DK)
Groundwater exploitation	Lorca (ES)	Lorca (ES)	-
Extra (Volcanism)	La Palma (ES)	-	-

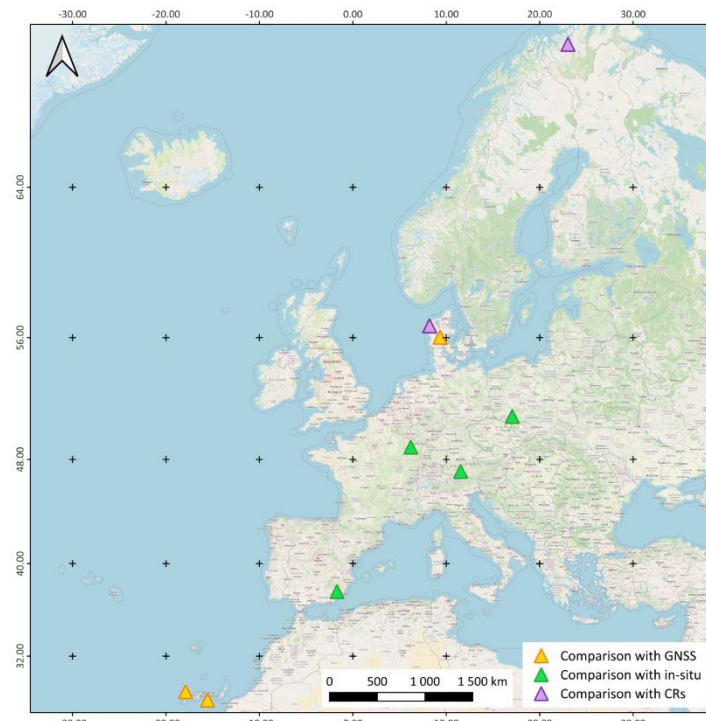


Figure 2.8: Distribution of the validation sites selected for the EGMS product consistency and accuracy assessment.

The sites are further described in subsections 2.3.1.4.1 to 2.3.1.4.3.

#### 2.3.1.4.1 Validation with GNSS data sites

The sites for validation by comparison with GNSS data are described below. Detailed information can be found in [D5-Validation Areas](#).

- The **Canary Islands** is home to over two million people and have an average population density three times higher than the rest of Spain. This archipelago is one of the major volcanic oceanic island groups of the world and has a long magmatic history, which began at the bottom of the ocean more than 40 million years ago. Sixteen historical eruptions have been documented in the Canarian Archipelago to date. The last event occurred in September 2021 in La Palma. This geological event started on September 19th and concluded on December 13th, 2021, leaving a lasting impact on the island's physical

landscape. Over 3,000 buildings were destroyed and more than 7,000 people were forced to evacuate their homes. For the project, **Gran Canaria** and **La Palma** have been chosen as validation sites.

- The Guadalentín basin in southeastern Spain is one of the driest regions of Europe. Continuous groundwater pumping, mainly for agricultural use, led to a decrease in the piezometric levels of more than 200m since 1975. This overexploitation of the aquifer has led to considerable land subsidence in the area. **Lorca**, on which validation activities focus, has been extensively studied using different techniques such as GNSS and InSAR. The accumulated vertical deformation close to Lorca is around 24 cm, with an even greater subsidence in the centre of the basin, reaching up to 12 cm/year.
- **Jutland** is a large peninsula that extends over the mainland regions of Denmark: It separates the North and Baltic seas and borders Germany to the south. Along the west coast, the sedimentary sequence is mostly composed of sand and clay. Although Denmark is mainly uplifting by around 1 mm/year due to the post-glacial, large parts of the coastal region are subsiding due to local phenomena; for example, the harbour in Esbjerg registers active subsidence and other subsidence phenomena have also been reported in the town of Thyborøn. Jutland area is affected by such phenomena and has been monitored with GPS stations since around the year 2010.

#### 2.3.1.4.2 Validation with in-situ data sites

The sites for validation by comparison with in-situ data are described below. Detailed information can be found in [D5-Validation Areas](#).

- **Freyming-Merlebach**, located in the **Lorraine** region of France near the German border, faced growing concerns due to uplifts caused by natural water filling in formerly exploited underground coal mines (post-mining).
- The mining operations in **Turow**, the second largest active coal mine in Poland, not only deplete water supplies but also trigger subsidence in the border areas of Germany and Czech Republic. An extensive network of water boreholes has been employed to evaluate the effectiveness of the EGMS for monitoring the impacts of Turow's mining activities in the vicinity of the open-pit lignite mine near the Czech Polish border.
- **Lorca**, in the Guadalentín basin is the last site considered for validation by comparison with in-situ data. It has been described in subsection 2.3.1.4.1.
- **Navis** is a municipality in the district of Innsbruck-Land in the Austrian state of Tyrol. Deep-seated landslides (often also referred to as deep-seated gravitational slope deformations, DSGSDs) are widespread phenomena in the province of Tyrol. Since 2012, GPS surveys conducted in Kerschbaumsiedlung, a residential estate complex situated in the western part of Navis, have indicated that the slope is undergoing movement of up to 3 cm per year. To analyse the process and causes of this slope movement and to enable the implementation of effective remediation measures, extensive testing and monitoring activities were carried out between 2012 and 2014 (Hofmann & Sausgruber, 2017).

#### 2.3.1.4.3 Sites for position and height validation with CRs

The sites selected for the evaluation of XYZ and time series accuracy with CRs are described below. Detailed information can be found in [D5-Validation Areas](#).

- **Indre Nordnes** and **Jettan** are two unstable mountain ranges on the eastern side of the Lyngenfjord (Norway). These locations are part of a cluster of deforming rock slopes in the region, which are influenced by the geological history, bedrock structure, fluid flow, permafrost, and weathering processes [Vick et al, 2021, Rouvet et al., 2021]. These rock



slopes pose a significant hazard, as they have the potential of triggering rock avalanches that could endanger nearby settlements and infrastructures [Hermanns et al, 2018].

- **Thyborøn** (Denmark) is located on a sandy barrier facing the North Sea and is vulnerable to flooding from the adjacent Linford due to its low elevation (1.0 – 2.5m). Coastal subsidence is believed to be a consequence of the overall sedimentary structure of the barriers and landfills, including the compaction of some highly compressible layers. The region, mainly constructed on landfill and soft sediments, exhibits notable subsidence rates exceeding 7 mm/year, particularly in its south-eastern parts.

### 2.3.2 EGMS Applicability and Usability

Three validation activities focused on applicability were conducted across various validation sites (Figure 2.9). Detailed methodologies for each activity can be found in document [D6-Validation Methodologies](#); in particular, the Active Deformation Areas (ADA) approach has been used across the three validation methods.

IoAs are not converted to values between 0 and 1, but expressed as statistical or physical metrics, or as a qualitative assessment of the agreement between EGMS and ancillary data (based on expert interpretation).

#### 2.3.2.1 Validation by comparison with other Ground Motion Services (GMS)

##### a) Objectives and validation steps

This validation activity consists in comparing EGMS products with quality-controlled and validated datasets from existing operational national/regional GMSs.

Due to varying availability of product levels in the respective public national/regional GMSs, the validation is limited to comparable datasets and processing levels. Spatial resampling to 30x30m and automated detection of ADAs were performed to facilitate intercomparison of different GMSs.

It is important to note that national/regional GMSs are affected by similar errors as EGMS, including residual atmospheric phase, digital elevation model inaccuracies, and phase unwrapping errors. And differences in processing algorithms may create differences in the ground motion velocity and time series. Thus, they should not be used as "ground truth".

Different aspects are considered when performing the comparison:

- EGMS and the other GMSs generation are based on different processing strategies, e.g. EGMS is designed to map displacements over large areas while some GMSs may focus on the analysis of more localized phenomena such as landslides.
- The two datasets are not re-referenced to a common reference point or GNSS model. This choice was made to avoid altering the datasets beyond the applied pre-processing described in [D6-Validation Methodologies](#). However, this needs to be considered when comparing datasets, especially for the uncalibrated Basic/L2a products.
- Calibration differences and different reference systems must be considered when comparing calibrated data.

##### b) IoA definition

The different metrics involved in IoA computation are listed in Table 2.6.



Table 2.6: IoAs defined for the validation by comparison with other GMSs.

IoA	Metric calculation and interpretation	EGMS products
<b>Spatial overlap between moving areas (EGMS vs GMS)</b>	Overlap between ADA polygons obtained from two GMS sources. Formula: Maximum of: (Number ADAs with > 30% overlap) * 100 / Number ADAs OR (Total overlap area all ADAs * 100) / (Total area joined ADAs)	Basic/L2a, Calibrated/L2b and Ortho/L3
<b>Relative velocity difference (EGMS vs GMS)</b>	Relative velocity difference calculated as follows: $(\text{abs}(d\text{Vel}) * 100) / \text{maximum}(\text{abs}(\text{Vel}_{\text{EGMS}} + \text{Vel}_{\text{validation}})/2, 3.0)$	Basic/L2a, Calibrated/L2b and Ortho/L3
<b>Velocity correlation coefficient (EGMS vs GMS)</b>	Spatial correlation of velocity values on a common grid using Pearson <sup>1</sup> Correlation coefficient (linear correlation)	Basic/L2a, Calibrated/L2b and Ortho/L3
<b>Displacement correlation coefficient (EGMS vs GMS)</b>	Mean of Temporal correlation of time series using Pearson Correlation coefficient (linear correlation)	Basic/L2a, Calibrated/L2b and Ortho/L3

### 2.3.2.2 Validation by comparison with inventories of phenomena

#### a) Objectives and validation steps

The main goal of this validation activity is to compare the EGMS data with information from inventories, such as points or polygons representing the geometry, expected velocity or qualitative characteristics of the phenomena, along with dates of geohazard events or documented damage.

This activity aims to assess EGMS's detection capabilities in geohazard management by examining its potential to complement or create inventories when they do not exist. The focus is on the capability to detect known phenomena and, when available, to assess the similarity between ADAs derived from both inventories and EGMS, which serves as a key validation indicator for mapping geohazards. The characteristics of the addressed phenomena, including size and velocity of movement, are considered as they have an impact on the validation analysis.

#### b) IoA definition

The different metrics involved in IoA computation are listed in Table 2.7.

A positive detection of a landslide in EGMS is determined if the EGMS velocities detected within the inventory polygons differ significantly from those in the surroundings (outside the inventory). A detection is considered successful when the velocity difference between the inside and outside of the polygon exceeds 2 mm/year.

<sup>1</sup> Pearson correlation coefficient: <https://www.sciencedirect.com/topics/social-sciences/pearson-correlation-coefficient>



Table 2.7: IoAs defined for the validation by comparison with inventories of phenomena.

IoA	Metric calculation and interpretation	EGMS products
<b>Phenomena captured (yes/no)</b>	Binary detection based on velocity threshold: This parameter is positive if the motion detected by EGMS inside the inventory polygons is significantly different (>2 mm/year) from all the EGMS MPs outside the inventoried phenomenon.	Basic/L2a, Calibrated/L2b
<b>EGMS ADA and phenomena area intersection</b>	% of Intersection between EGMS active deformation areas (ADA) polygons and inventory polygons representing phenomena. The following formula is used: $\text{intersection} = \text{DIA}/\text{DMA} * 100;$ $\text{non-intersection} = \text{DDA}/\text{DMA} * 100$ where DIA=intersection between polygons DDA=area difference between intersecting polygons (total list); DMA= (EGMS ADAs areas plus Inventory areas)*0.5	Basic/L2a, Calibrated/L2b
<b>EGMS ADA and phenomena location/point</b>	Point within ADA: EGMS active deformation areas (ADA) polygons contain the inventories of phenomena represented with points.	Basic/L2a, Calibrated/L2b

### 2.3.2.3 Validation by consistency checks with ancillary data

#### a) Objectives and validation steps

This activity utilizes national inventories of geomorphological, geotechnical, and geological data, along with expert judgment and automated procedures, to interpret the presence of moving areas in EGMS on the base of radar interpretation. Ancillary data, such as information on landslides, active faults, or mining activity, supports the interpretation.

#### b) IoA definition

The validation approach does not directly translate into quantitative statistics or IoA values. It provides valuable insights into the alignment of EGMS products with geological and geotechnical considerations, based on expert assessment.

When quantitative comparisons between EGMS products and ancillary geoinformation are feasible, such information is utilized to support expert interpretation. Table 2.8 provides a listing on the metrics derived in this case.

Table 2.8: IoAs defined for the validation by consistency checks with ancillary data.

IoA	Metric calculation and interpretation	EGMS products
<b>ADA detection vs land cover maps</b>	Correlation between anthropogenic land cover classes and active deformation areas (ADA) obtained from EGMS.	Basic/L2a, Calibrated/L2b and Ortho/L3
<b>ADA detection vs geological maps</b>	Correlation between depth to bedrock and deformation patterns (ADAs) derived from EGMS.	Basic/L2a, Calibrated/L2b and Ortho/L3
<b>ADA detection vs soil thickness maps</b>	Correlation between soil thickness maps and deformation patterns (ADAs) derived from EGMS.	Basic/L2a, Calibrated/L2b and Ortho/L3

<b>ADA Comparison with fault lines positions</b>	Correspondence between EGMS –active deformation areas (ADA) polygons and fault lines.	Basic/L2a, Calibrated/L2b and Ortho/L3
--	---	--

#### 2.3.2.4 Validation sites

The validation of EGMS products relies on a set of validation sites ([D5-Validation Areas](#)). Fourteen of them are used for the validation activities dedicated to EGMS product applicability and usability assessment. An overview of the selected sites is presented in Table 2.9 and in Figure 2.9. These locations were chosen for their broad geographic distribution and the diverse nature of the geohazards affecting them.

Table 2.9: Overview of validation sites (Applicability/Usability).

Methodologies Geohazards	Consistency with other GMS	Consistency with inventories of phenomena	Consistency with geo- information
Landslides	Aosta valley (IT) Tuscany (IT)	Rules / Arcos de la Frontera (ES) French Alps (FR)	-
Mining and post-mining	-	Lorraine region (FR)	Silesia (CZ) La Unión (ES)
Urban / Anthropogenic	Thyborøn (DK) Po delta (IT)	-	Oslo (NO) Tagus valley (PT)
Groundwater exploitation	-	-	Lorca (ES)
Extra (Volcanism)	Mount Etna (IT)	-	-

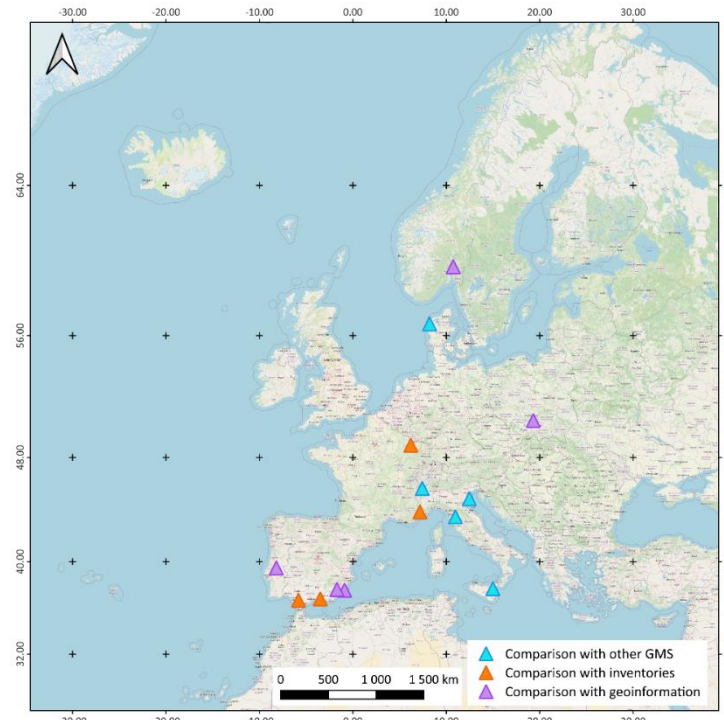


Figure 2.9: Distribution of the validation sites selected for the EGMS product applicability and usability assessment.

The sites are further described in subsections 2.3.2.4.1 to 2.3.2.4.3.

#### 2.3.2.4.1 Validation by consistency with other GMS validation

- The **Valle d'Aosta**, in northwestern Italy, covers 3200 km<sup>2</sup> of alpine terrain, with elevations ranging from 312 m at Pont Saint Martin to 4810 m at Monte Bianco peak. Over half of the region is above 2000 m altitude. As a result, the area's steep topography with high peaks and deep valleys is susceptible to landslides. Giordan et al., 2018, estimated that over 17% of Vale d'Aosta is affected by gravitational phenomena, including shallow landslides (debris flow, planar and rotational slides), rock fall, large slope instabilities, and Deep-seated Gravitational Slope Deformations (DSGSD).
- The validation site in the **Tuscany Region** covers the provinces of Massa Carrara, Lucca and Pistoia. In Tuscany, more than 100,000 landslide phenomena are known and mapped (Del Soldato et. al., 2019), with the areas along the Apennine ridge showing the highest density in landslide activity (Rosi et. al., 2018). Those displacements are monitored by InSAR.
- The motion in **Thyborøn** (Denmark) has also been assessed to validate EGMS product consistency and accuracy. A description of this site is provided in subsection 2.3.1.4.3.
- The **Po River delta** is an ecosystem covering approximately 400km<sup>2</sup>. Subsidence in this area results from both natural and human causes (Fabris et al., 2022). The natural component is primarily related to compressible Holocene deposits, contributing 2-4 mm per year. The human-induced component is associated with the extraction of water aquifers and can result in subsidence rates ranging from tens to hundreds of millimetres per year (Fabris et al., 2022).
- **Mount Etna**, standing at approximately 3,300 meters, is the largest active onshore volcano in Europe. Volcanic activity includes summit eruptions from five craters and fissural eruptions along three rift zones extending northeast, south, and west from the summit (Cappello et al., 2013). The Mount Etna eruption that took place from December 24-27, 2018, resulted in significant surface deformation. This event originated from fissures on the eastern flank of the volcano and was accompanied by a seismic swarm. The activity peaked on December 26 with a substantial earthquake (ML 4.8) along the Fiandaca Fault.

#### 2.3.2.4.2 Validation by consistency inventories of phenomena

- **Rules Reservoir** is a reservoir in Vélez de Benaudalla, province of Granada, Andalusia, Spain. The Rules Dam is located on the river Guadalefo, downstream from its confluence with the Izbor river, and collects the water from the southern slopes of Sierra Nevada Mountain range, from Sierra de Lújar and from La Contraviesa. The focus of the study are three active landslides within the slopes of the Rules Reservoir: the Lorenzo-1 Landslide, the Rules Viaduct Landslide and the El Arrecife Landslide. The first two are rotational landslides; InSAR displacement rates are up to 2 cm/yr for the Lorenzo-1 Landslide and up to 2.5 cm/yr for the Rules Viaduct Landslide. On the other hand, the El Arrecife Landslide has a translational character (the surface of rupture is planar) and therefore, it presents a potential hazard of experiencing critical acceleration and a partial or total rupture of the slope (Reyes-Carmona et al., 2022).
- **Arcos de la Frontera** is a National historic-artistic monumental town located in the province of Cádiz (Andalusia, Spain) that went through a vast urban expansion in the first decade of this century. New housing blocks were constructed on a gentle slope area underlined by weathered clayey soil of the Guadalquivir Blue Marls (GBM) formation, which is extensively present in the region and typically undergoes serious geotechnical problems such as landslide subsidence, collapse or soil creep (Escolano Sánchez et



al. 2019; Tsige and Corral 2013). Since the 1970s, landslide activity in Arcos de la Frontera has damaged infrastructure, urban assets, and buildings in the New Town area.

- The **Alpes-Maritimes** department is located in the Provence-Alpes-Côte d'Azur region of southeastern France, bordering Italy to the east. The target phenomena are landslides. There are several main areas in the region where many landslides have been recorded. Over the past two decades, the region has experienced numerous episodes of intense rainfall, with particularly notable events occurring in February and November 2014, and October 2000. The most recent one in October 2020 during the Alex storm, triggered damaging landslides in the Vésubie, Roya and Tinée valleys. Moreover, the area is characterized by deep seated landslides.
- In the Lorraine Region of France, sites of interest include the municipalities of Forbach and **Freyming-Merlebach** (see also section 2.3.1.4.2). This region's economy and development were historically driven by coal mining until its decline in the early 21st century. These study areas feature abandoned coal mines, which span over approximately 50 km<sup>2</sup> and were operational until 2004. Post-mining subsidence and uplift, due to underground changes, impact land stability. The site is monitored by levelling.

#### 2.3.2.4.3 Validation by consistency with other geoinformation

- The **Upper Silesian Coal Basin** (USCB), spanning over 6000 km<sup>2</sup> at the Czech-Polish border, is one of Europe's largest hard coal mining areas. Mining began in the 19th century. Urban growth, driven by the mining industry, has led to 37 towns with nearly three million residents today. Underground coal mining is the main cause of ground deformation, including subsidence and heave. Over 300 km<sup>2</sup> are already impacted by mining subsidence.
- **La Unión** mining district is located in southeast Spain at the Mediterranean coast. The area has large Pb and Zn deposits and was exploited until 1992. Fifty years of mining have buried the surrounding valleys and hills under waste. The primary deformation phenomena in this region are associated with post-mining slope instabilities affecting waste and tailings disposal facilities. After mining ceased in 1992, studies found that toxic metals continue to spread from destabilized mining wastes to nearby ecosystems.
- **Oslo** (Norway) is also selected as a validation site for assessing urban subsidence and the impact of engineering works/construction. Over the past 10-15 years, the vicinity of the Oslo central station has undergone extensive building and infrastructure development. Construction activities have led to significant settlements in the area, primarily caused by the reduction of pore pressure, mainly resulting from leakage associated with drilling activities (Hauser et al 2019).
- The **Lower Tagus Valley** Fault System is a set of active tectonic faults near Lisbon, Portugal. It has long been associated with damaging earthquakes that affected the Greater Lisbon Area in historical times. The most recent took place in 1909 with M6.0. Seismic hazards present significant risks to both populations and infrastructure, and they may impact CO<sub>2</sub> storage, geothermal projects, and underground energy storage initiatives. The region is experiencing significant pressure due to excessive exploitation of groundwater resources and ongoing construction activities. Numerous studies have documented substantial ground subsidence as a result.
- The last site is **Lorca** already described in subsection 2.3.1.4.1.



The findings of the validation activities are detailed in the following sections. Section 3 is dedicated to the presentation of the results of the Consistency and Accuracy validation activities, while Applicability and Usability are assessed in Section 4.

### 3 RESULTS – CONSISTENCY AND ACCURACY

This section aims to evaluate the accuracy of the EGMS portfolio in estimating ground motion across certain thematic areas. Specifically, the goal is to evaluate the EGMS's accuracy within the context of several applications, determining how effectively the data can quantitatively describe specific ground motion phenomena.

An overview of the validation sites was provided in 2.3.1.4. Detailed descriptions of the data and sites can be found in [D3-Validation Data Collection](#) and [D5-Validation Areas](#). At these sites, the EGMS portfolio is compared to in-situ data sources including:

- GNSS observations (velocity components and time series).
- Geodetic data acquired by in-situ landslide monitoring stations.
- Levelling data acquired by in-situ campaigns over abandoned mining.
- Piezometric data (groundwater level measurements).
- Artificial Corner Reflectors (CRs) deployed to optimally reflect the radar signal back to the satellite, along with precise measurements of CRs location.

#### 3.1 Velocity and time series validation by comparison with GNSS

##### 3.1.1 La Palma (Spain)

La Palma is monitored by eight continuous GNSS stations (Figure 3.1), five of them were deployed during the eruption.



Figure 3.1: La Palma Island and location of the GNSS stations (basemap: Google).

Due to ash cover and vegetation, only some MPs are observed within a 100 m radius around a certain GNSS stations. The data gaps in the time series of the GNSS stations are either because the GNSS data did not meet the internal quality standards or because of receiver changes due

to communication issues (e.g. station LP01). Stations with fewer than three MPs in their surroundings were excluded from analysis, such as station LP04.

Figure 3.2 shows an example of the double differences performed between GNSS and EGMS MPs around each GNSS station on the Basic/L2a products on ascending orbit track 060. The double difference comparison used 'MAZO' as reference station. Results differ slightly across stations, but the poor fit between EGMS and GNSS is evident, especially at station pairs with higher displacements due to the 2021 eruption.

The case of the descending track 069 is considered in Figure 3.3. The EGMS and GNSS displacement time series shows more similarity, though there is no perfect match (see extreme cases for stations LPAL-MAZO and LP06-MAZO).

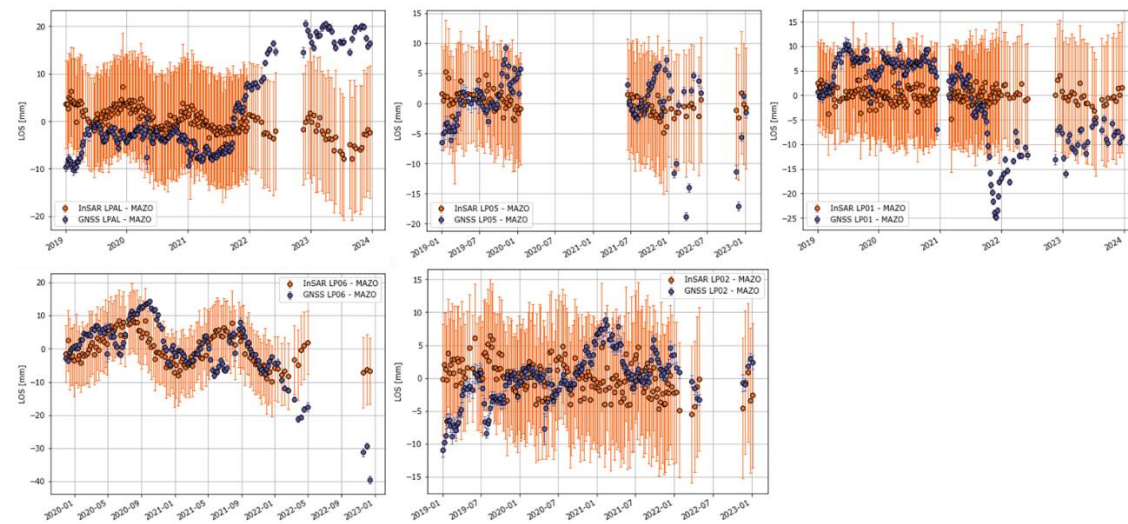


Figure 3.2: Double differences comparison between pairs of stations for EGMS Basic/L2a ascending track 060.

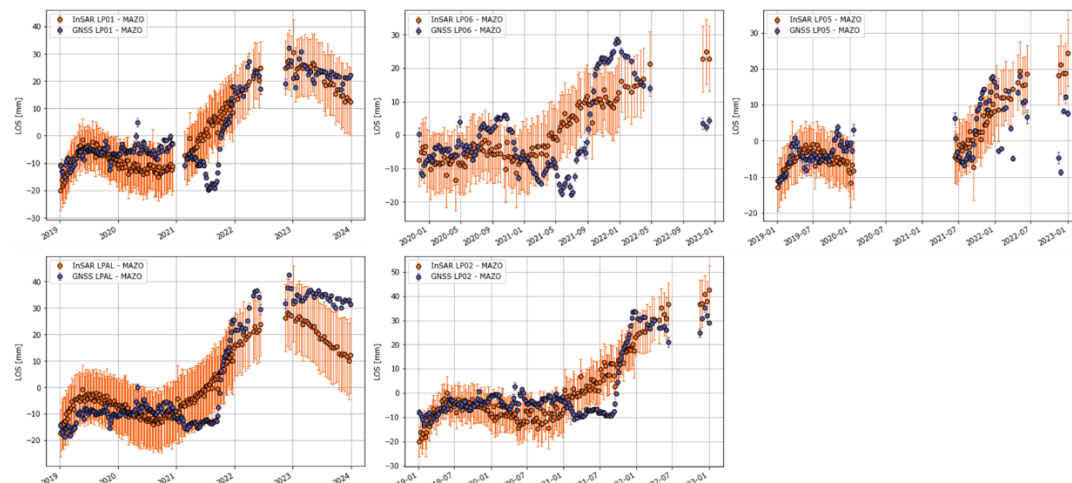


Figure 3.3: Double differences between pairs of stations for EGMS Basic/L2a descending track 069.

As reported in the validation of the [2<sup>nd</sup> EGMS update](#), the observation on the performance of the descending mode is crucial for a comprehensive analysis of different processing parameters. Figure 3.4 and Figure 3.5 present the outputs for the Calibrated/L2b product, with single differences shown. For the Calibrated/L2b products, the difference in ascending and descending tracks is not so clear, meaning that the better performance of the descending orbit does not hold for the full extent of the time series. While this achievement represents substantial progress on the possible use of EGMS for volcanic events monitoring, an understanding of the differences in performance between ascending and descending tracks remains necessary. The

better performance of the Basic/L2a product for descending orbit, compared with the Calibrated/L2b product, may be due to the highly non-linear displacements associated with the volcanic eruption. When calibrated with GNSS, these displacements might become smoother, which could lead to the loss of the non-linearity characteristic of the pre-, co-, and post eruptive phases. Therefore, it should be stressed that during eruptive events, Basic/L2a products are the most reliable choice.

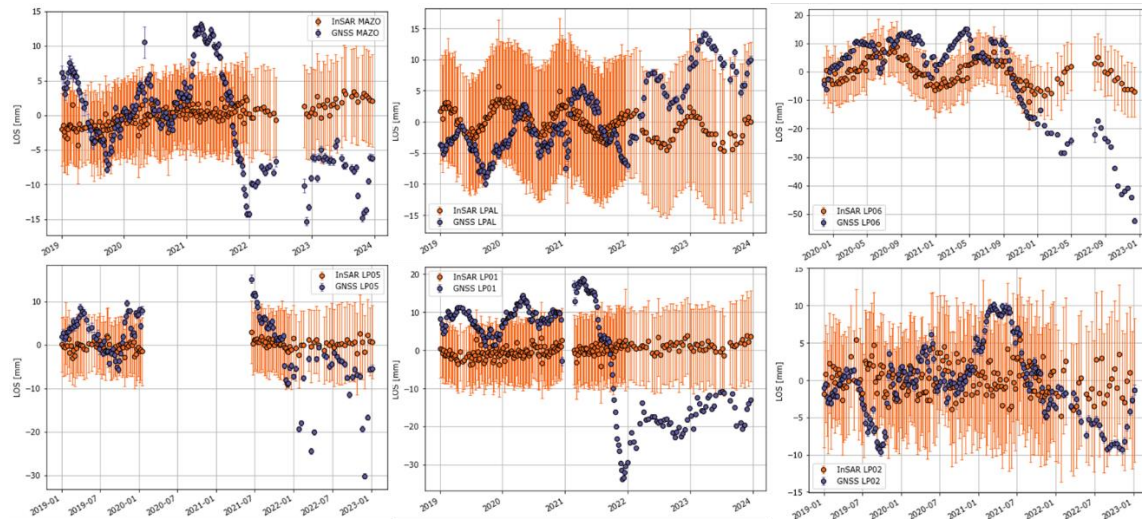


Figure 3.4 Single differences between GNSS and EGMS for Calibrated/L2b ascending track 060.

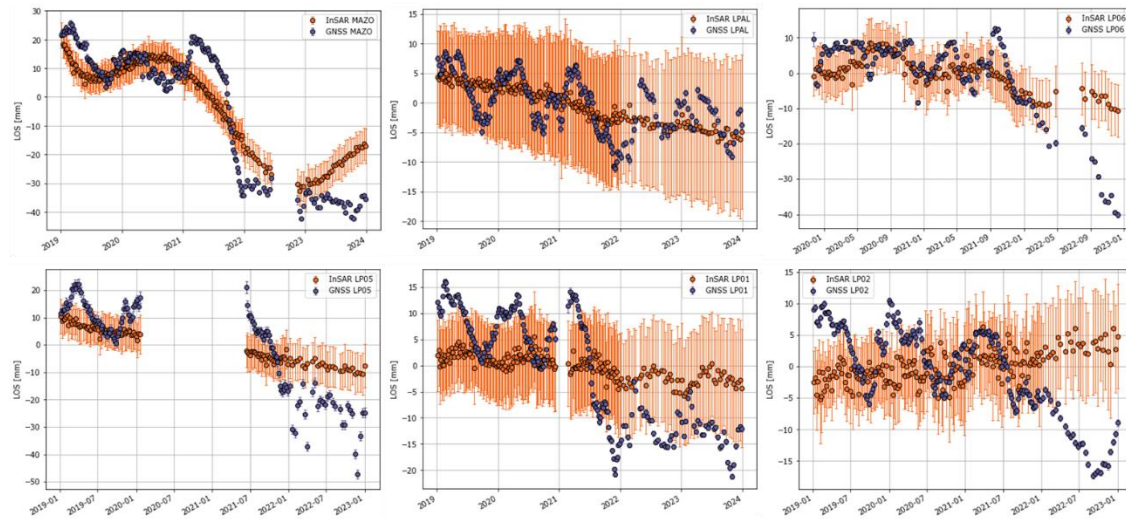


Figure 3.5: Single differences between GNSS and EGMS for Calibrated/L2b descending track 169.

Computed IoAs are summarized for all EGMS products in Figure 3.6. Further description of the metrics can be found in Table 2.2. The maximum IoA is obtained for MAZO station, as it is used as reference. As anticipated, the descending orbit shows better performance than the ascending one. This is further confirmed by the fact that station 'LP03' shows low IoA for the ascending track.

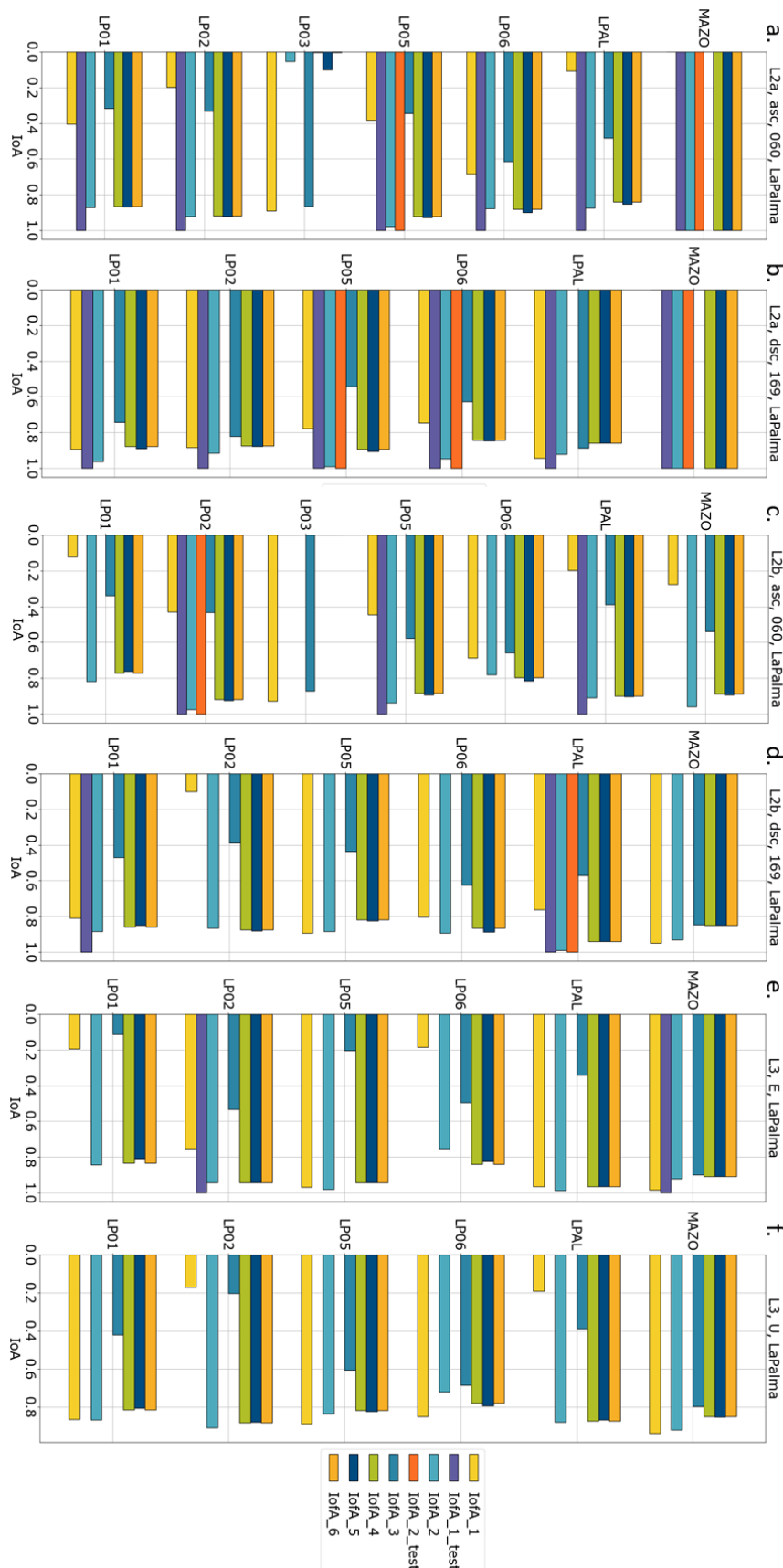


Figure 3.6: Summary of all IoAs per station and EGMS products.

---

*The La Palma interferometric data processing presents challenges due to the volcanic event that occurred in 2021. The results have provided compelling insights when comparing the performance of GNSS and EGMS.*

*Notably, the descending orbit for the Basic/L2a products has shown a more promising outcome, with the EGMS demonstrating a good ability to replicate the GNSS time series displacement signature. This performance marks a significant step forward to fine-tune the EGMS in active volcanic regions. It is important to emphasize that, given the non-linear nature of displacements associated with volcanic eruptions, Basic/L2a products are the most reliable option.*

---

### 3.1.2 Gran Canaria (Spain)

Due to the availability of GNSS stations, the validation activities have been focused on Gran Canaria Island (Figure 3.7).



Figure 3.7: Grand Canaria, in Spain, and GNSS stations distribution. (basemap: Google)

In the analysis of the Basic/L2a and Calibrated/L2b products (ascending orbit 162), all stations pass the Overall Model Test (OMT) (see section 2.3.1.1) for the time series across all tracks. When examining velocity estimation, there is a strong agreement between the EGMS and GNSS stations. However, ALDE is the station with the weakest fit, showing velocity differences of approximately 1.2 mm/year for the Basic/L2a products and 2.1 mm/year for the Calibrated/L2b products.

Figure 3.8 and Figure 3.9 illustrates both the worst and the best performance in the time series comparison for the Basic/L2a and Calibrated/L2b products regarding velocity and seasonality correlations. Subplots a. and b. demonstrate the best velocity correlation examples between EGMS and GNSS, while subplots c. and d. illustrate the worst velocity correlation examples. Similarly, subplots e. and f. present the best seasonality correlation examples, whereas subplots g. and h. depict the worst examples of seasonality correlation time series.

The left column shows Basic/L2a products with 'MAS1' as the reference station, while the right column shows the Calibrated/L2b products. The orange error bars of the EGMS MPs were derived from all the data points falling within the search radius. The best correlation examples

consistently feature the descending track 096, with only one instance showing the worst correlation for velocity estimation, resulting in a difference of 1.2 mm/year.

In Figure 3.8, it is observed that station ALDE effectively captures the linear descending trend of the GNSS time series for the descending track 096 (subplot b.), while it does not perform well for the ascending track 162 (subplot d.). The strongest correlation in both velocity and seasonality between GNSS and EGMS time series is found at station ALDE track 096. In contrast, AGUI GNSS station shows the weakest results displaying a good velocity correlation but an anti-correlated seasonal signal. Note that the gaps in the GNSS stations TERR, AGUI, ALDE, and ARGU during the last half of 2022 occurred because the data did not meet the quality standards of the GNSS processing made by IGN.

Overall, the agreement between EGMS and GNSS stations is better for Basic/L2a than for Calibrated/L2b products. In the case of Calibrated/L2b products, four out of seven stations for the ascending orbit and five out of seven for the descending orbit do not pass the velocity test. However, note that the stations failing the velocity test have velocity differences ranging from 0.6 to 2 mm/year. The station ALDE has the worst performance for the ascending orbit, with a 2.1 mm/year difference between GNSS and EGMS.

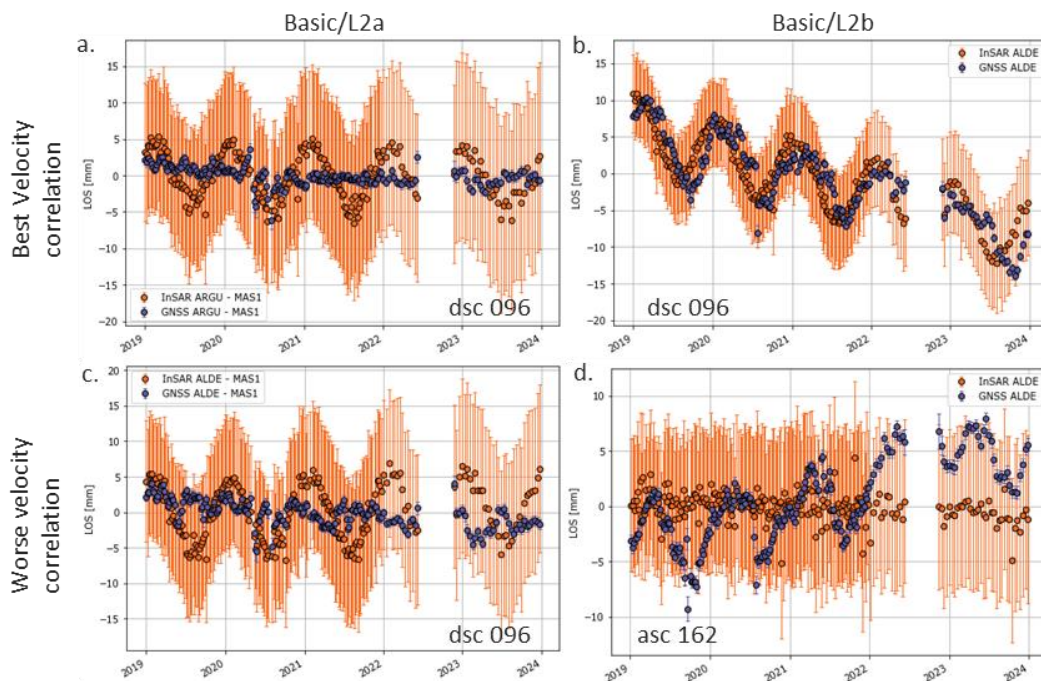


Figure 3.8: Examples of GNSS and EGMS time series used to assess velocity performance for Basic/L2a and Calibrated/L2b products.

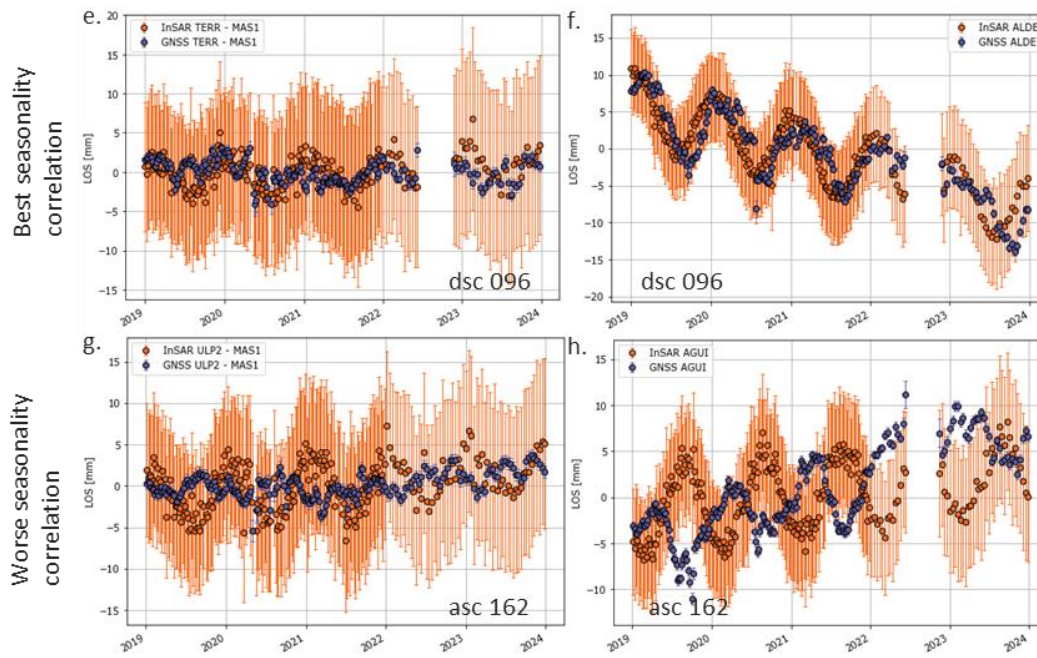


Figure 3.9: Examples of GNSS and EGMS time series used to assess seasonality performance for Basic/L2a and Calibrated/L2b products.

Figure 3.10 illustrates the comparison of the Ortho/L3 products in both east-west (top row) and vertical (bottom row) directions. Subplots c. and d. display the worse cases, because of higher velocity differences (subplot c.) or anti-correlated (or off-phase) seasonal deformation.

The velocity estimations indicate a strong correlation between the GNSS and the EGMS product. The largest velocity differences for the East-West Ortho/L3 products are observed at ALDE station, equal to 1 mm/year, followed by ARGU, which records a 0.5 mm/year difference with EGMS time series. The time series exhibit more considerable differences for seasonal patterns. Generally, the EGMS Ortho/L3 vertical time series exhibit a more pronounced anti-correlation or a delay in the peaks and troughs than its east-west counterpart. GNSS data show seasonal effects at all stations with an amplitude signal up to 15 mm. The EGMS captures these seasonal variations particularly well at the AGUI and ALDE stations.

In some cases, the seasonal differences may be attributed to the spatial and temporal averaging, which involves resampling to a coarser grid and a standard 6- or 12-day temporal sampling to derive these products. However, explaining a consistently off-phase signal with low standard deviation as seen in Figure 3.10 subplot f. is more complicated.

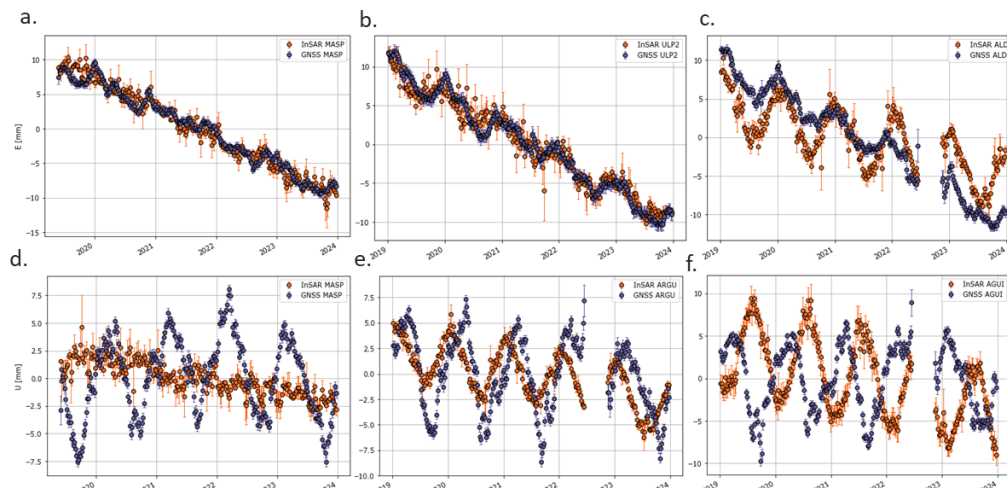


Figure 3.10: Ortho/L3 products comparison in the E-W (top row) and Vertical direction (bottom row).

The estimated IoAs are displayed in Figure 3.11, and further description on the metrics computed can be found in Table 2.2.

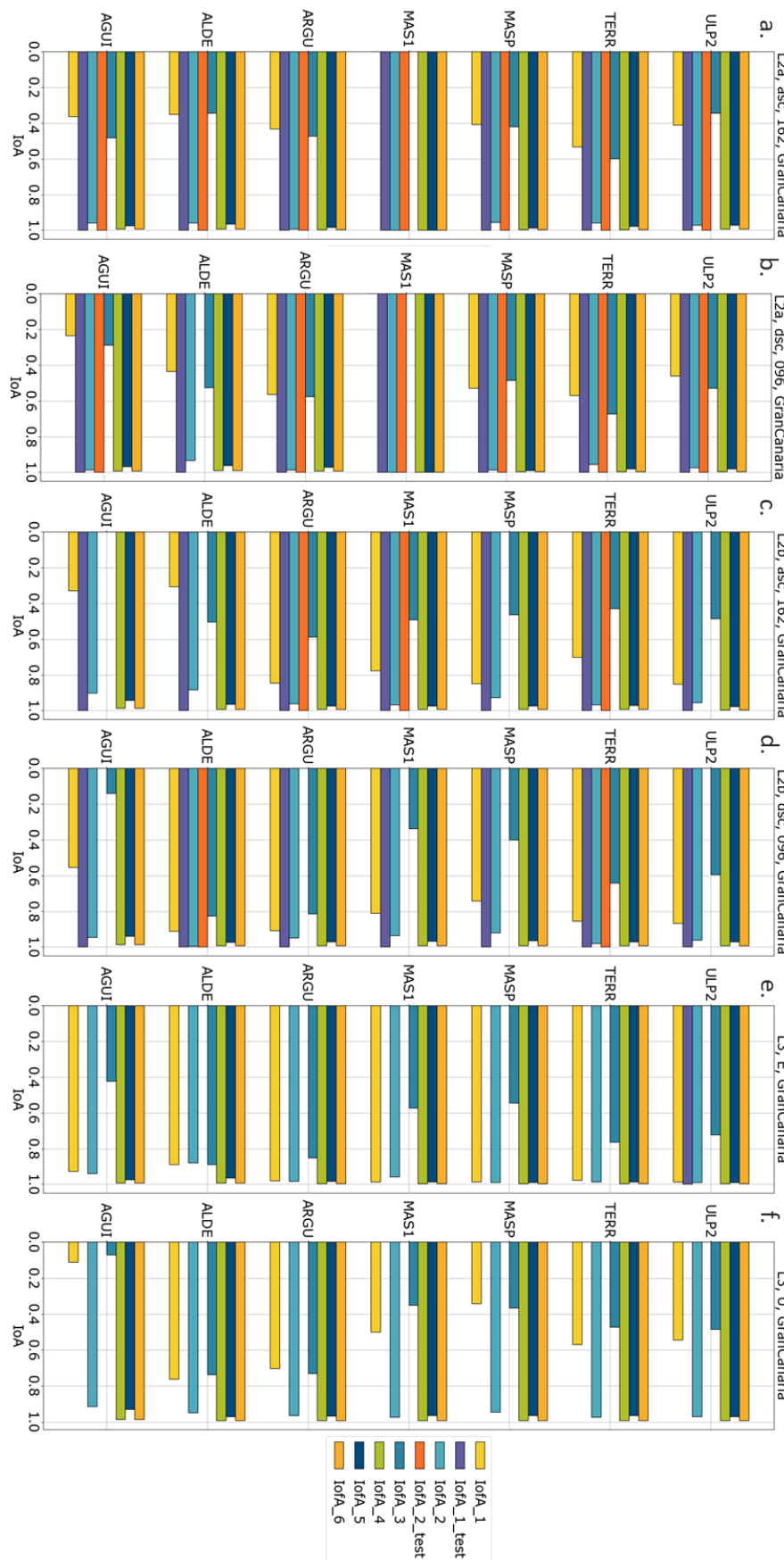


Figure 3.11: IoAs for Basic/L2a, Calibrated/L2b and Ortho/L3 EGMS products.

The Ortho East-West product consistently exhibits higher IoAs than the Ortho/L3 Vertical product across all stations.

The general assessment for the Gran Canaria test site is positive, with a good fit between most GNSS stations and the EGMS time series around those stations. The time series of the EGMS show a good agreement with GNSS for most stations and track combinations. The most considerable velocity difference has been estimated at the MASP GNSS station. It corresponds to 1.2 mm/year for Basic/L2a products, 2 mm/year for Calibrated/L2b products, and 2.2mm/year for Ortho/L3 Vertical. However, the mean velocity differences fall below 0.8 mm/year.

Due to the nature of the InSAR and GNSS—which involves the choice of spatial reference, time resampling, spatial averaging, atmospheric corrections, and the specific processing of GNSS data—seasonal effects should be carefully interpreted for Calibrated/L2b and Ortho/L3 products. They should additionally be carefully interpreted for Basic/L2a products because of the comparison between pairs of stations (double differences).

---

*The overall agreement between the EGMS and GNSS stations is slightly stronger for the Basic/L2a products compared to the Calibrated/L2b products, although the differences are minimal. The average velocity difference across all stations, tracks, and products at this test site is less than 0.8 mm per year – within the estimated precision of the EGMS.*

*The EGMS is capable of accurately measuring the moderate ground motion in Gran Canaria; however, the data regarding seasonal variations should be interpreted with caution.*

---

### 3.1.3 Guadalentín basin, Lorca Region (Spain)

Among all the validation sites, Lorca exhibits the highest displacement rates. This makes GNSS comparison particularly valuable for EGMS validation due to its challenging performance requirements. Stations LRCA, ORCA, and LORC (red square in Figure 3.12) mark this significant subsidence area.

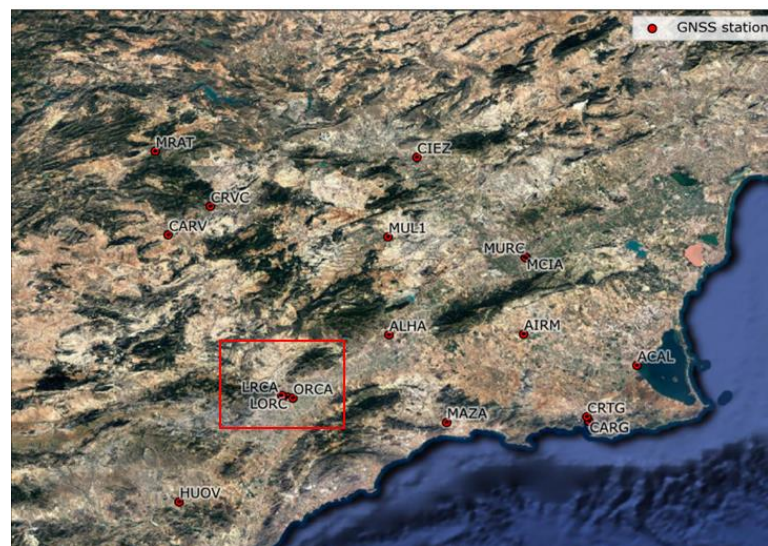


Figure 3.12: Lorca, in Spain, and the GNSS station distribution. (basemap: Google)

Given that the most significant deformation has been detected at stations LRCA, ORCA and LORC, the GNSS comparison with the EGMS products will focus on these three stations. The totality of the stations is used for the IoAs calculations. Figure 3.13 illustrates the comparison between Basic/L2a products and the GNSS measurements, in ascending orbit 103 (a, b, and c) and in descending track 008 (d, e, and f). CARG station is used as reference. The figure shows

that EGMS captures significant deformations in both ascending and descending tracks. Note that, for station ORCA, which is operated by the Instituto Geológico y Minero (IGME), the GNSS data only covers the period up to 2020.

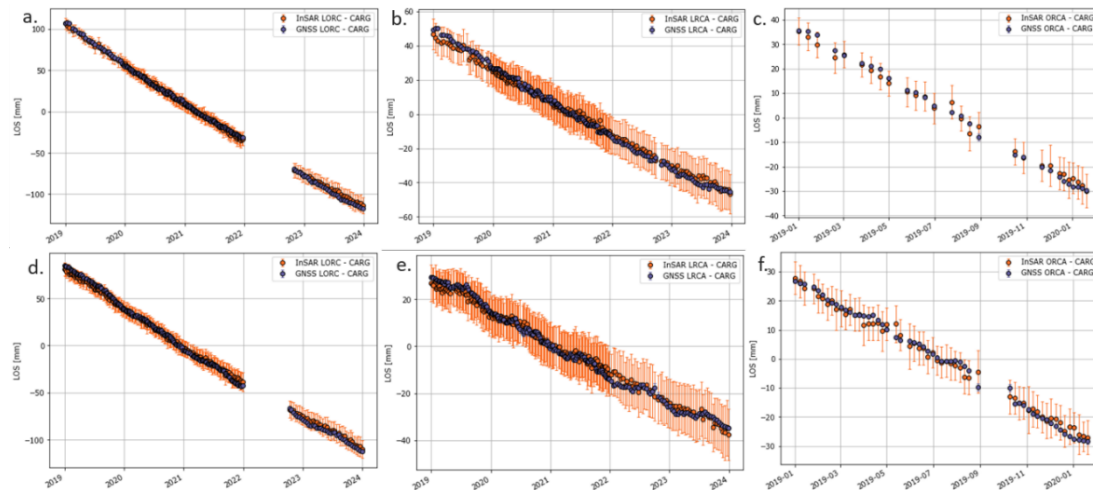


Figure 3.13: Example of double differences between pairs of stations of Basic/L2a ascending and descending orbits.

Figure 3.14 presents single differences between EGMS and GNSS for Calibrated/L2b products on the ascending track 103, for the ORCA, LRCA and LORC stations. Other stations located outside the boundaries of Lorca's subsidence area, such as CARG, HUOV, MAZA, ACAL, and CRTG show consistent velocity differences below 0.6 mm/year across most EGMS products, indicating a near-perfect fit between GNSS and EGMS.

The Calibrated/L2b products exhibit similar patterns to Basic/L2a regarding the fit between EGMS and GNSS products. For Calibrated/L2b, ORCA, the station with the higher subsidence rate, records a velocity difference of 5 mm/year for the ascending track 001 and 1.3 mm/year for ascending track 103. Despite the differences in the velocity estimation, the consistency between the EGMS and GNSS time series is high. All the EGMS observations fall within the 1-sigma interval at all timestamps.

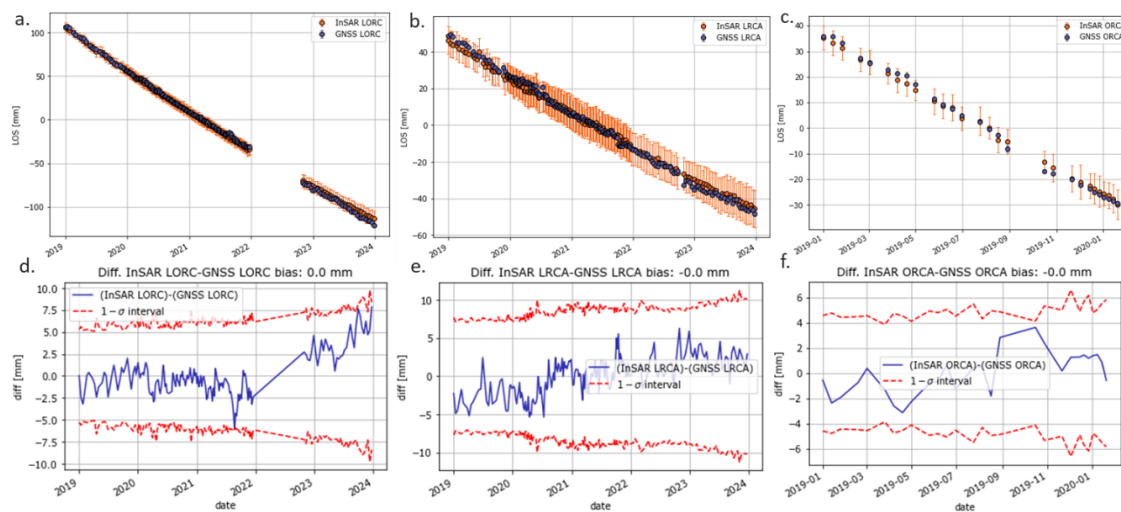


Figure 3.14: Comparison between EGMS and GNSS for Calibrated/L2b ascending orbit 103.

With respect to Ortho/L3 products, the fit in the vertical direction consistently outperforms that in the east-west direction. The velocity correlation plots between EGMS and GNSS are drawn in Figure 3.15 and Figure 3.16, for the ascending and descending orbits, respectively. The Basic/L2a, Calibrated/L2b and Ortho/L3 East-West are considered. The black full line indicates perfect agreement between the estimated velocities of the EGMS MPs and GNSS station.

Dashed line indicates the best fit line between all stations. Most stations align well with the black full line, showing a strong agreement between the estimated velocities of EGMS MPs and the ones of the GNSS station.

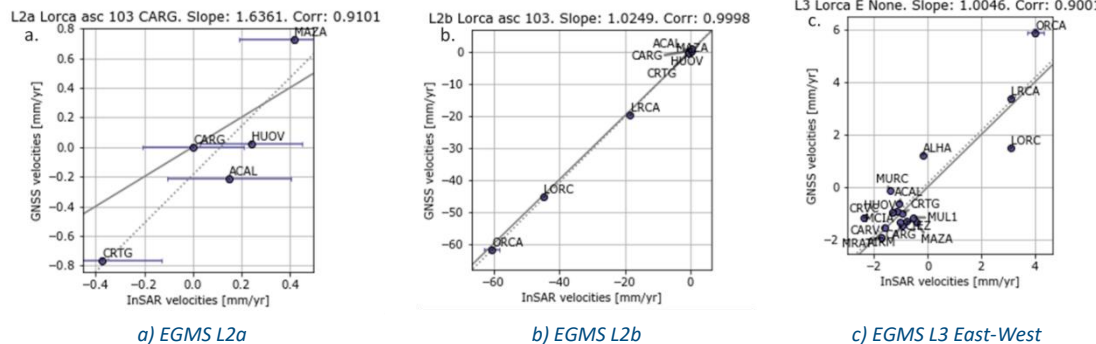


Figure 3.15: Correlation between EGMS and GNSS velocity estimations for the three EGMS products along ascending track 103.

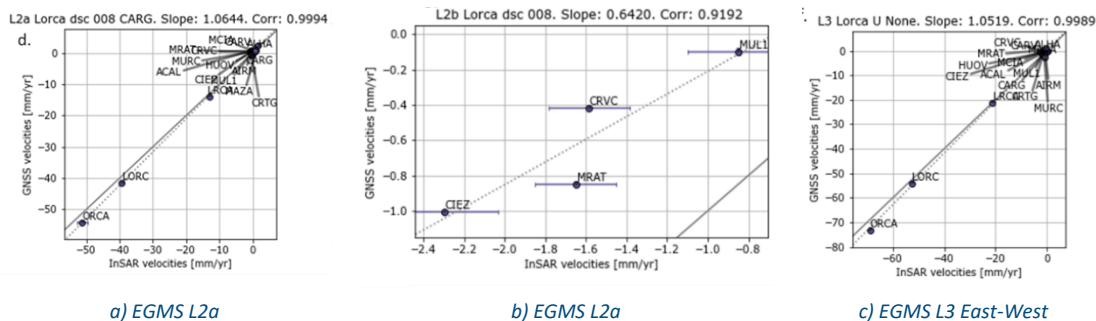


Figure 3.16: Correlation between EGMS and GNSS velocity estimations for the three EGMS products along descending track 088.

Figure 3.17 summarizes the IoAs of all EGMS products per station in the form of bar charts. Further description on the metrics computed can be found in Table 2.2.

The IoAs show better performance for the ascending track than for the descending track, for both Basic/L2a and Calibrated/L2b products. The lower performance of the IoAs in the descending track is primarily due to the parameter used to compute the seasonality. However, most stations pass the OMT for time series evaluation and the t-test for velocity in both tracks. As expected, the IoA values for the vertical component of the Ortho/L3 products are generally higher than those for the east-west component. Among all stations, in the vertical component, 'LRCA', 'ORCA' and 'LORC' show the lowest IoA values. This is surprising considering the perfect fit shown in Figure 3.18 (a., b. and c.). The low values of these IoAs can be attributed to the selected EGMS MPs showing lower variation. Therefore, when comparing the differences between GNSS and EGMS, most values fall outside the one-sigma or one standard deviation from the mean, as illustrated in Figure 3.18 (d., e., and f.).

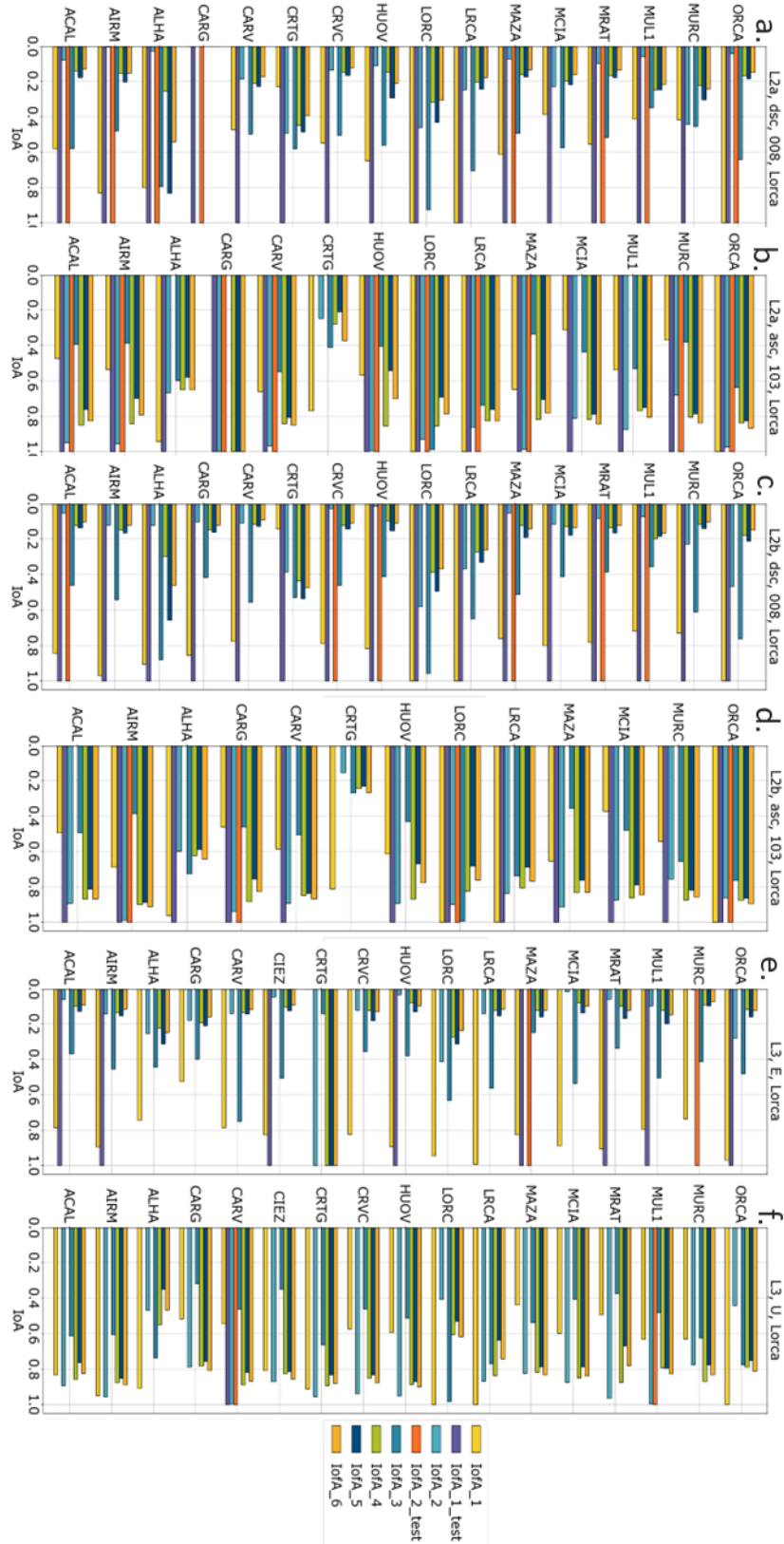


Figure 3.17: IoAs for Basic/L2a, Calibrated/L2b and Ortho/L3 products.

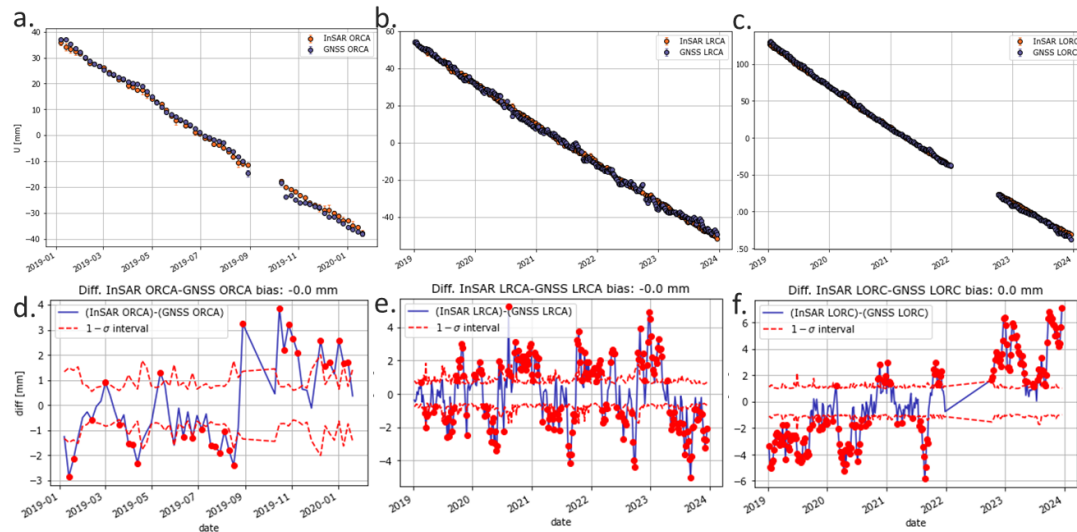


Figure 3.18: Comparison between GNSS and EGMS for Ortho/L3 products in the vertical direction.

The results demonstrate the EGMS's ability to capture subsidence induced by groundwater exploitation in the Lorca region, and possibly at other locations with comparable accuracies.

Assuming GNSS measurements as ground truth, these results illustrate that EGMS can effectively capture the strongest deformation in areas with high groundwater extraction rates.

Accuracy on the velocity estimation can reach sub-millimetre levels, with errors below 1 mm/year. This level of accuracy provides a good foundation to use EGMS to assess surface deformation estimation in this specific field of application.

### 3.1.4 Jutland peninsula (Denmark)

The Jutland area has been monitored by continuous GNSS stations since around 2010 (Figure 3.19), targeting coastal subsidence. In some rural areas of Jutland, few MPs were observed within the applied 100 m radius around the GNSS stations. Station TEJH was excluded from the analysis due to not reaching the minimum required number of EGMS MPs in its vicinity.

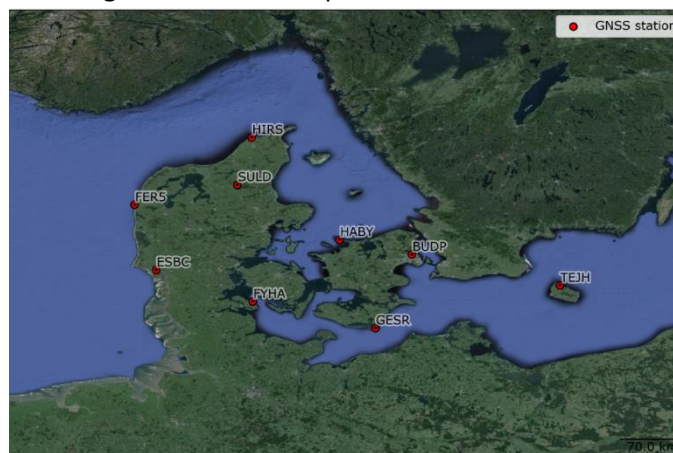


Figure 3.19: The Jutland peninsula in Denmark and the distribution of GNSS stations (basemap: Google).

Figure 3.20 and Figure 3.21 display the higher (a., c., e. and g.) and lower (b., d., f., and g.) velocity correlations for the time series of EGMS Basic/L2a MPs comparisons around each GNSS station. The time series in the figures have FYHA station as reference. The orange error bars of the EGMS MPs were derived using all the MPs falling within the 100 m search radius.

One key distinction between EGMS MP time series and GNSS station data is the magnitude of seasonal effects. While GNSS stations exhibit pronounced seasonal signals, these are not well captured by the average of EGMS MPs within the selected radius around each GNSS station. However, the GNSS time series falls within the estimated standard deviation of the EGMS time series (indicated by the orange lines in Figure 3.20 and Figure 3.21). This suggests that the amplitude variations observed at some GNSS stations may be smoothed out when averaging the time series of EGMS MPs within the selected radius. An analysis of the individual MPs' time series at the two stations with the worst fit between EGMS and GNSS, ESBC and HIRS, supports this observation. For ESBC, a total of 127 points were selected within a 100-meter radius, while HIRS had 162 points, with 117 points for the ascending track. This represents a significantly larger number of MPs compared to the SULD station, which has only 7 MPs, and FERR, which has 40 MPs. The time series for ESBC and HIRS exhibit high variability; some individual time series reflect seasonal oscillations, while others do not. This variability presents a limitation of the approach. However, reducing the radius would mean there would be insufficient data points for analysis for other stations.

In the examples displayed, the standard deviation oscillates between -10 and 10 mm. All stations successfully pass the statistical time series test for all four tracks analysed. Considering all stations in all data products and tracks, the velocity differences between the GNSS and the EGMS estimations are 0.8 mm/year on average.

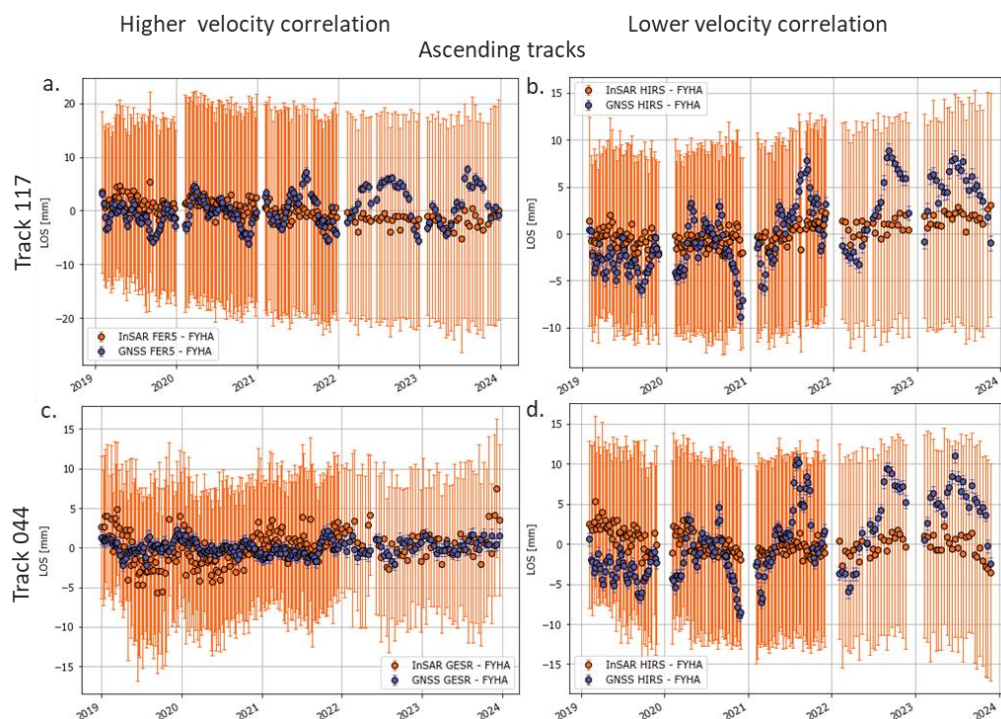


Figure 3.20: Double differences comparison between pairs of stations for EGMS Basic/L2a from ascending orbit (tracks 117 and 044).

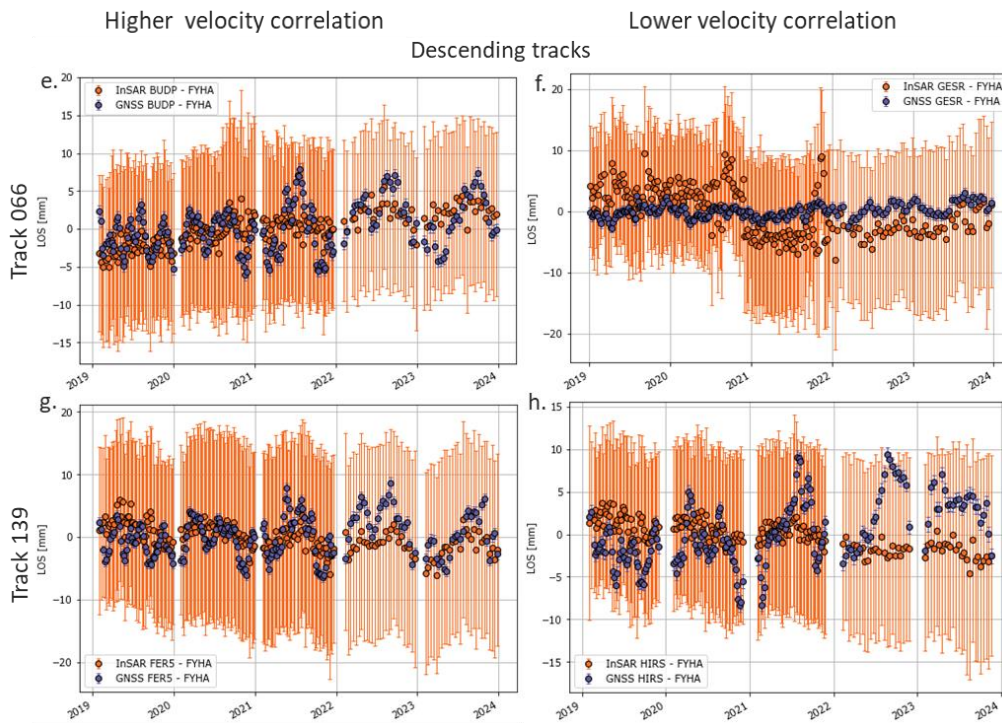


Figure 3.21: Double differences comparison between pairs of stations for EGMS Basic/L2a from descending orbit (tracks 066 and 139).

Figure 3.22 illustrates the differences between GNSS and EGMS within a 1-sigma interval or four out of the six stations (21 stations in total) that did not pass the velocity test. Still, the estimated average velocity differences between GNSS and EGMS are minimal and in the order of 0.8 mm/year. For most stations, those failing the velocity test show a linear trend within the 1-sigma deviation and a seasonal signal in the differences between the EGMS and GNSS time series. Overall, the seasonality index or the correlation of detrended signals demonstrates a satisfactory and improved relationship between seasonal effects observed in EGMS and GNSS for most products, with only a few stations showing discrepancies.

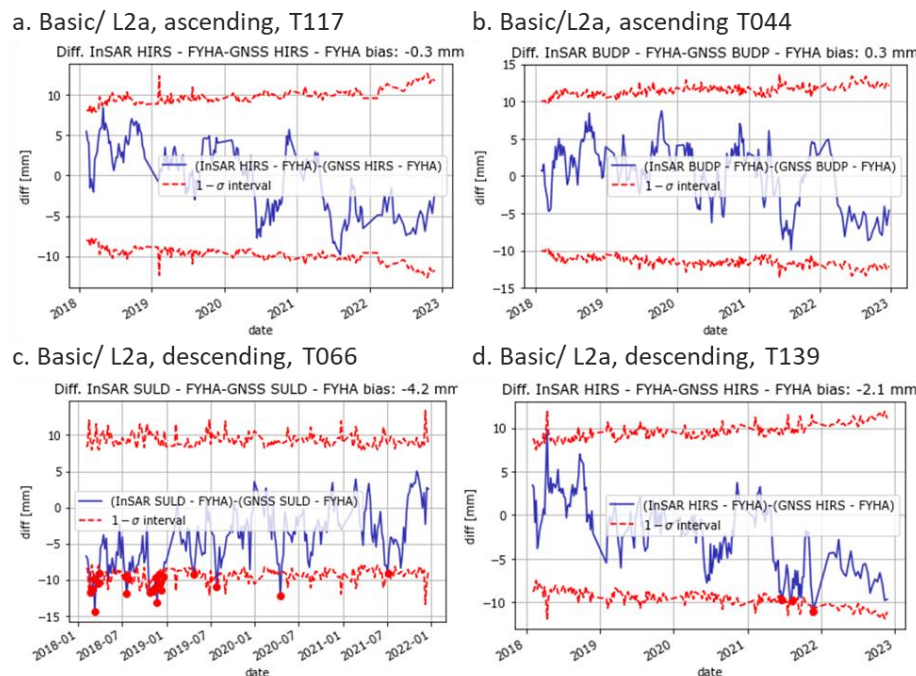


Figure 3.22: Examples of double differences for Basic/L2a products, highlighting comparisons for ascending and descending orbits for the stations that did not pass the velocity statistical test.

Figure 3.24 illustrates the correlation of estimated velocities between EGMS and GNSS across all stations for each track of the Basic/L2a and Calibrated/L2b EGMS products. Station location falling around the solid line indicates perfect agreement between the estimated double difference velocity of the EGMS and the GNSS. The dashed line indicates the best-fit line between all stations.

The diagrams confirm previous observations about velocity differences. The correlations indicate a good agreement between GNSS and EGMS estimated velocities for most EGMS products and orbits, except for isolated stations (e.g. HIRS and BUDP). The highest velocity differences observed between EGMS and GNSS are around 2 mm/year for Basic/L2a products (see station HIRS Figure 3.23, Figure 3.21 and Figure 3.22) and about 3 mm/year for Calibrated/L2b products (see GESR station Figure 3.24 Calibrated/L2b descending track 066).

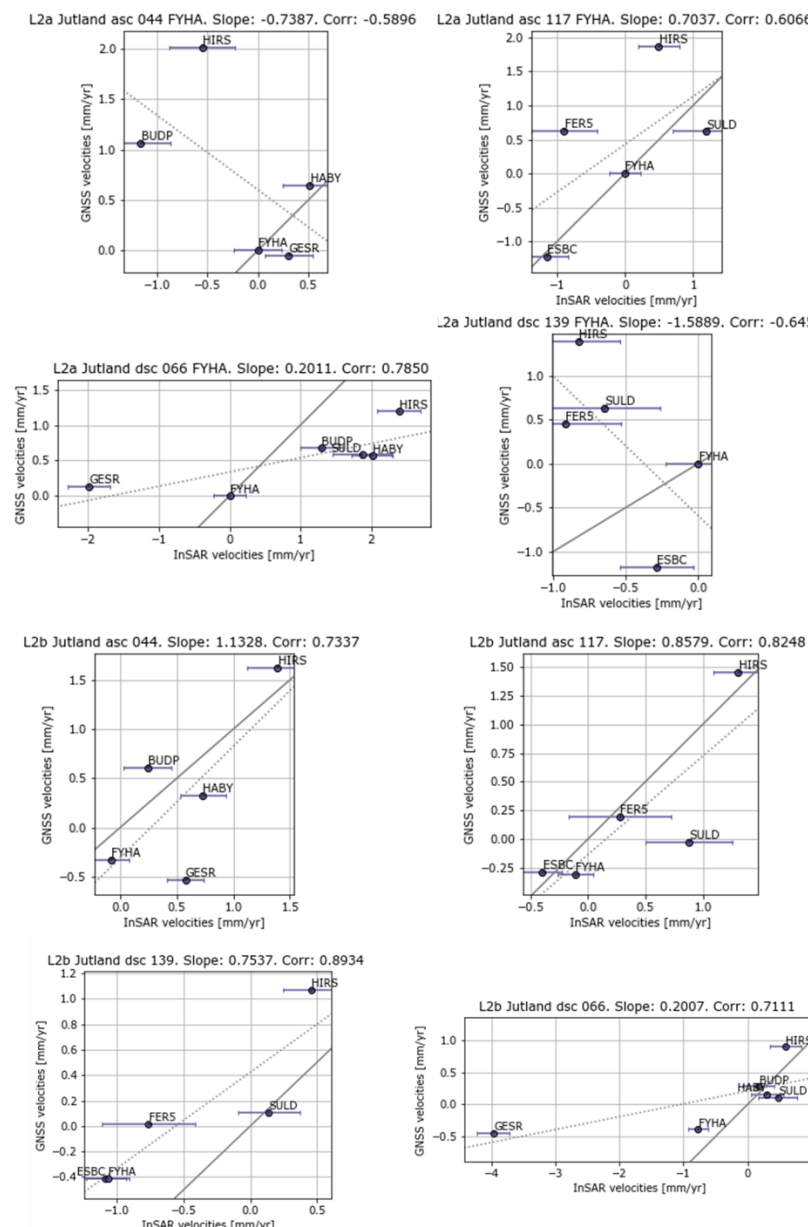


Figure 3.24: Correlation between EGMS and GNSS velocities for the Basic/L2a and Calibrated/L2b EGMS products.

Figure 3.25 illustrates the bar charts of the IoAs of the available ascending and descending orbits for the Basic/L2a, Calibrated/L2b products and the Ortho/L3 East-West and Vertical products. Further description on the computed metrics can be found in Table 2.2:

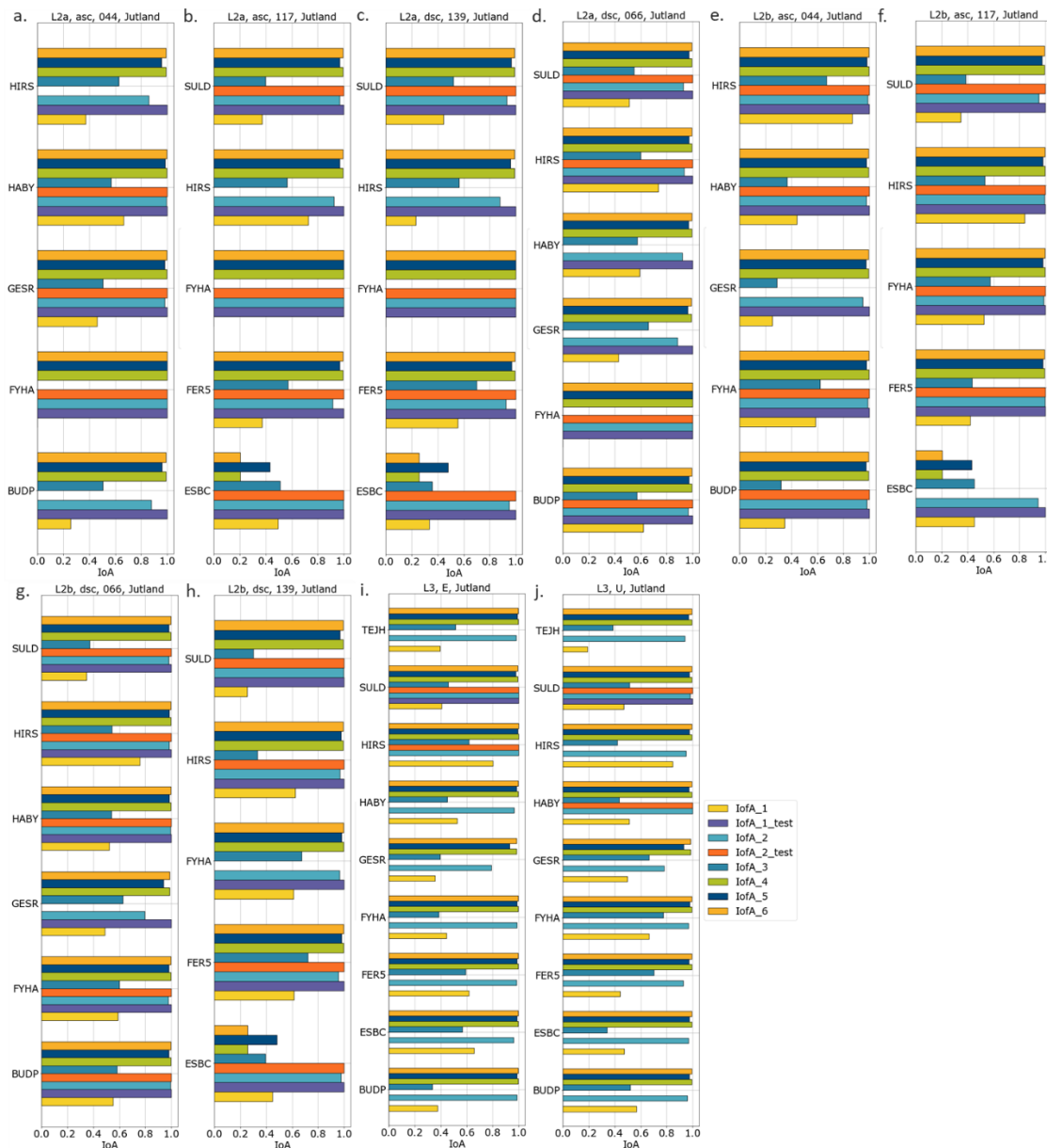


Figure 3.25: IoAs for all the EGMS products.

The OMT for the time series and the t-test for velocity differences yield significant positive outcomes for nearly all stations, indicating a strong similarity between the EGMS and GNSS time series. All stations have successfully passed the velocity statistical test for all orbits of the Calibrated/L2b products, reassuring this similarity, and only a few stations did not pass the time series statistical test.

For the Ortho/L3 products, the Ortho/L3 East-West (E) performance is equivalent to the Ortho/L3 Vertical (U) products with similar IoAs. 11% of the stations pass the time series, and 22% pass the velocity statistical tests for the east component. For the vertical component, 11% of the stations pass the time series statistical test and 22% the velocity statistical test. Two hypotheses can account for this lower performance compared to the Basic/L2a and Calibrated/L2b products: the gridded nature of the Ortho/L3 products and the sensitivity of the statistical tests. The time series statistical test is susceptible to outliers, leading to the rejection



of some time series even when only a few outliers are present (as indicated by the red points in Figure 3.21 c.).

Looking at the velocity differences, the average difference between the EGMS Ortho/L3 products and the GNSS stations is approximately 0.7 mm/year for the east component and 1.1 mm/year for the vertical component. Notably, only one station (GESR) acts as an outlier, with velocity differences exceeding 3 mm/year for both the Ortho/L3 East-West (E) and Ortho/L3 Vertical (U) products.

The velocity test is conducted by analysing the velocity differences between the EGMS and GNSS for each EGMS product. The test becomes more rigid since most velocity differences across all stations are low. As a result, even minor differences, such as 0.5 mm/year (as observed at the ESBC station in the Ortho/L3 Vertical), may not meet the test criteria. This limitation highlights the importance of employing diverse metrics (IoAs) for product comparison.

---

*The time series of the EGMS MPs at each GNSS station follows the trends of the corresponding GNSS data. Correlation plots for the Basic/L2a EGMS products indicate that the highest velocity differences reach up to 2 mm/year at specific stations, namely GESR, BULPD, and HIRS. In the case of the Calibrated/L2b products, these differences decrease substantially, except for GESR station, which reaches a velocity difference of 3.7 mm/year.*

*For the Ortho/L3 East-West (E) component, the highest velocity difference is 3.8 mm/year at station GERS, while for the Ortho/L3 Vertical (V) component, the same station is also an outlier reaching up to 3.9 mm/year.*

*Overall, the time series and velocity data for Denmark show a good fit between GNSS measurements and the EGMS MPs in the vicinity of the GNSS stations. All stations across all level products pass the time series overall model test, and 70% of all stations pass the velocity test. The remaining 30% are mostly, but not all, associated with the Ortho/L3 products.*

---

## 3.2 Velocity and time series validation by comparison with in-situ data

### 3.2.1 Lorraine (France)

The municipality of Freyming-Merlebach, located in the Lorraine region (France) near the German border, has experienced uplifts due to natural water filling in formerly exploited underground coal mines. A dataset consisting of over 850 yearly levelling measurements are used for comparison with the EGMS velocities. Their geographic localisation is shown in Figure 3.26.

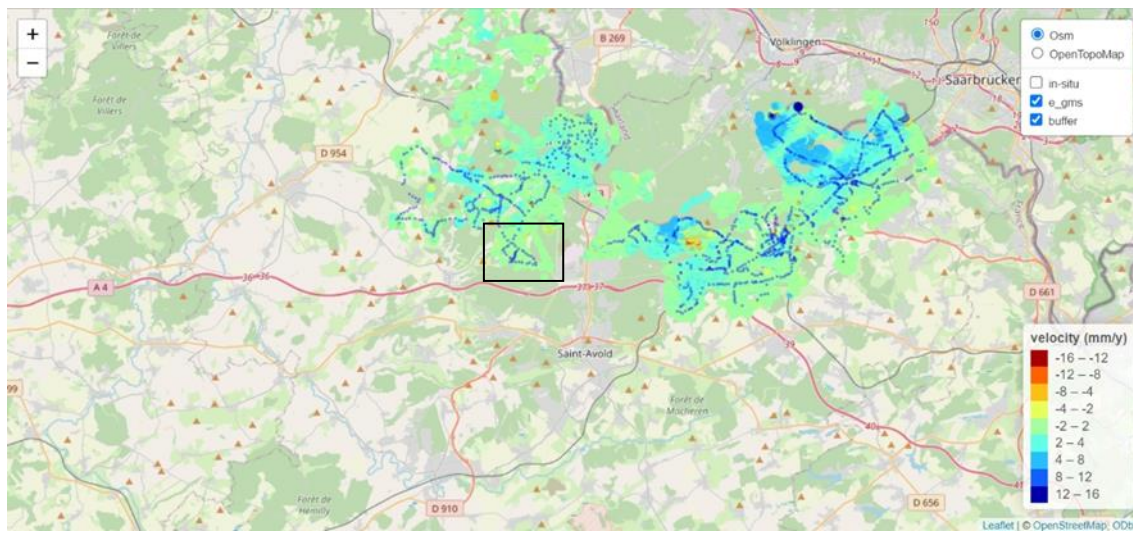


Figure 3.26: EGMS Basic/L2a ascending orbit (track 088) over Lorraine overlaid to the in-situ levelling stations available for validation shown in blue circles. (Basemap: OpenStreetMap).

EGMS products were acquired over ascending track 088 and descending track 037. The latter has a steeper satellite viewing geometry, which may be more suitable for comparison with levelling measurements, as these only captured the vertical component of displacement.

Velocity comparisons were conducted for all levelling stations over the 2019-2023 period, using data from both ascending track 088 and descending track 037. Basic/L2a, Calibrated/L2b and Ortho/L3 vertical are considered for the analysis while the Ortho/L3 E-W component is excluded. Note that the levelling measurement accuracy is about  $\pm 20$  mm/year, which is significantly less accurate than EGMS measurements.

Figure 3.27 shows the comparison between the averaged velocity computed for the levelling stations and the EGMS. Overall consistency is good; higher discrepancies between the plots are noticed over the first 150-200 stations. Those stations are mainly located in the western part of the study site (Figure 3.26).

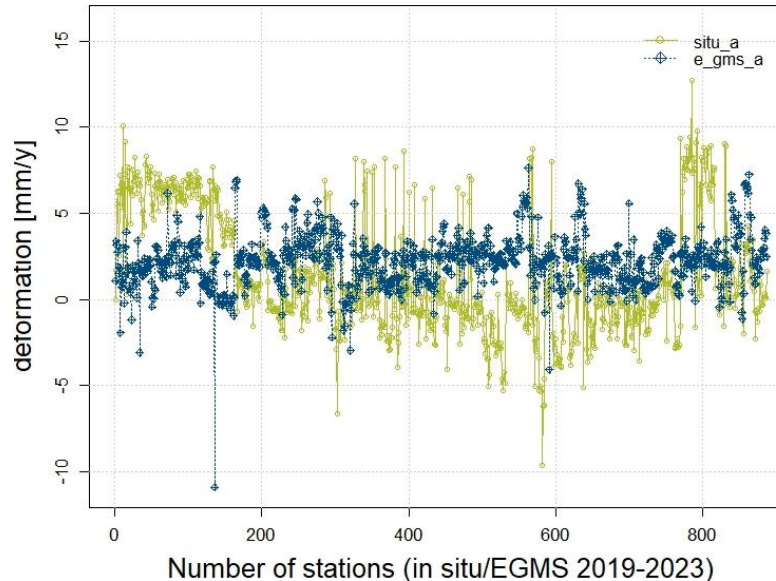


Figure 3.27: Plot showing the mean velocity measured by the totality of levelling points against the mean value of EGMS update 2019-2023 MPs that fall within 50m of the in-situ data.

Figure 3.28 shows time series from different levelling stations distributed across the site of interest. Stations 10164 and 10043, located in *Le Porcelette*, in the western sector (see black

rectangle in Figure 3.26), show a different behaviour. Unlike the consistent uplift trends observed at other stations, these two display divergent patterns. The EGMS is not able to capture the local seasonal variations that does not reflect the general uplift in Lorraine. This anomaly is attributed to the presence of clayey soils in the *Le Porcelette* area, which strongly react to water content variations, thus creating the seasonal variations that are observed in the time series in Figure 3.28.

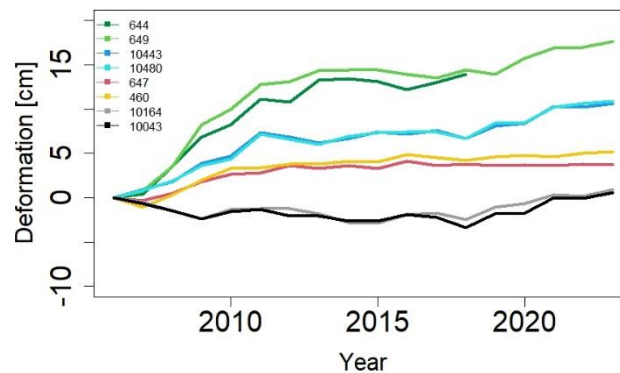


Figure 3.28: Plot showing the measurements (in cm/year) of eight different levelling stations distributed over the study site - Stations 10164 and 10043 are located in “Le Porcelette” area.

IoAs are computed for all levelling stations and orbits, and averaged. Additional description of the metrics can be found in Table 2.3. The results are displayed in Figure 3.29. The correlation IoA displays the lowest values, which may be related to the low performances observed for the *Le Porcelette* area. Error IoAs show good performances since the MAE remains below 5 mm for all products and orbits. Overall, the global IoA remain low, impacted by the Combined Index.

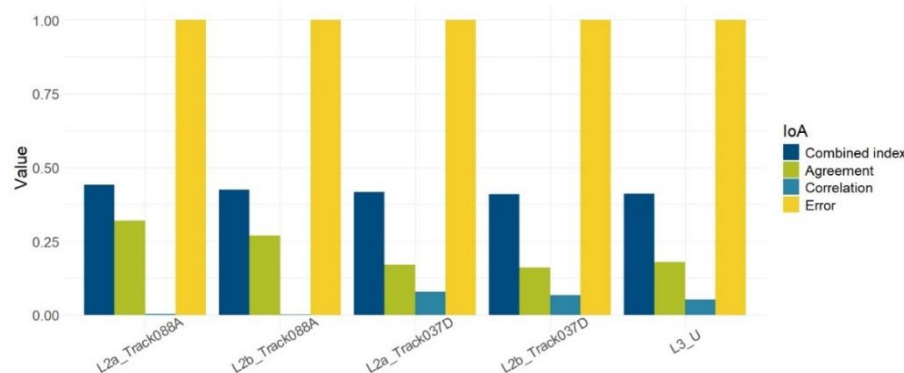


Figure 3.29: IoAs metrics for the comparison between levelling points average velocity and EGMS velocity for the MP falling inside the 50 m buffer of each station.

Time series comparison is then conducted over 10 selected levelling stations. The selection was based on the analysis of the average displacement of the InSAR MP within each 50-meter buffer; the stations showing the highest uplift rates detected on EGMS were chosen.

The estimated IoAs for each of the 10 selected stations are displayed in Figure 3.30.

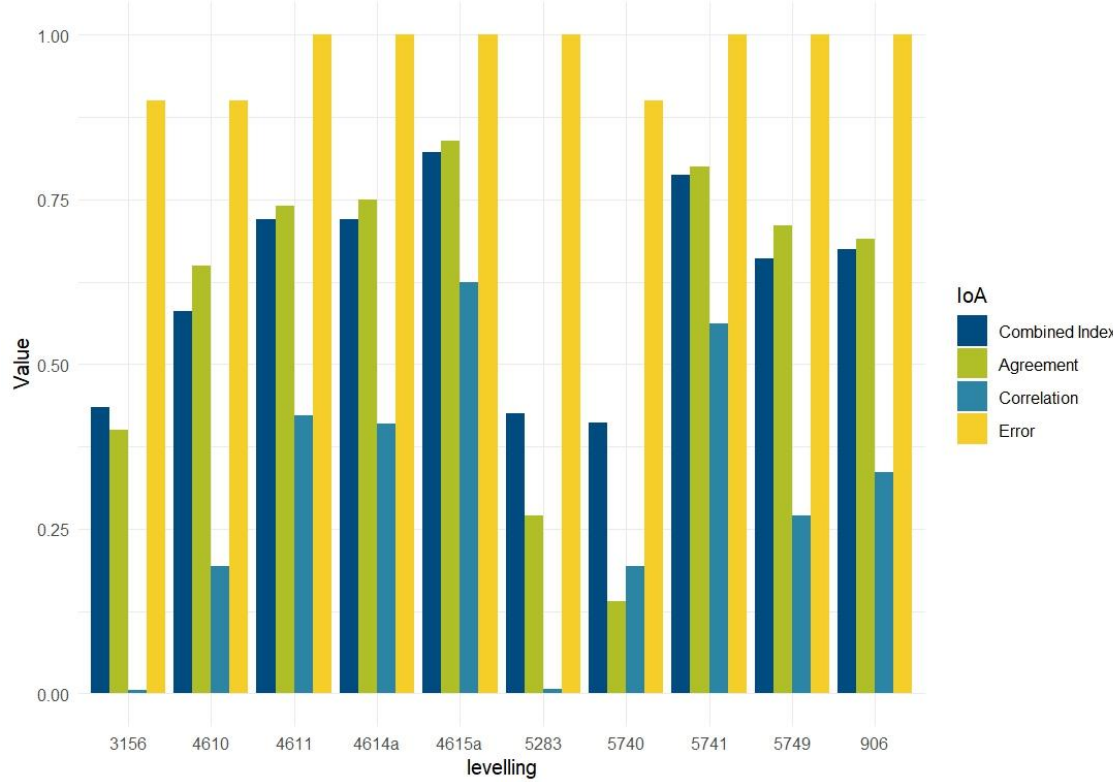


Figure 3.30: IoAs for time series comparison – 10 selected levelling stations are considered.

Station 5741, along with station 4615a, show high performance compared to other stations, with combined indices over 0.75. Conversely, stations 3156, 5283, and 5740 have a combined index below 0.5.

Figure 3.31 and Figure 3.32 present the time series comparison between levelling and EGMS at stations 5741 and 3156, respectively. In Figure 3.31, the two datasets exhibit general consistency, with a discrepancy of approximately 7 mm observed in 2023. However, considering the accuracy of levelling measurements, this difference falls within acceptable limits, indicating consistency in the overall results. In Figure 3.32, the comparison between EGMS and in-situ levelling time series at station 3156 reveals a difference of approximately 1 cm, which is still satisfactory considering the level of accuracy of the in-situ measurements.



Figure 3.31: Comparison of in-situ levelling time series at station 5741 with EGMS Calibrated/L2b data for descending track 037.

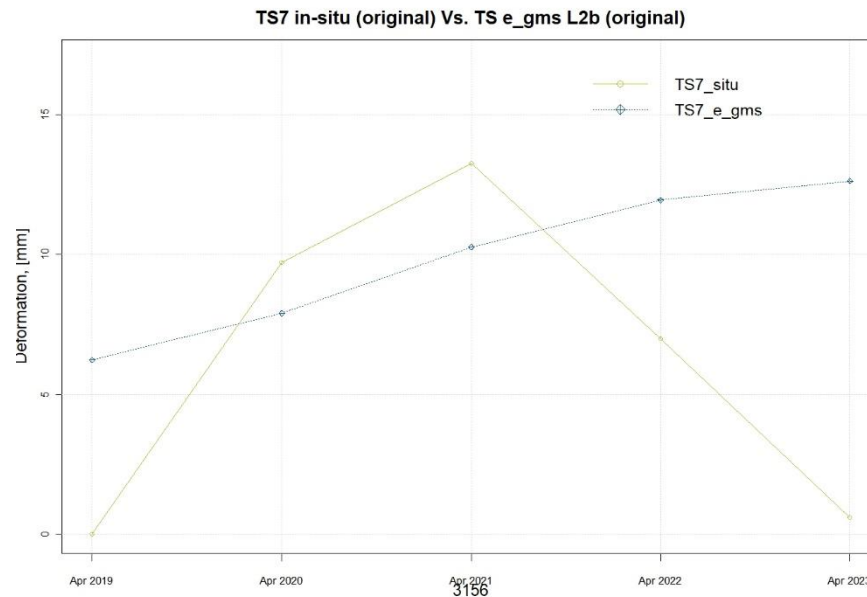


Figure 3.32: Comparison of in-situ levelling time series at station 3156 with EGMS Calibrated/L2b data for descending track 037.

Figure 3.33 provides the averaged IoAs estimated for the time series over the 10 stations; all orbits and EGMS products are considered. An improvement compared to the [previous EGMS update](#) in terms of IoA metrics is first observed, except in the case of the Ortho/L3 vertical component.

The descending data (track 037) exhibit the highest IoAs, likely due to their steeper incidence angle that are more suitable for comparison with levelling measurements, which exclusively capture vertical ground movements.

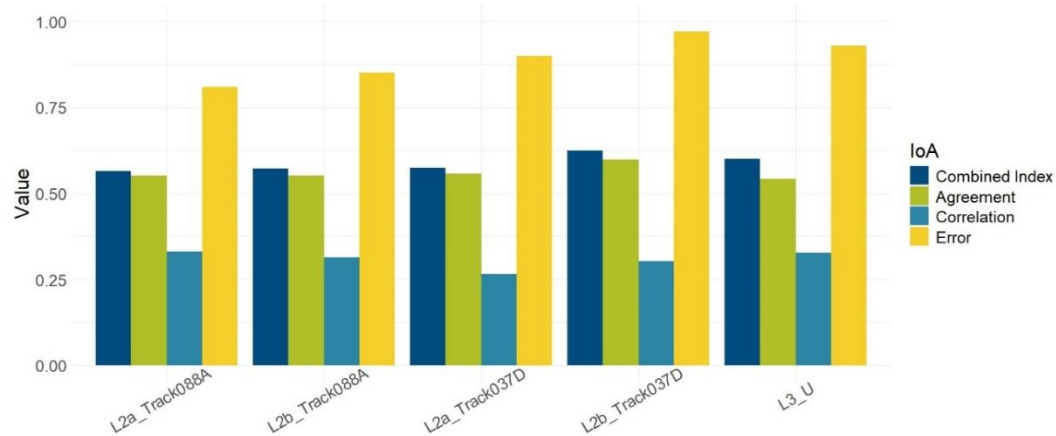


Figure 3.33: IoAs for the time series results for the Lorraine case study (In-situ levelling versus EGMS Basic/L2a, Calibrated/L2b and Ortho/L3 products).

*The presence of expansive clay in a portion of the western sector of Lorraine (“le Porcelette”) introduced a seasonality trend which translated into an underestimation of the uplift rate in the EGMS velocity and time series. However, overall, the EGMS has shown consistency with annual levelling measurements of ground uplift in post-mining areas.*

### 3.2.2 Turow (Poland)

Turow, located at the Czech Republic and Polish border, stands as the second largest active coal mine in Poland. The mining activity is depleting water supplies and damaging nearby houses due

to induced subsidence. The extensive network of water boreholes established to monitor the impact of the open-pit coal mine on its surroundings (36 boreholes 1997-2023) are used for validation purposes. However, only 15 stations from this network correspond to the monitoring period 2019-2023 (Figure 3.34).

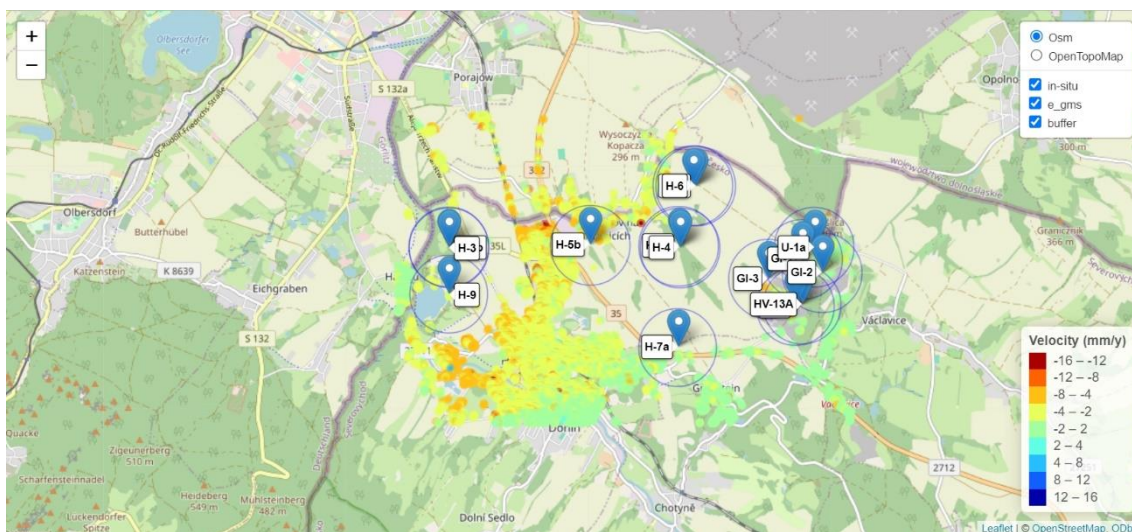


Figure 3.34: Turow validation site showing the Calibrated/L2b EGMS product track 095, the piezometer position, and the 500-m buffer drawn around it.

The ground water levels are measured regularly twice a year. The measurement is expressed in meters above sea level of the heads of the water table for each time step. The methodology proposed by Boni et al. (2016) was applied, additional information is provided in section 2.3.1.2. Two sets of ascending orbit data (tracks 073 and 146), one set of descending orbit data (track 095) and Ortho/L3 up-down were available. Figure 3.35 presents IoA metrics for various piezometers, displaying only Calibrated/L2b products along track 073, which performed the worst. Across the piezometers, the combined index varies from 0.27 to 0.62.

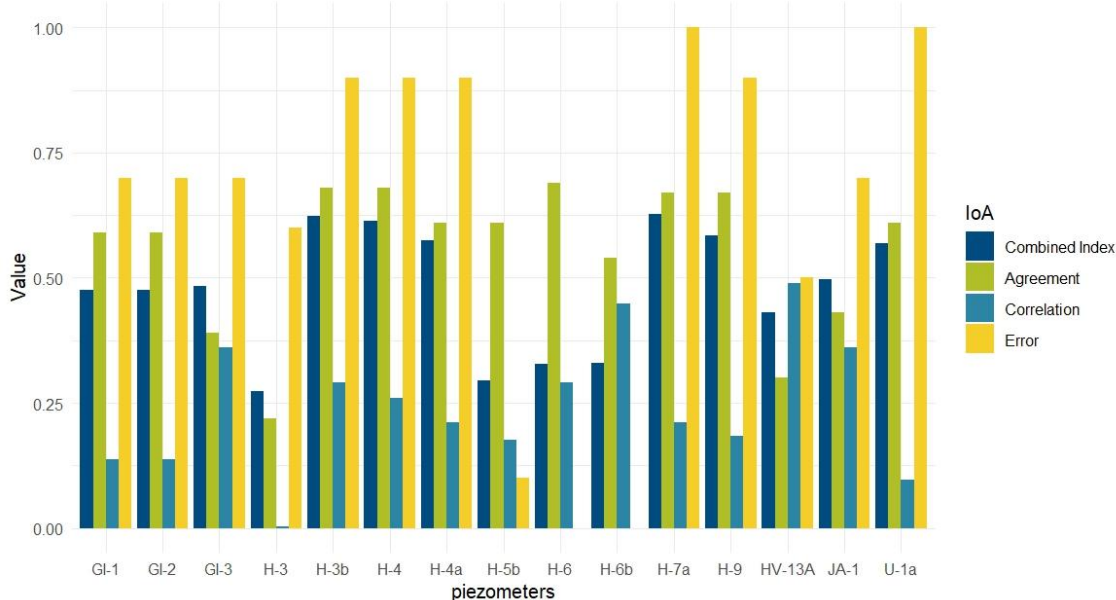


Figure 3.35: IoAs for time series comparison of the 15 piezometers for Calibrated/L2b track 073.

Figure 3.36 to Figure 3.39 illustrate the comparison between adjusted piezometer measurements (in mm/y) and the time series of the best matching MPs within a 500 m buffer. Piezometers H-3b, H-9, H-6, and H-3 are considered.

There is strong agreement between the two types of measurements for the H-3b and H-9 piezometers, with close alignment in both velocity and trend (Figure 3.36 and Figure 3.37). In the case of H-9, minor discrepancies can be observed after the end of 2022, which may be attributed to some noise in EGMS measurements (Figure 3.37).

In piezometer H-6 (Figure 3.38), more differences can be observed between the two time series. EGMS time series show a similar trend change than in the case of H-9 piezometer.

In Figure 3.39, piezometer H-3 shows moreover non-linearities that EGMS does not capture properly. This issue has already been noted in the [2018-2022 update report](#).

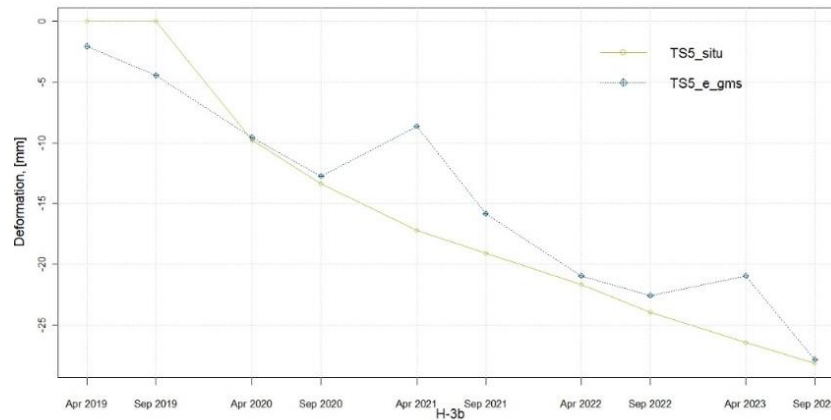


Figure 3.36: Comparison between EGMS Calibrated/L2b measurements calculated along the ascending track 073 and in-situ piezometer time series TS5-H-3b.

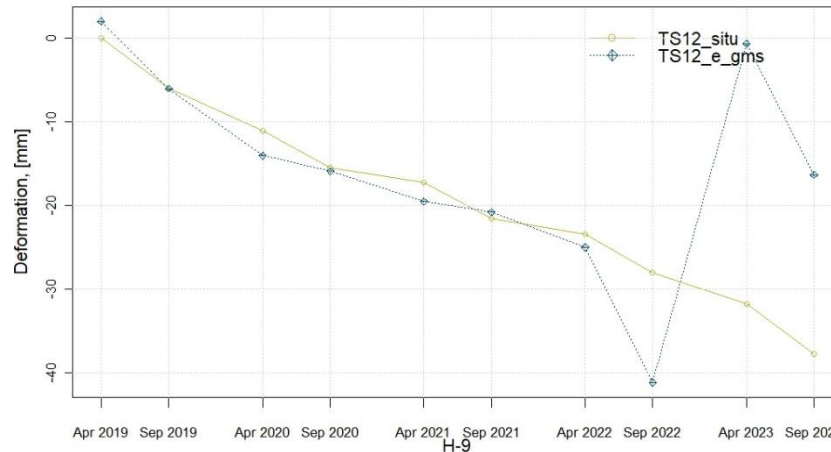


Figure 3.37: Comparison between EGMS Calibrated/L2b measurements calculated along the ascending track 073 and in-situ piezometer time series TS12-H-9.

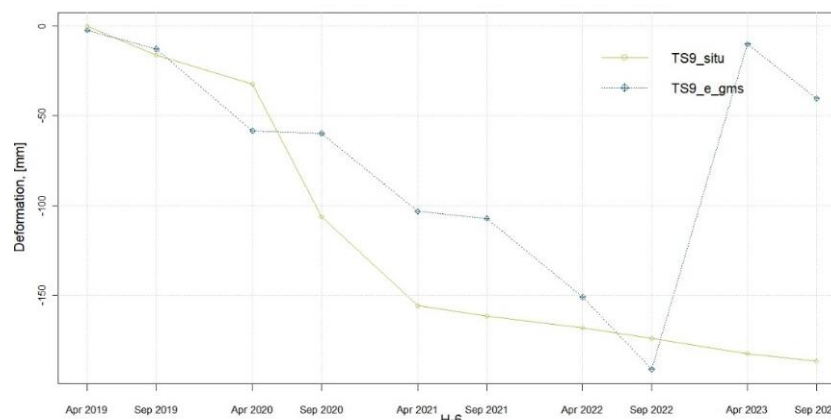


Figure 3.38:Comparison between EGMS Calibrated/L2b measurements calculated along the ascending track 073 and in-situ piezometer time series TS9-H-6.

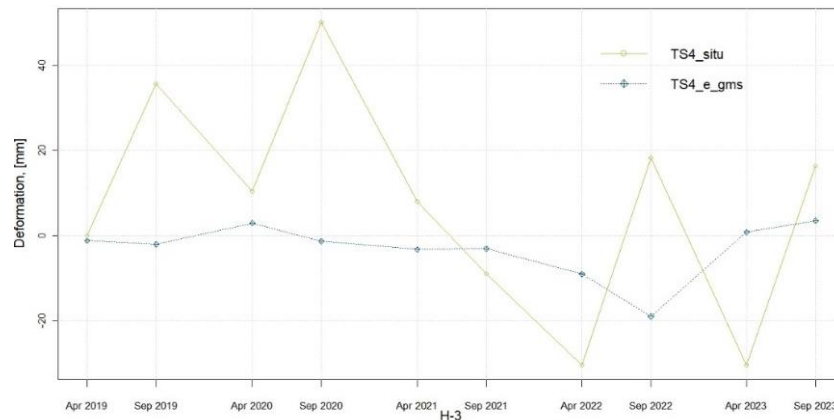


Figure 3.39: Comparison between EGMS Calibrated/L2b measurements calculated along the ascending track 073 and in-situ piezometer time series TS4-H-3.

The IoA metrics, averaged across all piezometers are displayed in Figure 3.40, and for Basic/L2a, Calibrated/L2b and Ortho/L3\_UD. Error scores are generally higher (i.e., lower MAE) than other metrics and Ortho/L3\_UD shows the highest IoA values overall.

Performances are lower for the Calibrated/L2b product in the ascending track 073. This can be associated to the way the IoA is calculated, by selecting the EGMS MP within each piezometer's influence radius and then minimizing the MAE between in-situ and satellite data.

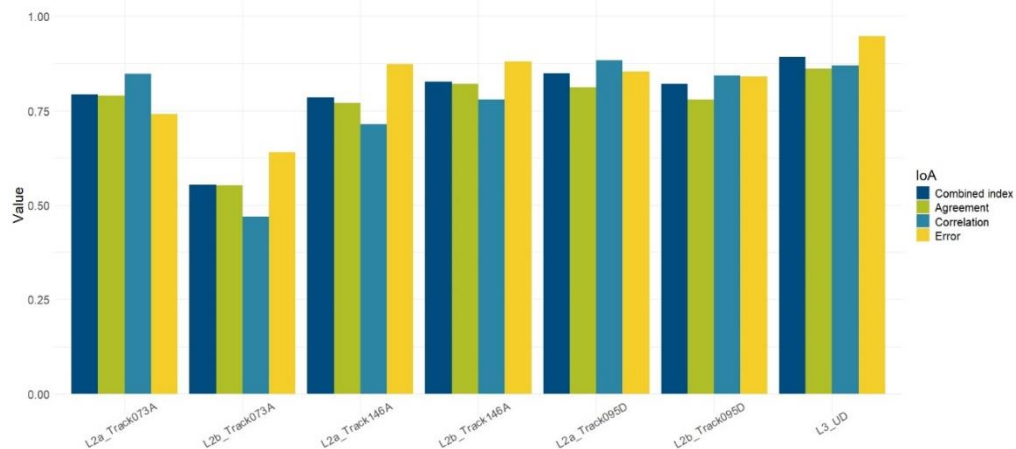


Figure 3.40: Indexes of Agreement for the time series results for Turow: Basic/L2a, Calibrated/L2b and Ortho/L3 compared to the in-situ piezometer dataset.

*Overall, the combined index indicates high consistency for all the EGMS products evaluated with the only exception of track 073 Calibrated/L2b. An isolated piezometer, the H-3, exhibits poor performance across multiple EGMS products due to its non-linear deformation trends.*

### 3.2.3 Guadalentín basin, Lorca Region (Spain)

A comparison between EGMS measurements and the water level change (in meters a.s.l.) is performed for Lorca.

The data used for validation were collected from three boreholes equipped with piezometers (Figure 3.41). Those piezometers measure the fluctuation of the groundwater table four, five, and six times a year at irregular intervals. The measurements are expressed in meters above sea level of the heads of the water table for each time step.

The methodology presented by Ezquerro et al. (2020) was used to evaluate the capability of EGMS in capturing vertical motion affecting the Lorca region. The L3\_UD component is compared with piezometer measurements.

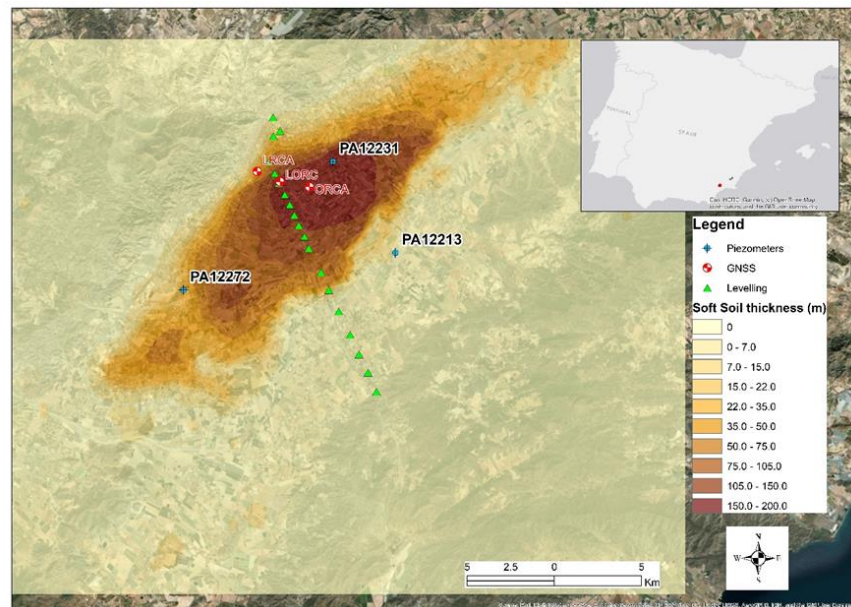


Figure 3.41: Lorca study case showing levelling, GNSS and piezometer positions.

IoA metrics are computed for each piezometer and displayed in Figure 3.42. In particular, piezometer PA12213 shows low performances.

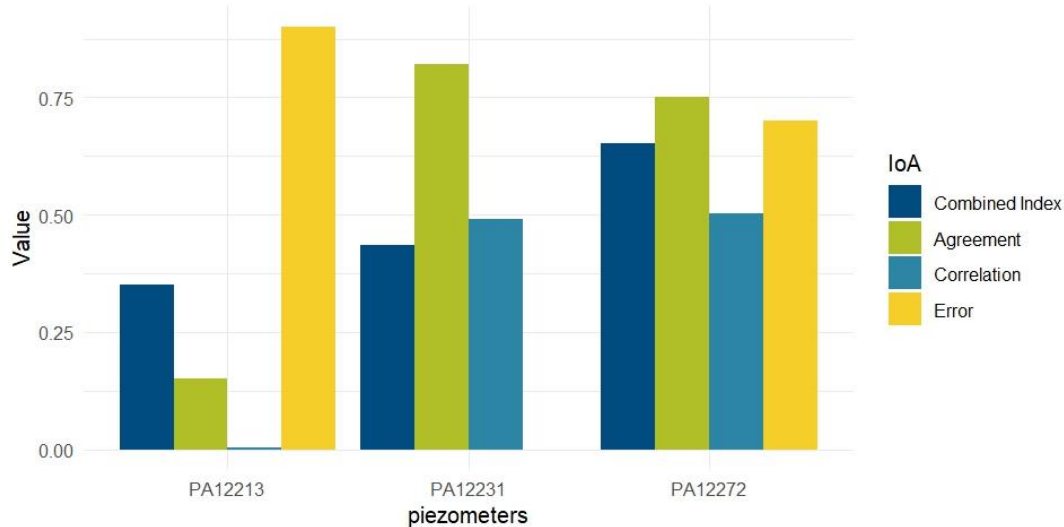


Figure 3.42: IoAs for time series comparison of the 3 piezometers for the L3/Ortho.

Piezometer PA12213, located in the shallower soil area, measures a 10 mm subsidence over five years (Figure 3.43). The discrepancy with EGMS measurements, which do not properly capture the non-linearity of the piezometer time series, leads to the lowest error score and impacts global performance. A similar mismatch can be observed for piezometer PA12272 in Figure 3.44, although the global performance in terms of IoA metrics is better.

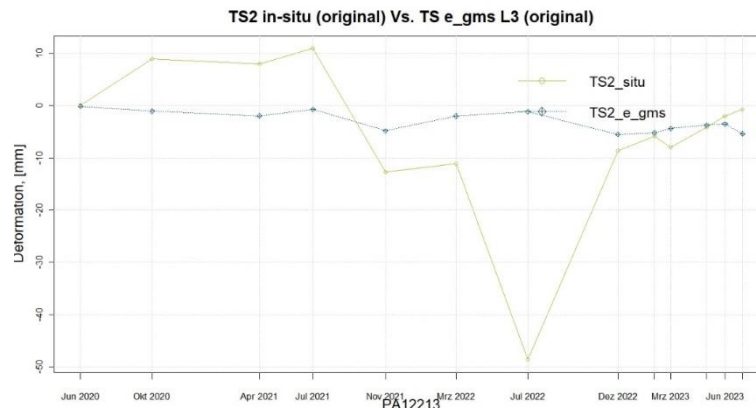


Figure 3.43: Time series plot of piezometer number PA12213 against the EGMS Ortho/L3 MP.

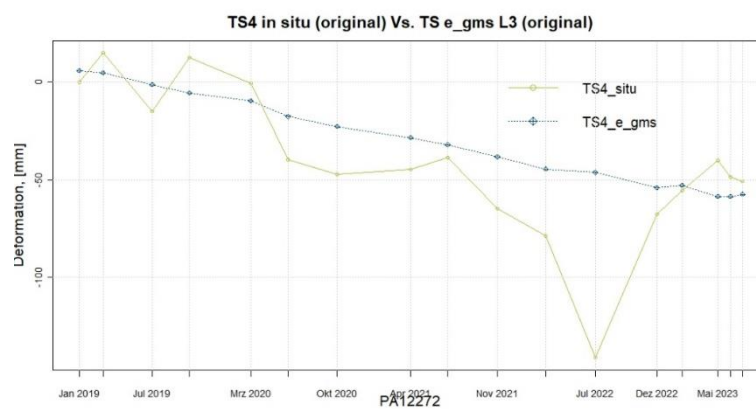


Figure 3.44: Time series plot of piezometer number PA12272 against the EGMS Ortho/L3 MP

The global IoA metrics, computed for all piezometers, are displayed in Figure 3.45. The combined index is equal to 0.48, demonstrating moderate consistency, while the agreement metric scores slightly higher (0.57).

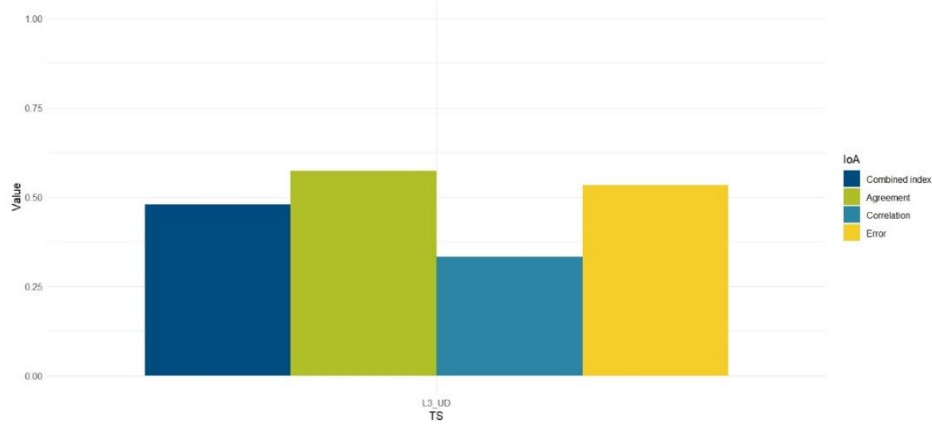


Figure 3.45: IoA corresponding to the time series results for the Lorca case study (in-situ versus EGMS Ortho/L3 products).

*Despite the limitations of the technique in capturing strong non-linearity, EGMS demonstrates its capability to follow the seasonality that the groundwater exploitation induced in the water table oscillations with good accuracy.*

### 3.2.4 Navis (Austria)

Since August 2013, an Automatic Tracking Total Station system (ATTS) has been installed to monitor 80 points across the Navis landslide area. For comparison with EGMS products, data from five of the stations are used. The ATTS system measures X, Y and Z components of deformation, systematically recording daily displacement measurements (in mm/day). The device has an accuracy of approximately  $\pm 5.4$  mm per year.

Figure 3.46 shows the Navis area with a 50m buffer around each station.

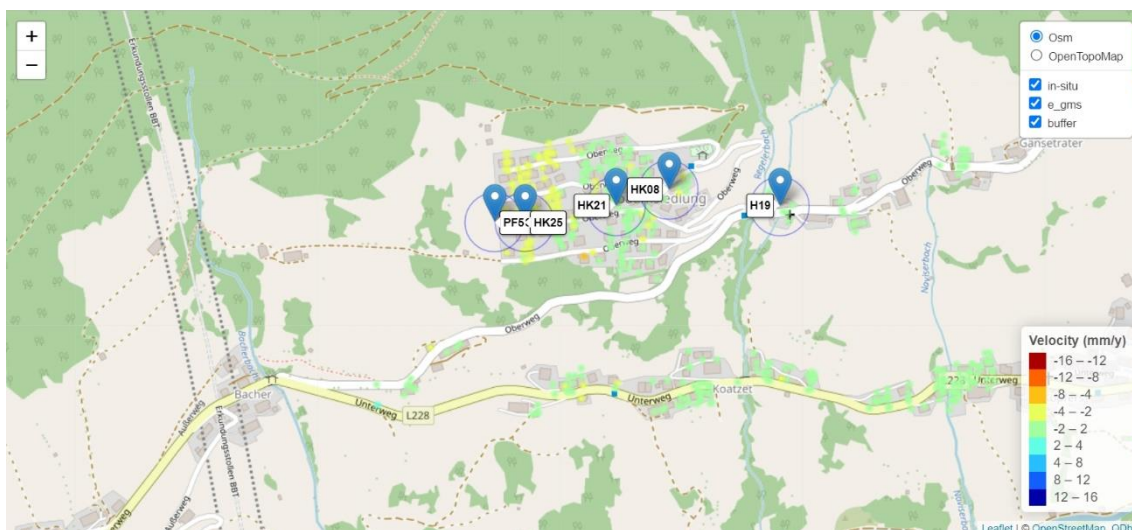


Figure 3.46: EGMS Calibrated/L2a Descending track 168 MP distribution in Navis and position of the in-situ stations.

Figure 3.47 presents a daily time series for the three-dimensional components of the ATTS station TS1 - PF5S. The data indicates a movement towards the south, with a cumulative displacement of 38 mm over a period of 5 years.

SAR satellites have an intrinsic limitation to measure horizontal motion in the north-south facing slope due to their side looking angle (toward the east and the west) acquisition geometry. In Navis, the primary motion direction is southwards (Figure 3.47). The velocity and time series were converted from in-situ measurements (East-West, North-South, Vertical) to LOS under the assumption that southward displacement is the dominant component, minimizing vertical and east-west motions. Therefore, the north-south deformation rate was assumed to be zero.

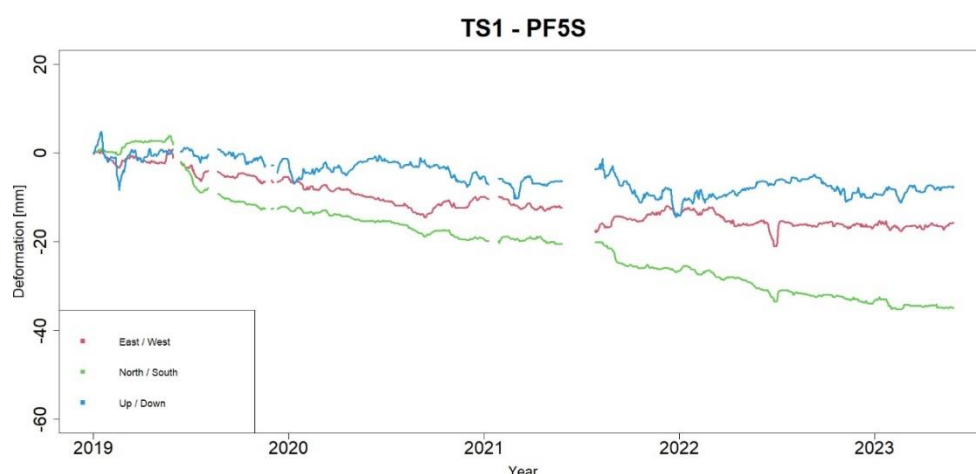


Figure 3.47: ATTS time series for station TS1 – PF5S (filtered data). Source:  
<https://geoinformation.tirol.gv.at/client/?projekt=kerschbaumsiedlung>.

Velocity estimated by EGMS and ATTS were compared and a global IoA computed. Figure 3.48 shows the global IoA metric, across all stations, for Basic/L2a, Calibrated/L2b and Ortho/L3 products; both orbits are also considered. First observation concerns the important difference of performances between the ascending and descending orbits. This may also have an impact on the fact that L3\_EW performs worse than L3\_UD. No significant difference is observed between Basic/L2a and Calibrated/L2b products.

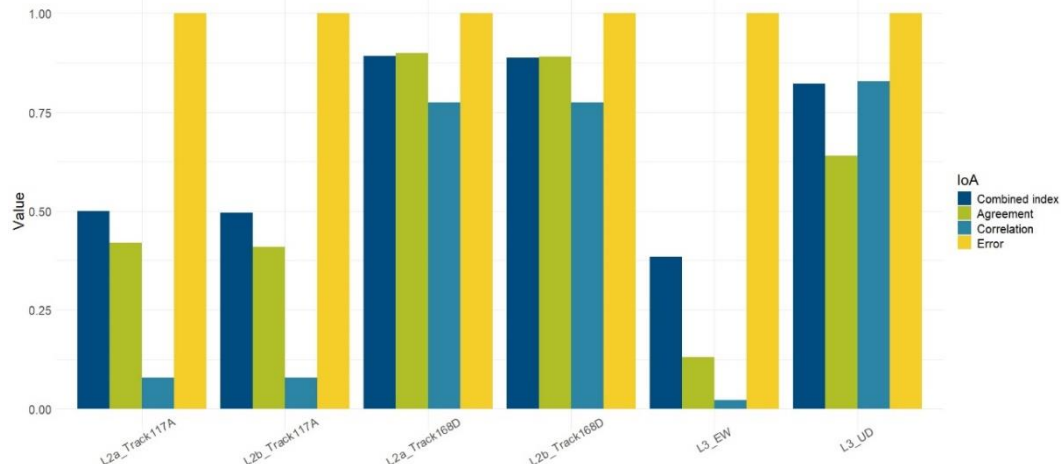


Figure 3.48: Indexes of Agreement for the velocity inter-comparison results in the Navis case study:  
Basic/L2a Calibrated/L2b and Ortho /L3 data.

The difference in performance between the ascending and descending modes is further investigated. The IoA validation metrics for the descending track 168 are displayed in Figure 3.49, Basic/L2a are considered. The computed error value of 1 indicates a MAE value lower than 5mm.

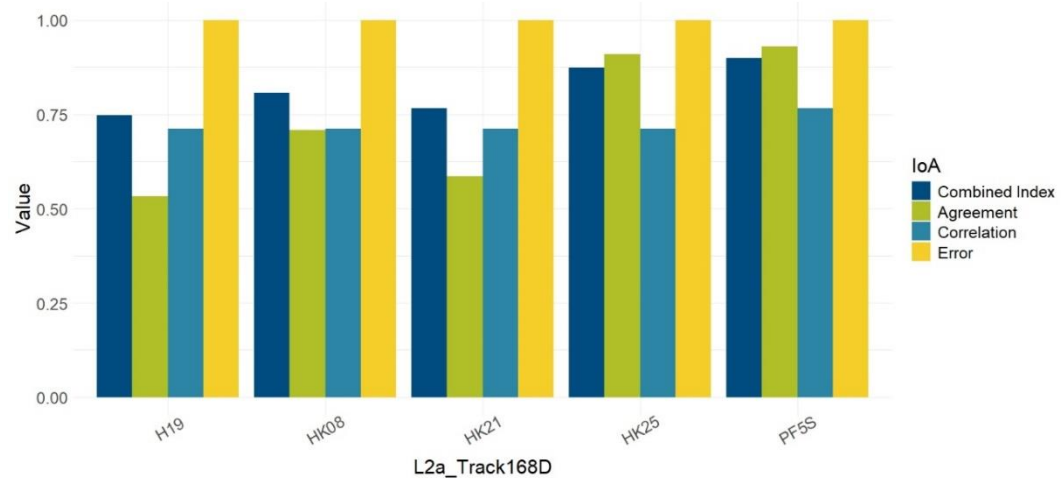
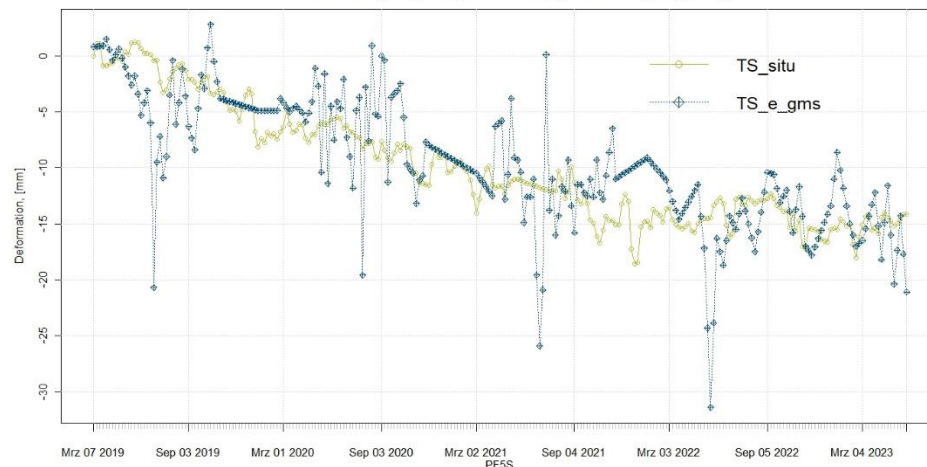


Figure 3.49: Indexes of Agreement for the time series results in the Navis case study: Basic/L2a  
(descending track 168) compared with 5 total stations (H19, HK08, HK21, HK25, PF5S).

Among the five ATTS stations, PF5S achieved the best performance; the good agreement with EGMS time series is confirmed by Figure 3.50. This result is likely due to the position of the point measured by the ATTS, which is situated on the ground for this particular station, whereas it may not be the case for the other stations (Figure 3.46).

**TS1 in situ (original) Vs. TS e\_gms L2a (original)**


**Figure 3.50:** Comparison of in-situ TS1-PF5S time series against the against the EGMS Basic/L2a descending track 168.

The ascending track 117 is considered in Figure 3.51. Globally the performances are worser than in the descending orbit (Figure 3.49). This may be related to the fact that the western part of Navis is characterised by less deformation, with a cumulative displacement of 17 mm in 5 years. The EGMS might detect the motion but underestimate it due to the exposure of the site (with an aspect south and south-west) and the east looking viewing direction of the ascending data. Stations H19 and HK21 show a combined index above 0.5. Station H19 is further considered in Figure 3.52. Despite residual noise, EGMS results capture the overall trend of in-situ measurements, though with an underestimation of about 5 mm.

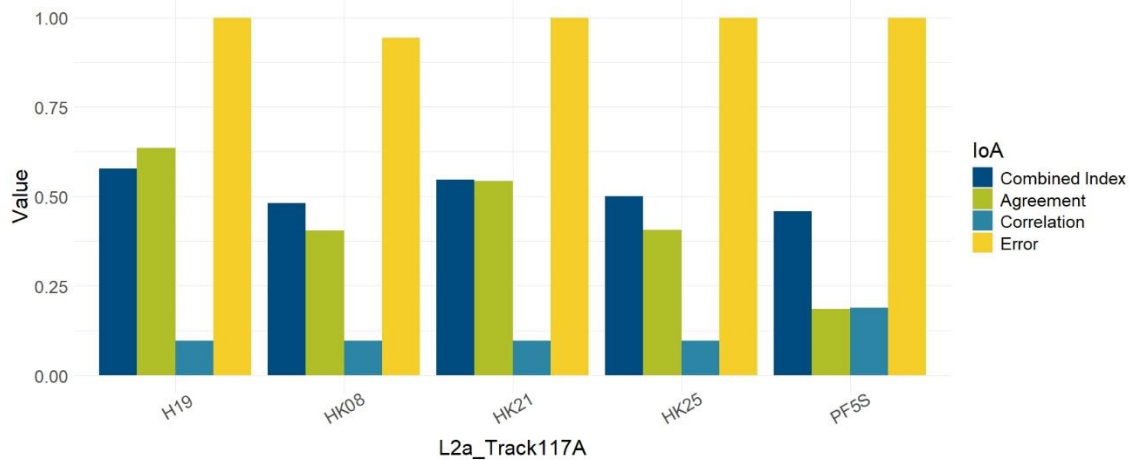


**Figure 3.51:** Indexes of Agreement for the time series results in the Navis case study: Basic/L2a (ascending track 117) compared with 5 total stations (H19, HK08, HK21, HK25, PF5S).

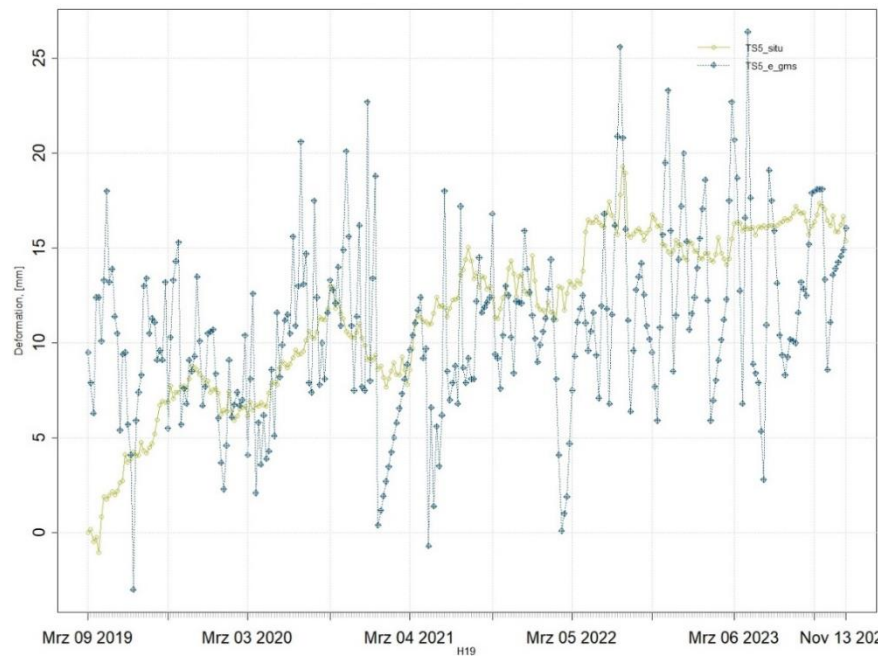


Figure 3.52: Comparison of in-situ TS5-H19 time series against the against the EGMS Basic/L2a ascending track 117.

Figure 3.53 shows the IoAs for all the time series inter-comparison in Navis, where a difference between the performances in ascending and descending orbits is evident and, again, L3\_EW scores less than L3\_UD.

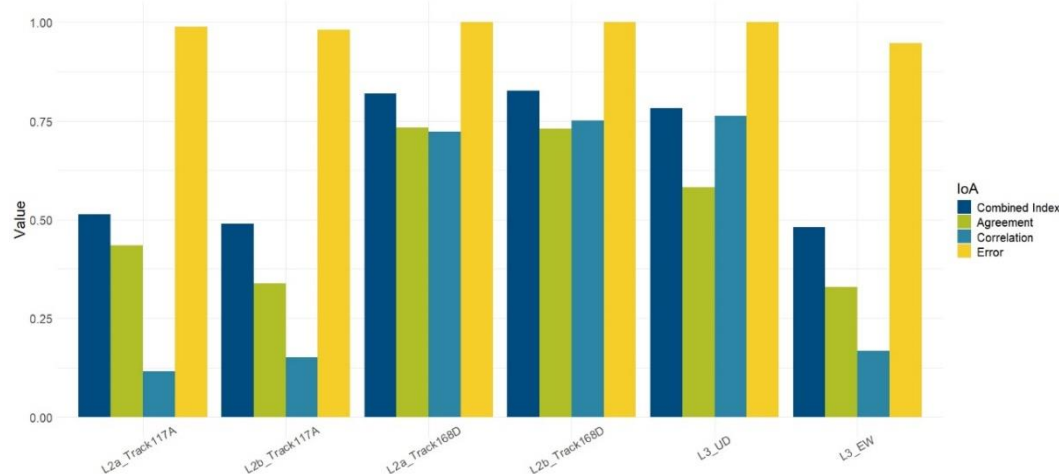


Figure 3.53: Indexes of Agreement for time series inter-comparison results in the Navis case study: Basic/L2a, Calibrated/L2b and Ortho/L3 data.

---

*In conclusion, despite the natural constraints of Navis (south orientation of the slope), this validation site reached a level of agreement of over 0.75 in both velocity and time series. The only exception is the ascending orbit data and the Ortho/L3 East-West that have to be handled with carefully for south and southwest-oriented landslides.*

---

### 3.3 Height and position validation by comparison with CRs

#### 3.3.1 Thyborøn (Denmark)

Thyborøn exhibits notable subsidence rates exceeding 7 mm/year, particularly in its south-eastern parts. Recent measurements include CRs linked to a levelling network (Figure 3.54). This network serves to calibrate satellite-based deformation measurements, offering crucial data for EGMS validation. The image in the bottom right corner shows an example of the type of CR deployed in Thyborøn.

Nine CRs are expected to be visible in the current EGMS products being validated (2019-2023). The CRs are double trihedral reflectors made from 60x60x120 cm square aluminium/iron plates with double geometry, suitable for both ascending and descending satellite paths (Figure 3.54). Moreover, there have been three levelling campaigns (2021, 2022 and 2023) relevant to this release of the EGMS. Because of the high corner reflector density for the current EGMS comparison, Thyborøn has been selected for assessing geo-positioning accuracy.

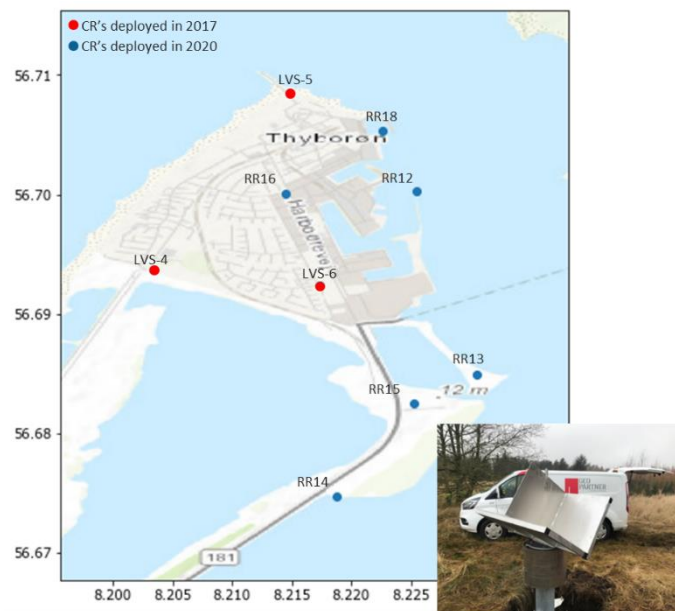


Figure 3.54: Map of the Thyborøn Peninsula with the eight corner reflectors (CRs) locations.

Figure 3.55 shows an example of EGMS MPs time series located around the 'LVS4' and 'LVS5' CRs, along with the estimation of the MP time series most likely to be the CR. Table 3.1 summarizes the metrics (mean square error) and the probability that a given MP near a CR location corresponds to the actual CR. This probability is computed for the five closest points to the CR. Note that these CRs were installed in 2017, therefore covering the full period of the current EGMS update. Geolocation accuracy is determined by estimating the distance between the CR and the EGMS MP most likely to be the CR. The distance is computed using the three-dimensional Euclidean distance, considering the x, y, and height coordinates.

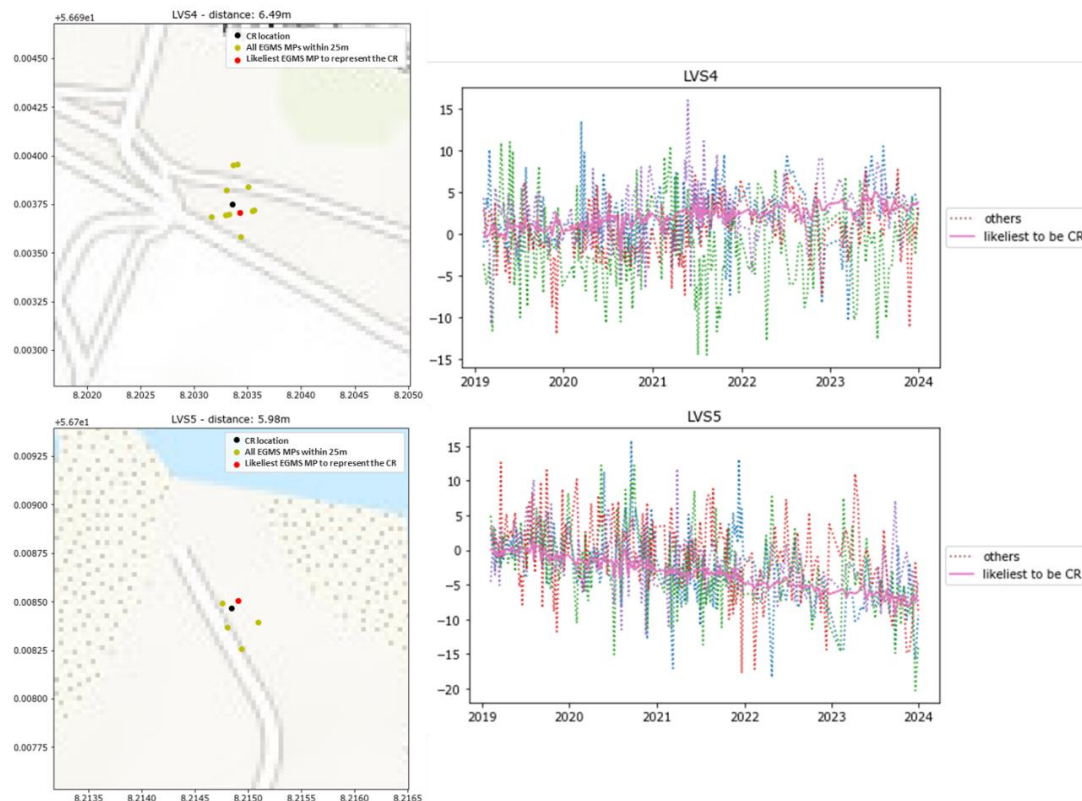


Figure 3.55: Example of time series and location of EGMS MPs around the 'LVS4' and 'LVS5' corner reflectors (CRs).

Table 3.1: Probability estimation of each MP being the CR for 'LVS4' and 'LVS5' corner reflectors (CRs). MSE is the Mean Squared Error.

LVS4			LVS5		
Distance (m)	MSE	Probability of CR (normalised)	Distance (m)	MSE	Probability of CR (normalised)
5.71	7.14	0.0	5.92	12.19	0.0
6.49	0.44	0.99	5.98	0.34	1.0
6.96	15.61	0.0	10.85	14.53	0.0
8.86	5.85	0.0	17.38	15.38	0.0
12.23	8.33	0.0	24.1	7.74	0.0

Considering all tracks and the estimated distances between the CR and the MP corresponding to the CR, the estimated mean error is 10.77 m, which is close to the geolocation accuracy requirement of 10 m, as defined by the EGMS production tender specifications. While the choice of the CR is straightforward for some locations, it is less evident for others; this is illustrated by Figure 3.56.

Figure 3.56 and Table 3.2 show examples of a clear choice for a CR point. A single EGMS MP was within 25 meters of the 'RR18' CR location, deployed on 19-08-2020. This deployment date coincides with the observed noise decrease in the green time series of CR 'RR18' in Figure 3.56. Note that the MSE for the MP at this CR is still high, which is likely to be the effect of this CR not being present in nearly 1,5 years out of the 5 years of time series coverage. In the same figure, the CR 'RR14' shows that it is sometimes less evident to determine the best MP candidate from the time series analysis. Moreover, Table 3.2 shows that different possible candidates show similar probabilities. Among all the CRs evaluated across the four analysed tracks (two ascending and two descending), selecting the EGMS MP for the CR 'RR14' presents a unique challenge. For this specific CR in descending track 139 the probabilities of the selected MP being representative of a CR are low. While the other two MPs have probabilities that are close to representing the

CR as well. When selecting the MP with highest probability of being CR 'RR14', the estimated distance difference is 16.3 m. As shown in Figure 3.56 (bottom-left) and Table 3.2 two other MPs are closer to the CR than the selected MP, with distances below 9 meters. If one of these other two MPs, despite having lower but statistically significant probabilities, had been chosen, the geolocation accuracy would have decreased.

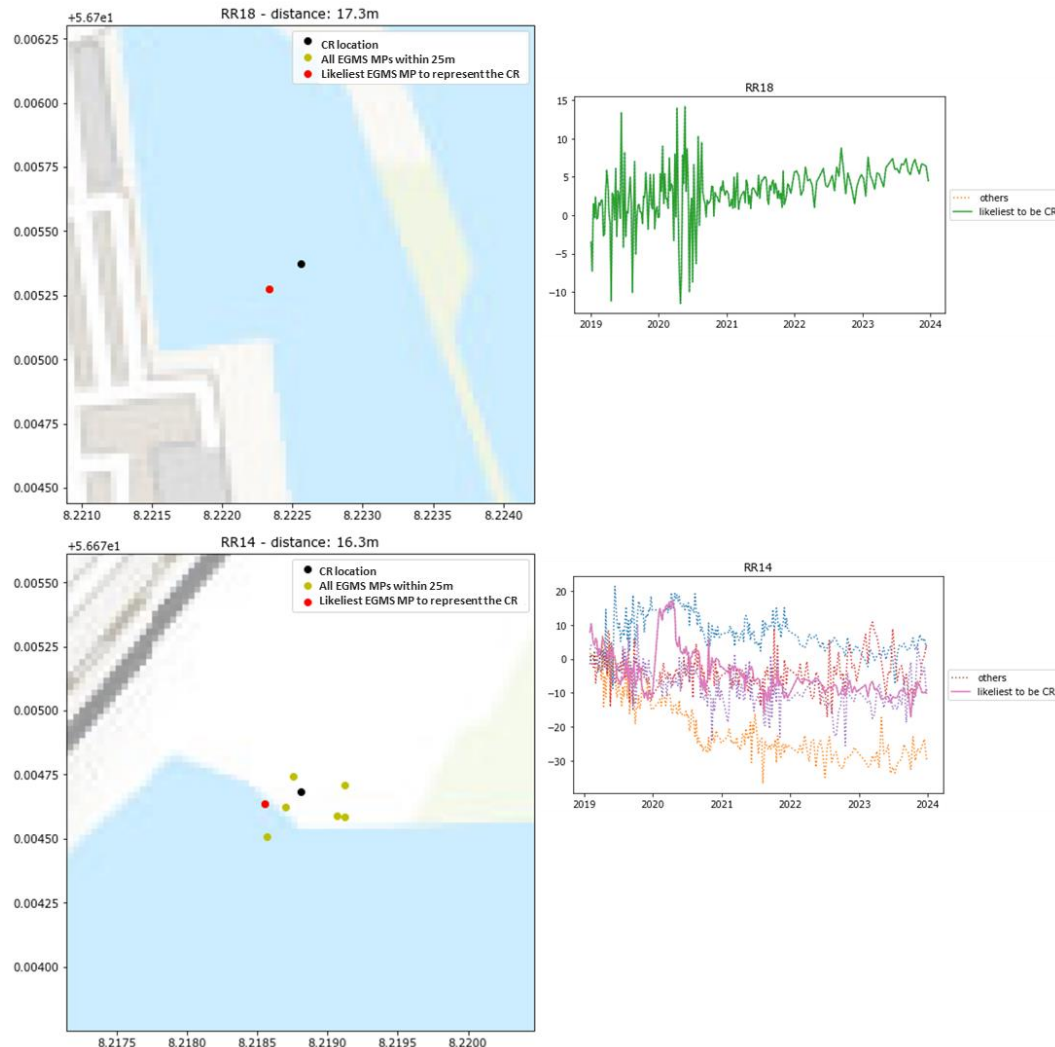


Figure 3.56: Example of time series and location of EGMS MPs around the 'RR18' (descending track 037) and 'RR14' (descending track 139) corner reflectors (CRs).<sup>2</sup>

Table 3.2: Probability estimation of each MP being the CR for 'RR18' and 'RR14' corner reflectors (CRs).

RR18		
Distance (m)	MSE	Probability of CR (normalised)
17.27	9.56	1.0

RR14		
Distance (m)	MSE	Probability of CR (normalised)
7.37	8.05	0.38
9.49	8.56	0.23
16.3	8.0	0.39
19.01	13.84	0.0
19.31	14.58	0.0

<sup>2</sup> Note that the background map is for reference only and does not accurately depict the CRs and MPs location, which are not on the water.

In the following analysis, the Basic/L2a products acquired along two ascending, and two descending tracks are examined and compared with levelling data for both time series and velocity estimations. This comparison is conducted under the assumption that the EGMS LOS displacements of the Basic/L2a products at the Thyborøn Peninsula are purely vertical.

Figure 3.57 illustrates an example of the velocity estimation correlation between the levelling at each CR location and the Basic/L2a EGMS values of the MP corresponding to the CR. This activity is performed for each orbit covering the Thyborøn Peninsula. The black full line indicates the perfect agreement between the velocity measured via levelling and EGMS. The dashed line represents the best-fit line between all CRs.

For all the tracks, the correlation is high, except for CR 'RR13' (visible in asc015, desc037, desc139). The higher discrepancies are observed in ascending track 015 and descending track 139, with velocity differences between EGMS and levelling estimation of approximately 4 mm/year.

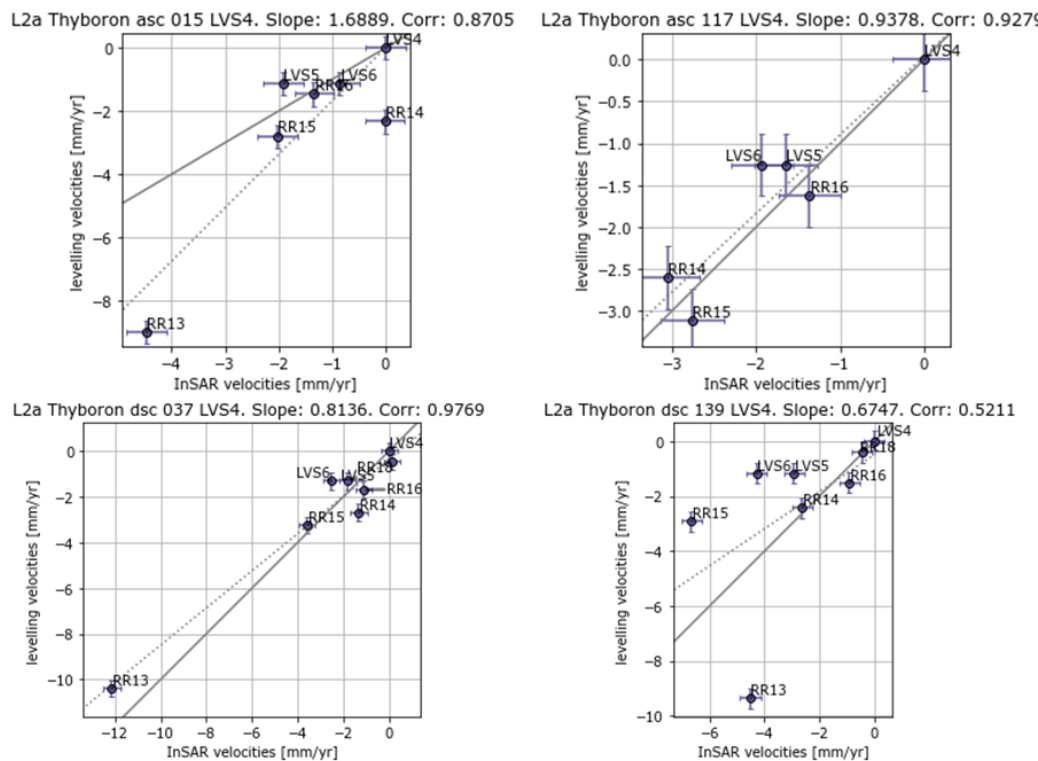
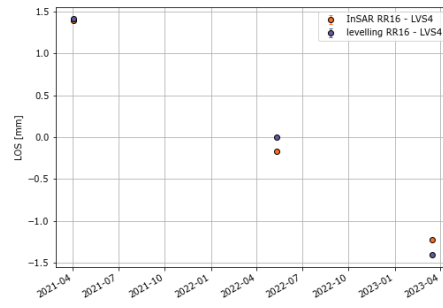


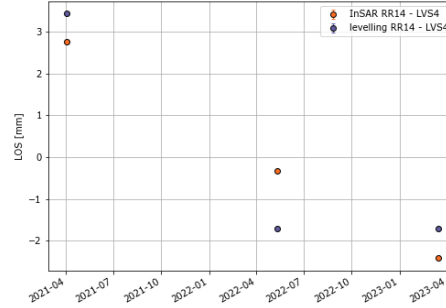
Figure 3.57: Correlation between EGMS and levelling velocities.

Figure 3.58 and Figure 3.59 show the results of the time series displacements comparison between the EGMS MP selected as the CR and levelling measurements at that specific CR. This comparison was limited to Basic/L2a products, employing the double differences method with 'LVS4' as the reference point. It is worth noting that only three dates of levelling measurements are available, for this reason, the mean velocity is less reliable due to the limited number of data points available. A best-case (high velocity correlation) and a worst-case (low velocity correlation) are proposed for the ascending and descending orbits, respectively.

As already observed in Figure 3.57, the levelling benchmark shows the lowest velocity correlation at CR 'RR13', for which the maximum estimated displacement difference between EGMS results and levelling reaches 6 mm in the descending track 139. Overall, the time series in Figure 3.58 and Figure 3.59 show that, despite some differences, time series exhibit comparable results and confirm a consistent downward linear trend between EGMS and levelling.

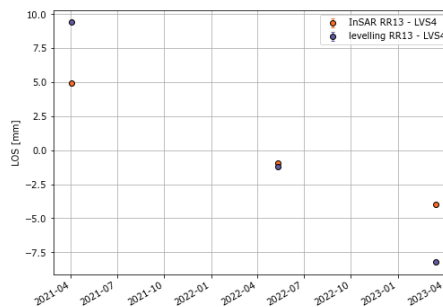


a) Case of CR 'RR16' in asc track 015.

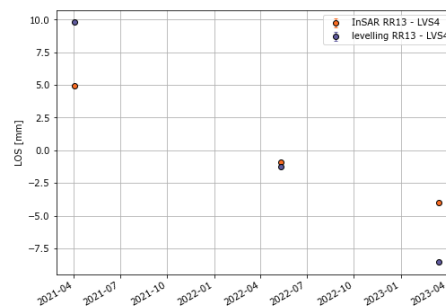


b) Case of CR 'RR14' in desc track 139.

Figure 3.58: Examples of time series displacements of stations with high velocity correlation between EGMS and levelling for ascending and descending orbits.



a) Case of CR 'RR13' in asc track 017.



b) Case of CR 'RR13' in desc track 139.

Figure 3.59: Examples of time series displacements of stations with low velocity correlation between EGMS and levelling time series for ascending and descending orbits.

The analysis indicates consistency between the levelling measurements and the EGMS time series estimation. This comparison is particularly valuable because it enables the evaluation of EGMS time series at CR locations, even though only three levelling measurements are available.

### 3.3.2 Indre Nordnes, Jettan and Gámanjunni (Norway)

The validation sites of Indre Nordnes, Jettan and Gámanjunni, are situated within landslide prone mountain areas in Troms and Finnmark County, in northern Norway. Because of the high risk of landslides, several monitoring systems have been deployed to acquire continuous, real-time, or periodic (with weekly intervals) measurements. Five CRs were installed at each of the three test sites, with continuous GNSS measurements taken either at or near these locations. Figure 3.60 shows these sites with Indre Nordnes (one CR with 'IN' initials), Jettan (three CRs with JT initials) and Gámanjunni (one CR with GT initials) mountains with satellite background. The Google Maps satellite image shows Jettan CR survey stations (JT-SAT-4, JT-SAT-3, JT-SAT-2). JT-SAT-4 is in a heavily vegetated area at the westernmost point. The ID numbers were kept as used by the [Norwegian Water Resources and Energy Directorate \(NVE\)](#), and the corresponding GNSS stations do not have 'SAT' in the name. On the right bottom corner an image of one of the CRs is shown.

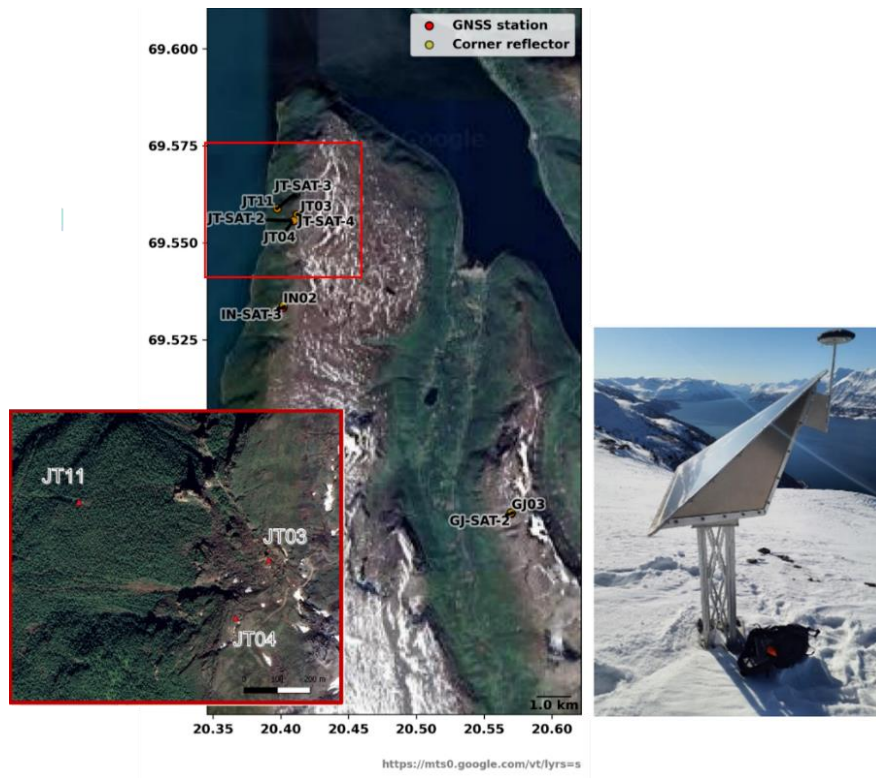


Figure 3.60: Map of the Norwegian corner reflector (CR) site.

The GNSS time series data have been analysed and compared with the ones of the MPs located nearby. Due to the lack of compatible GNSS data for evaluating the Calibrated/L2b product, comparisons were limited to the Basic/L2a product when assessing the five existing stations against the three EGMS products.

The GNSS station JT11 was selected as the reference station to evaluate the performance of the Basic/L2a product (descending orbit, track 168). The locations of the GNSS stations differ from those of the CRs, with distances ranging from 2 to 60 meters. As a result, GNSS measurements may not always correspond to CR measurements, particularly for GNSS stations located beyond the resolution of the EGMS LOS products (i.e., 20x5 meters) or those situated further away from the CRs. A 100-m search radius around the CR was then considered for the comparison (see [D6-Validation Methodologies](#)), in order to take into account these specificities.

Figure 3.61 illustrates the double differences between EGMS MPs and the GNSS stations JT04, JT03, J03 and IN02, using station JT11 as a reference. Winter dates are excluded to maintain coherence with EGMS time series, resulting in the visible observation gaps during the winter months. The figure shows that overall, EGMS time series closely match the GNSS observations within their error bars, derived using all the datapoints falling within the 100m-search radius.

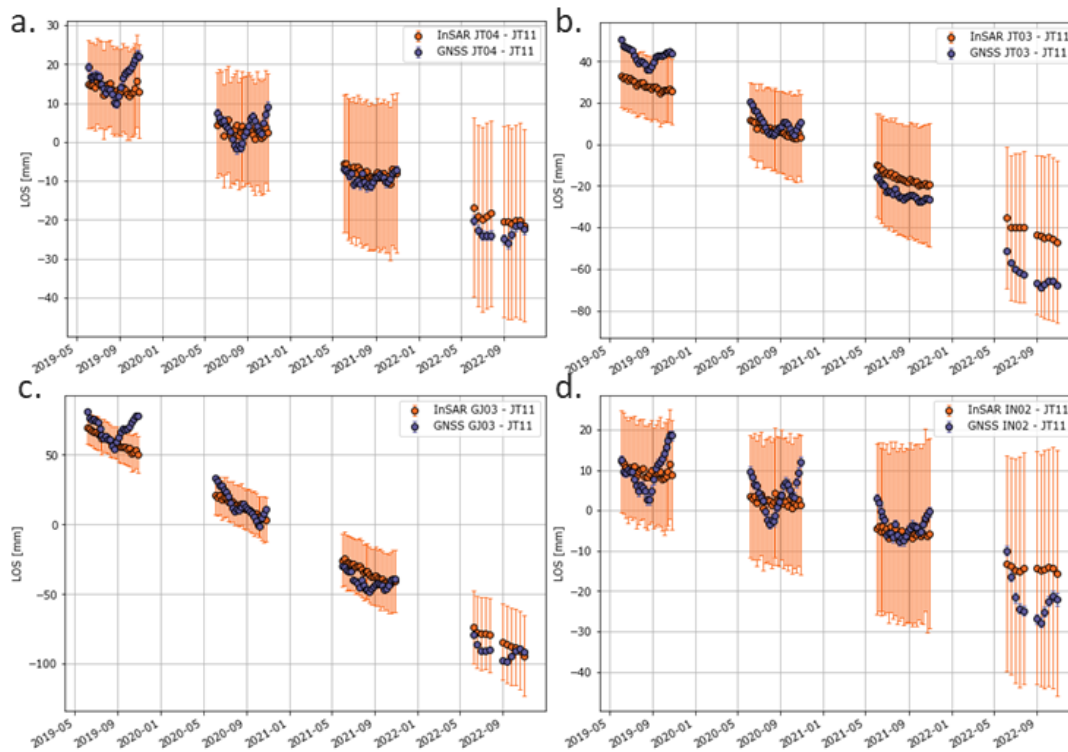


Figure 3.61: Examples of time series double differences between three of the stations for Basic/L2a descending track 095.

GNSS and EGMS times series are further assessed by subtracting the GNSS and EGMS time series for each pair of stations; the result is displayed in Figure 3.62. Red lines indicate a one-sigma deviation interval. Ideally, the subtraction between the time series should be around zero. Time series differences around zero are obtained for stations JT04 and IN02, indicating an excellent agreement. Station JT03 shows an underestimation of the EGMS with respect to the GNSS of approximately 30 mm in 5 years of observations (c.a. 6 mm/year). The results of the differences between EGMS and GNSS time series generally fall within a one-sigma deviation or one standard deviation from the mean.

Figure 3.63 illustrates the correlation in velocities between EGMS and GNSS. The black full line indicates perfect agreement between the two types of measurements and corroborates the results shown in previous figures. Dashed line indicates the best fit line between all stations. The graph confirms Figure 3.62 results. The velocity estimation at station JT03 and JT04 slightly deviates from the ideal correlation (black filled line), indicating that the EGMS velocities are lower than those measured by GNSS. For station JT03, the average difference of the velocity between EGMS and GNSS for all orbits is about 15 mm/year while for JT04 is lower, about 9 mm/year. The EGMS velocity at stations JT04, JT11 and IN02 almost matches the GNSS estimation.

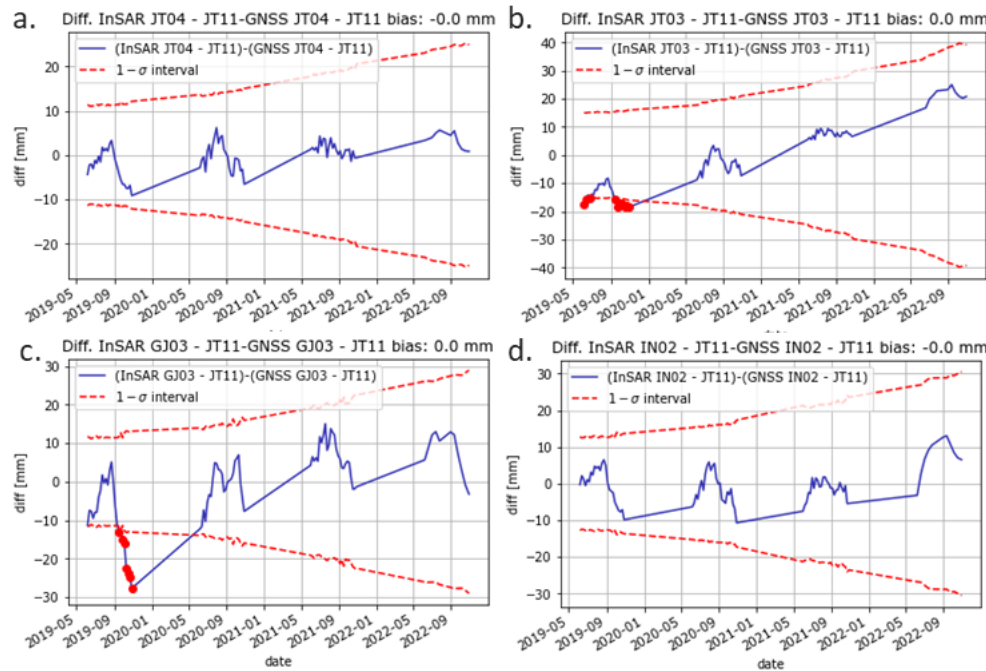


Figure 3.62: Differences between the EGMS and the GNSS double differences time series.

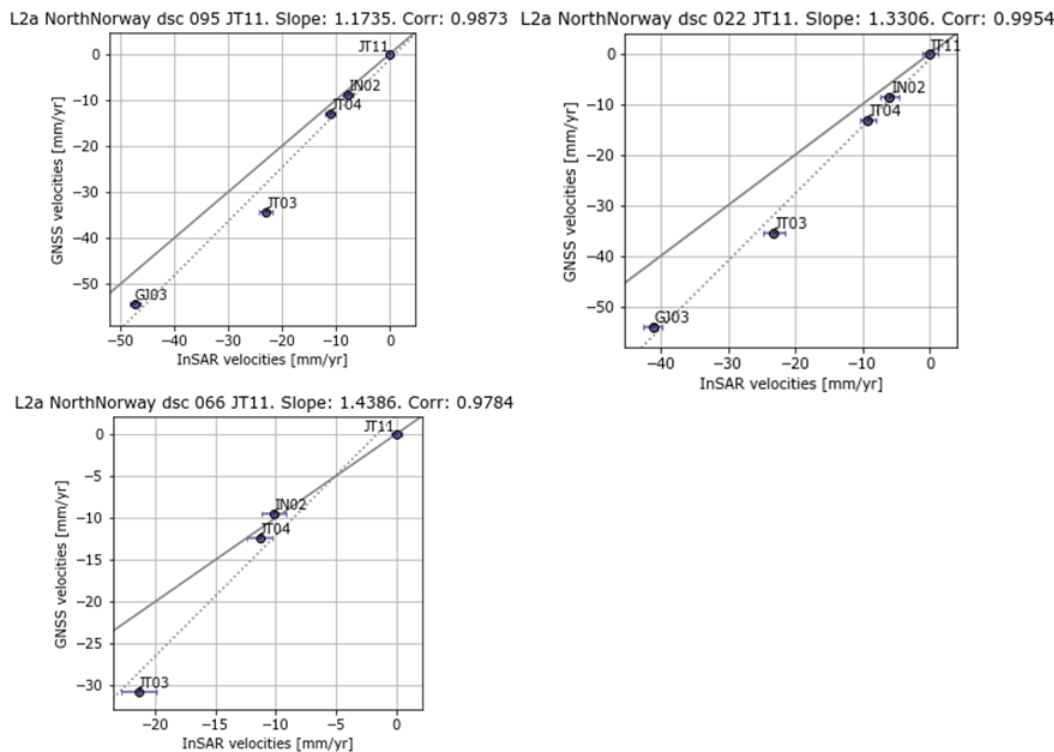


Figure 3.63: Correlation between EGMS and GNSS velocities.

Overall, the velocity correlation for all studied stations is on average 0.98, indicating that the Basic/L2a and GNSS estimated velocities generally align well. Basic/L2a products are recommended for landslide applications, and one station should be selected as reference because the GNSS and the Basic/L2a product are in different reference systems. If there are not enough GNSS stations or no stations at all, double differences between EGMS observations can be performed between MPs outside and inside the location of a potential landslide. An advantage of high-latitude locations is the orbit overlapping, as in the case of North Norway



where three orbits might be available for the same area. The optimal orbit pair (ascending or descending) should be used depending on the aspect of the mountain slope.

---

*For this validation site, there is a good correlation of velocity estimation between EGMS and the GNSS measurements close to the CR (Figure 3.63). However, two stations, GJ03 and JT03, stand out as outliers. The average velocity difference between GNSS measurements at the CR and the EGMS product is approximately 5 mm/year, which is relatively significant. The outlier stations GJ03 and JT03 contribute to this average with velocity differences of 10.2 mm/year and 11.7 mm/year across all tracks, respectively. Despite these discrepancies, the time series data from EGMS and GNSS remain within one standard deviation from the mean, indicating consistency between the two methods. These findings confirm the suitability of the EGMS for monitoring landslides, particularly in high latitude regions that benefit from multiple overlapping orbits.*

---



## 4 RESULTS - APPLICABILITY AND USABILITY VALIDATION

This section is designed to assess the applicability of the EGMS product in characterizing specific phenomena within the defined thematic areas of the EGMS Service, adhering to its specifications. The EGMS is compared to other high-resolution and geo-localised data sources such as:

- Other operational and quality-controlled Ground Motion Services (GMS) or InSAR results, to study and compare EGMS's ability to capture known deformation trends and phenomena.
- High-resolution land cover layers, aimed at exploring the correlation between surface characteristics versus MP density as well as time series attributes quality.
- National inventories of geo-localised phenomena or geohazards, to aid in identifying the kind of phenomena most suitable for representation in the EGMS products.
- Geological, lithological, hydrogeological, geomorphological, and geotechnical maps to correlate observed deformation trends with soil characteristics.
- Aerial photography and high-resolution land cover layers, providing insights into MP density and sensitivity to changes.
- Digital elevation models and derived slope data, enhancing the interpretation of geometrical constraints in the 3D plane.
- Inventories of anthropic activities that can trigger surface motion including mining, quarrying, and water pumping. Matching these with observed EGMS deformation areas helps identifying the phenomena captured by the EGMS.

### 4.1 Landslides

#### 4.1.1 Comparison with other GMS

##### 4.1.1.1 Aosta Valley (Italy)

This region, located in the Italian Alps, experiences a variety of gravitational phenomena including shallow landslides (e.g., debris flows, planar and rotational slides), rockfalls, large slope instabilities and deep-seated gravitational slope deformations.

Figure 4.1 shows a comparison of the displacement velocities between the EGMS and the regional GMS of the Aosta Valley, managed by the local Geological Survey (AVGS), for the Basic/L2a product in ascending track 88. The most recent dataset from AVGS contains acquisitions from April 2019 to January 2024 and has, therefore, a good overlap with the EGMS data period from January 2019 to December 2023. The comparison reveals good agreement between the detected ADAs. However, the AVGS dataset identifies 134 ADAs, while the EGMS dataset results in 51 ADAs. This discrepancy can be at least partially attributed to differences in MP density and coverage. The AVGS dataset seems to have better coverage on many slopes, where vegetation reduces the coherence of scatterers (see Figure 4.1). This difference is most likely due to different processing algorithms and strategies: while the EGMS is optimized for large scale mapping, the AVGS processing is optimized for landslide monitoring, i.e., to map local phenomena.

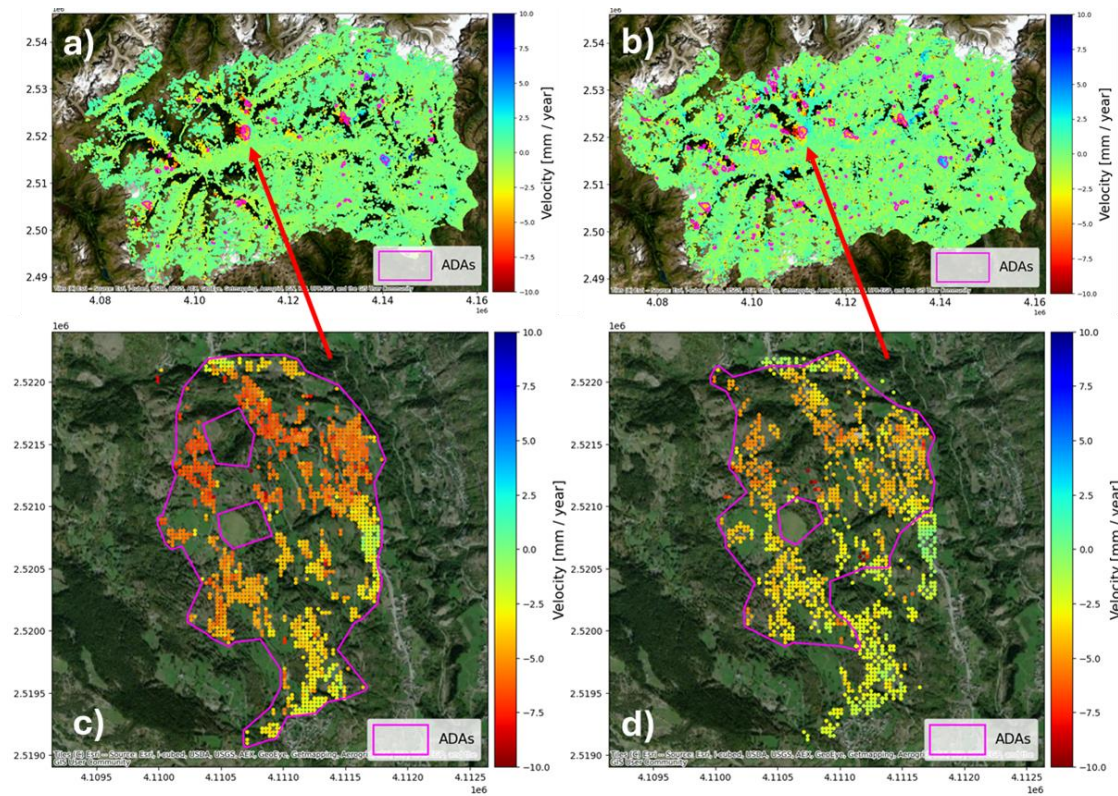


**Figure 4.1:** Displacement comparison for Aosta Valley (Italy): a) Basic/L2a displacement velocities (EGMS, track 88/ASC); b) AVGS displacement velocities. For the ADA marked by red arrows: c) and d) close-ups of corresponding velocity maps.

In the validation for the EGMS baseline ([2015-2021](#)), a difference between the velocity values of the two InSAR products (AVGS/EGMS) for the ascending track 88 was observed along the main valley cutting through the region. The EGMS showed a slight shift towards positive velocities in that valley, which correlated with topography. As it was evident only in the ascending data, it was interpreted as a residual atmospheric signal. The 2019-2023 EGMS update does not show a similar difference, indicating an improvement of the quality of data, as already observed for the [2018-2022 update](#).

Figure 4.2 (a) and (b) show the averaged time series and the velocity correlation for the ADA shown in Figure 4.1. For the ADA comparison, all MPs within the combined ADA area (ADAs in Figure 4.1 (a) and (b)) have been considered as a single polygon area.

The time series show a good agreement in their general trend. The EGMS data exhibits a clear seasonal variation, which is not visible in the AVGS data. This can be explained by the fact that the EGMS deformation model estimates the seasonality, and such seasonality is kept in the final time series, whereas in the AVGS data such a component is not maintained in the final product, as confirmed by the data provider. The velocity correlation in Figure 4.2 (b) also shows a good agreement, as evidenced by the elongated point distribution with a slight shift with respect to the best correlation (i.e. the diagonal red line).

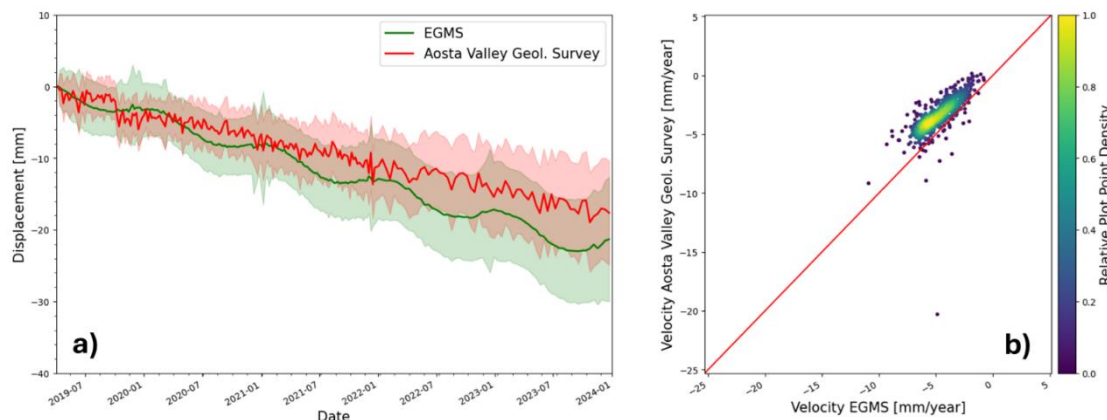


Figure 4.2: a) Average and standard deviation of ADA time series for EGMS and AVGS for the ADA shown in Figure 4.1; b) velocity correlation for area the same ADA.

Table 4.1 presents the averaged validation metrics (described in Table 2.6 and [D6-Validation Methodologies](#)) for all Basic/L2a products that have been compared. The relatively low spatial overlap of 57% can mostly be explained by the better coverage of the AVGS products on some of the mountain slopes. The velocity and time series correlation show a reasonable degree of correlation, the latter being affected by the difference in seasonality, which could be observed for some ADAs. The relative velocity difference of 40% shows that while differences can be observed the velocity values generally agree well.

Table 4.1: Validation metrics for Aosta valley.

Description	Value
Spatial overlap [%]	57.32
Relative Velocity Difference [%]	40.84
Velocity Correlation	0.65
Displacement Time Series Correlation	0.73

---

*Although the comparison between the two datasets reveals some differences (e.g. spatial overlap between moving areas), all major landslide areas are identified, and the time series show an overall good agreement. Some discrepancies in ADA detection may be attributed to variations in MP coverage rather than differences in velocity. The resulting metrics indicate a reasonably good agreement between both datasets suggesting that the EGMS is useful for regional-level landslide mapping activities.*

---

#### 4.1.1.2 Tuscany (Italy)

The validation site in the Tuscany Region (Regione Toscana, RT) covers the provinces of Massa Carrara, Lucca, and Pistoia. As Tuscany is an area particularly prone to landslides, this was the phenomenon of interest for this region.

Figure 4.3 shows a comparison of displacement velocities between the EGMS and the regional GMS of the RT for the Basic/L2a product descending track 168.

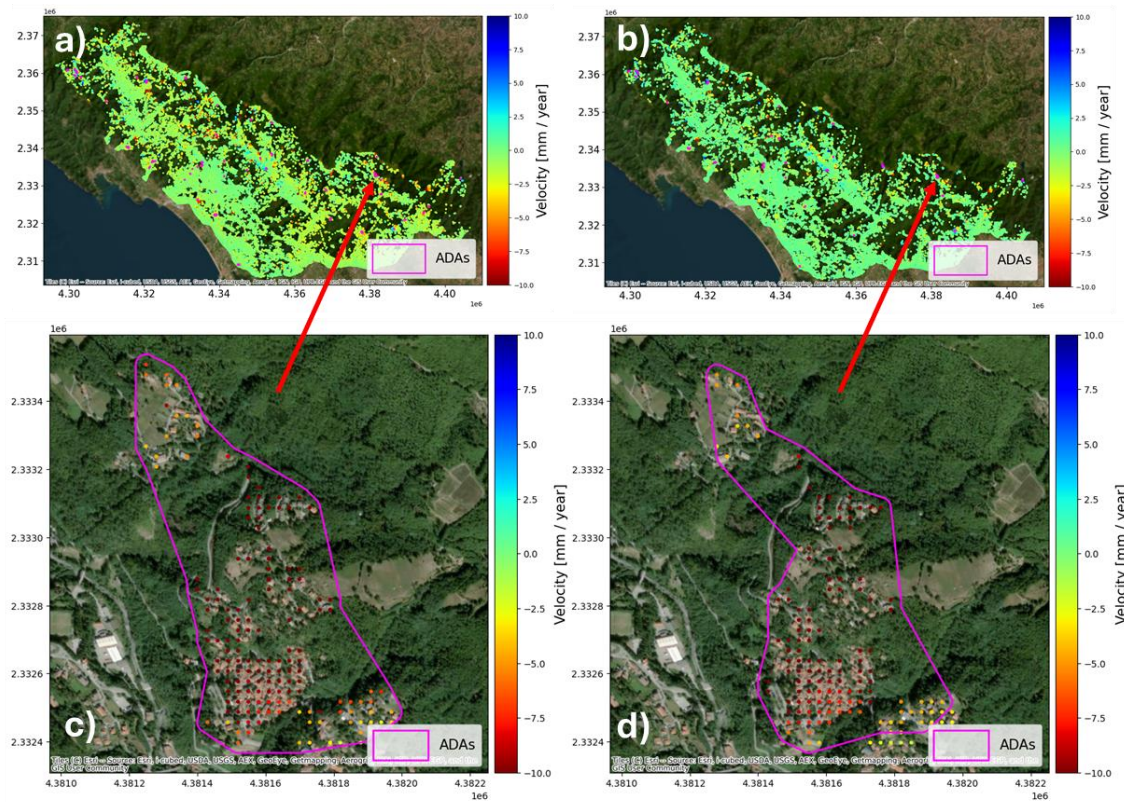


Figure 4.3: Displacement comparison for Tuscany (Italy): a) EGMS Basic/L2a displacement velocities (track 168, descending); b) RT displacement velocities. For the ADA marked by red arrows: c) and d) close-ups of corresponding velocity maps.

The velocity maps show a 0.7 mm/year offset between the two datasets, with EGMS velocity distribution pushed to slightly more negative values than RT measurements, likely due to different reference points. The difference observed is relatively minor and smaller than the offset observed during the comparison of the [2018-2022 update](#). It may still impact ADA detection and subsequently less ADAs have been detected than in the [2018-2022 update](#), with 48 ADAs detected in the EGMS dataset and 28 ADAs in the RT dataset. Overall, there is a good agreement between the datasets especially for larger ADAs, as demonstrated in Figure 4.3 c) and d).

Figure 4.4 a) presents a comparison of the time series for the ADA shown in Figure 4.3 c) and (d). All MPs within the combined ADA area (resulting from the merged ADAs detected in both datasets) have been considered. The two time series show a strong agreement. Moreover, standard deviations for the displacement values are also very similar between the two datasets. Figure 4.4 b) illustrates the spatial correlation of the velocity values. Ideally, the distribution of the points should align with the red diagonal line. A clear linear correlation of the velocity values can be observed, with only a very slight shift from the diagonal towards the RT velocity axis. This is consistent with the observed general velocity offset of only about 0.7 mm/year between the datasets.

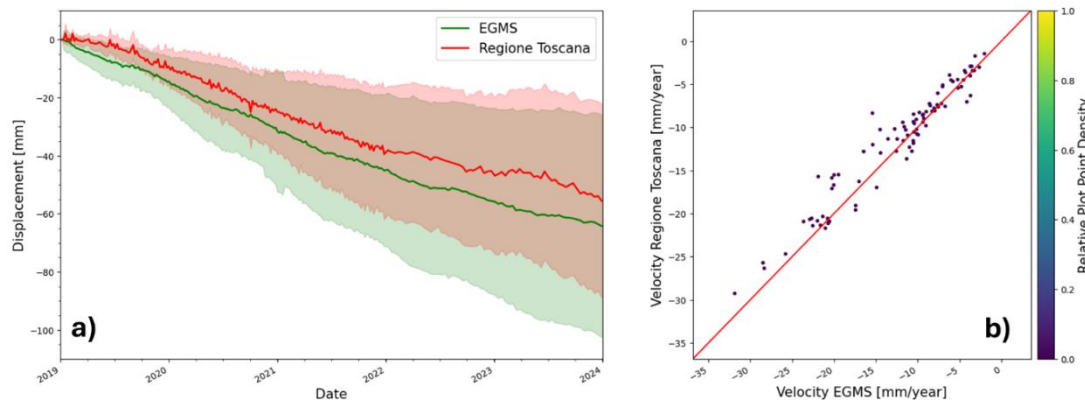


Figure 4.4: a) Average and standard deviation time series calculated from all the MPs making the ADA represented in Figure 4.3 c), for EGMS and RT; b) velocity correlation for the same ADA.

It is worth mentioning that for ascending track 117 a similar offset of ~0.6 mm/year was observed, while ascending track 15 did not show a notable offset (~0.1 mm/year). In these cases, the numbers of ADAs detected in EGMS and in the RT dataset are more similar, with 36 (EGMS) and 30 (RT) ADAs for track 15, and 8 ADAs for both dataset for track 117.

Table 4.2 summarises the validation metrics (described in Table 2.6 and [D6-Validation Methodologies](#)) for the comparison. Although the number of ADAs detected in both datasets has reduced compared to the [2018-2022 update](#), the spatial overlap is of the same order, about 50%. This relatively low spatial overlap should not be regarded as a negative outcome, as it shows that the EGMS is able to detect more ADAs than the RT dataset. A good match is noted for the larger ADAs, suggesting that the low spatial overlap is mainly due to smaller ADAs. A velocity difference of 34% is observed between the two datasets, likely due to observed velocity offset. The correlation of the time series also appears to be very good, suggesting that not only the general trends correspond well, but also non-linear variations over time.

Table 4.2: Validation metrics for Tuscany.

Description	Value
Spatial overlap [%]	50.67
Relative Velocity Difference [%]	33.53
Velocity Correlation	0.67
Displacement Time Series Correlation	0.90

*A general offset of about 0.7 mm/year in the descending product between both datasets was detected. This was improved with respect to the [previous update](#). Differences in the total number of detected ADAs can be observed; however, a good agreement is still obtained for larger ADAs. The ADA time series exhibit a good temporal correlation, and velocity values also correlate reasonably well. Therefore, despite observed differences, the datasets show a good match, confirming the usability of the EGMS for regional-level landslide mapping activities.*

## 4.1.2 Comparison with inventories of phenomena

### 4.1.2.1 Alpes Maritimes (France)

In Alpes Maritimes, national inventories are commonly created by field investigations, sometimes supported by aerial photos or optical satellite imagery. The French national

inventory has recently been updated (2022-2025) in the framework the Agence National pour la Recherche (ANR) project “VIGIMONT” (VIGilance MONTagne: service de prévision de risque glissement de terrain et laves torrentielles en territoire de montagne).

The number of EGMS MPs within landslide areas highly depends on the acquisition geometry (ascending/descending). The use of EGMS L2 products is recommended for landslide motion detection, especially in highly mountainous areas where MP density depends on both acquisition geometry and orientation of topographic slopes. It is important to note that EGMS L2 products correspond to the LOS direction (1 dimension), making them suitable for detecting slow motions ranging from 1mm/year to approximately 20 cm/year, where the full 2D/3D components of the motion are not required. On the other hand, for landslide detection, the direction of motion can be inferred from the slope. Therefore, EGMS L2 results are adequate to detect changes in the ground motion regime (e.g. acceleration or deceleration).

Moreover, North/South oriented landslides might go unnoticed or wrongly characterized when the magnitude of the vertical component of the movement is low. This is a well-known limitation of InSAR, since the technique is less sensitive to ground motion occurring along the flight direction of the satellite. In conclusion, in North/South oriented landslides, there might be confusion between vertical and horizontal motion components, leading to an underestimation of motion velocity in the Ortho/L3 product.

EGMS-derived ADA polygons and inventory points are compared to evaluate the capability of EGMS for landslide detection in the Alpes Maritimes department. Figure 4.5 and Figure 4.6 show that the site of interest in Alpes Maritimes has a significant number of landslides, with over 500 phenomena recorded in the national inventory.

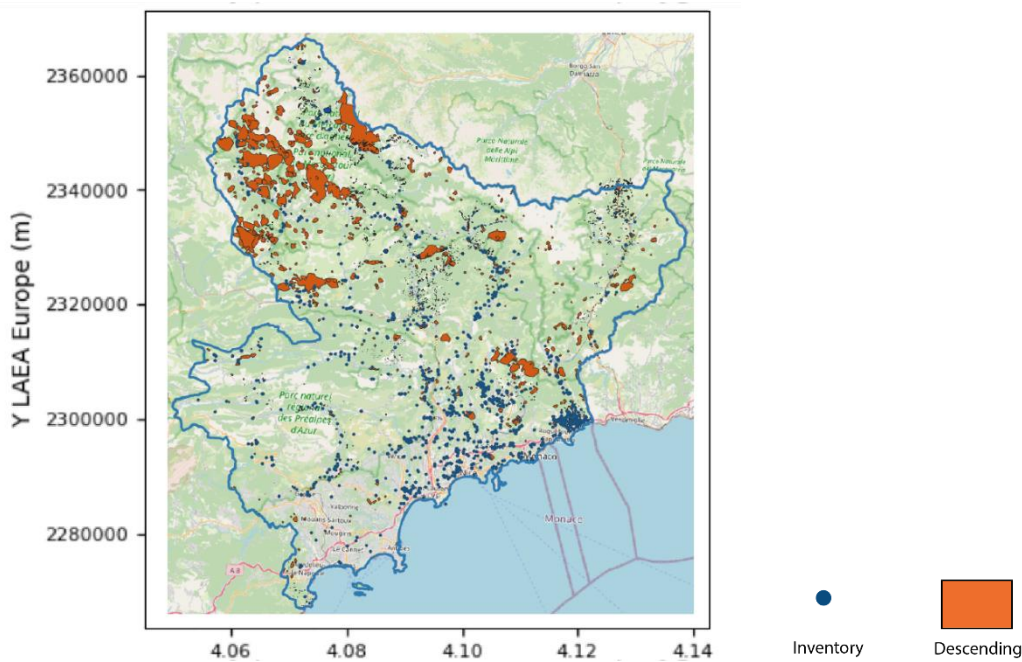


Figure 4.5: EGMS Calibrated/L2b ADAs in descending orbit compared with updated national inventory (blue dots) on the French Alpes Maritimes department.

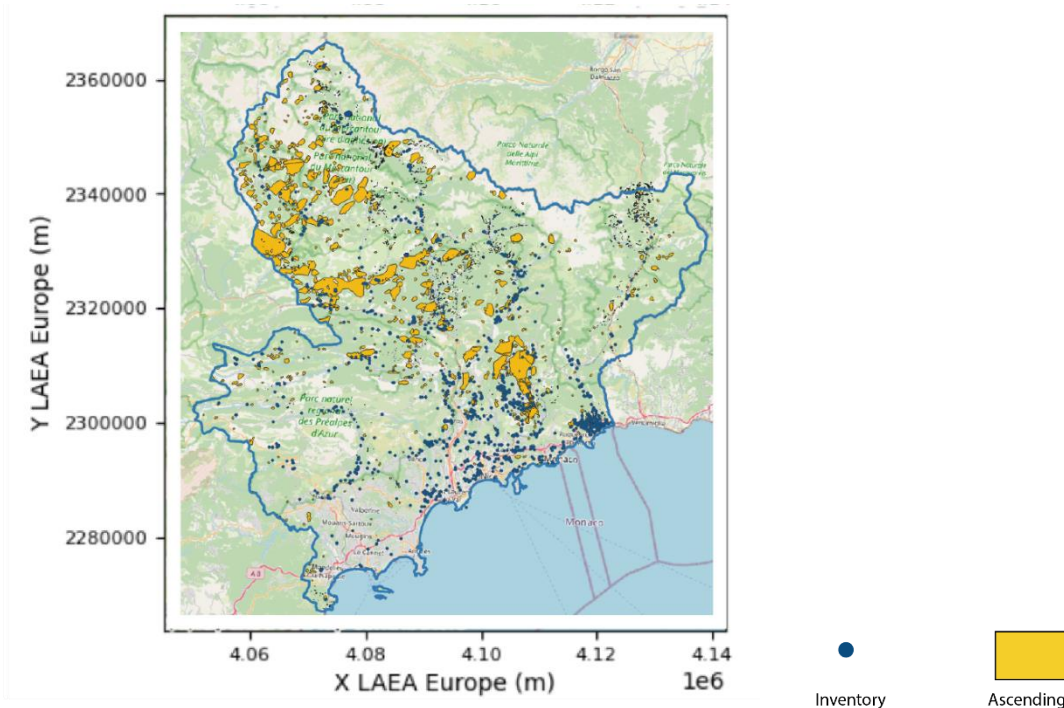


Figure 4.6: EGMS Calibrated/L2b ADAs in descending orbit compared with updated national inventory (blue dots) on the French Alpes Maritimes department.

The current EGMS update shows a higher number of ADAs compared to the 2018-2022 update, probably related to the increase in point density (see also section 2.1.2).

The Calibrated/L2b product has been chosen for this comparison given that the regional component of the motion can be neglected (less than 0.7 mm/year). In the ascending orbit, 55% of the detected ADAs intersect at least one inventory polygon, while, among the overall inventory data, only 40% of the polygons match with an ADA. In the descending orbit, those percentage goes to 59% and 26%, respectively.

These results indicate EGMS's capability to detect slow-moving landslides that may not be visible on the ground, particularly in remote areas. National inventories primarily depend on in-situ observations and damage reports that typically focus on built-up environments and related assets.

*More than half of the (potential) landslides identified by EGMS are not recorded in the up-to-date national landslide inventory. Particularly slow-moving landslides. This presents interesting perspectives for improving national inventories. These findings align with those of the [previous EGMS release validation](#). EGMS proves its value as a complementary tool to field observations and has the potential to enrich national inventories.*

#### 4.1.2.2 Rules reservoir (Spain)

The 30 km<sup>2</sup> basin around the Rules reservoir is affected by several landslides, most of them reported in the Spanish national inventory.

The Spanish inventory is built through both field mapping and an ad-hoc InSAR processing conducted by CSIC/IGME. To be consistent with [2018-2022 analysis](#), a velocity threshold of 4 mm/year in the ADA procedure has been used to detect relevant moving areas.

While EGMS measures local and regional motion, field-based inventories record local, relative, landslides velocities. A comparison between EGMS derived ADAs and field-based inventories reveals that the test area is influenced by regional motion related to neotectonic activity; with

a measured magnitude consistent with previously reported values (Piña-Valdés et al. 2022). Due to the presence of this widespread regional motion, the Basic/L2a product was deemed more suitable for the current analysis than the Calibrated/L2b product. Unlike Calibrated/L2b, the Basic/L2a product is not calibrated using GNSS data, allowing for the assessment of local-scale motion. It is also important to note that the study area is located in the southern sector of Sierra Nevada, characterized by very large gravitational motions.

Figure 4.7 presents a comparison between the EGMS ADA results and the landslide inventory for both ascending and descending orbits. The differences observed between ascending and descending ADAs are primarily related to the varying orientation of landslide slopes relative to the satellite acquisition geometry. As already noticed for the Alpes Maritimes Department (section 4.1.2.1), the number of detected EGMS ADAs in this analysis is higher than in the [2018-2022 update](#) (e.g. 108 compared to 27 within the validation zone for the descending orbit).

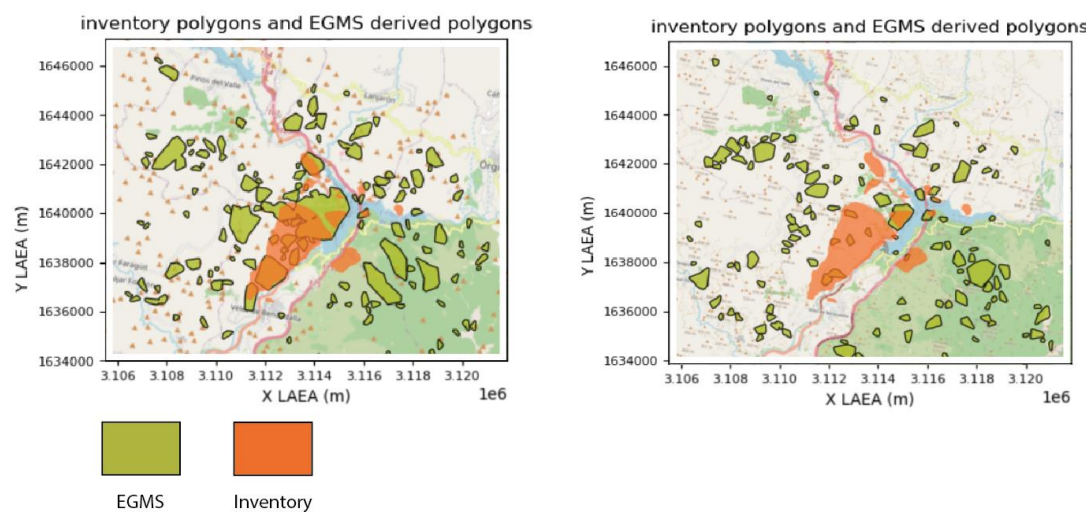


Figure 4.7: Basic/L2a ascending and descending Active Deformation Areas (green) and inventory polygons (orange).

Overall, a low level of similarity is observed between the EGMS ADA results and the inventories. Only 23% of the EGMS Basic/L2a derived polygons from ascending orbits, and 10% from descending orbits, are consistent with the inventory. This discrepancy may, in part, be attributed to changes in landslide activity that have occurred since the inventory was originally compiled. To help explain this discrepancy, velocity differences both within the landslide polygons and within a 300-meter buffer were analysed. Only a minority of the landslide ADAs exhibit deformation velocity differences exceeding the 2mm/year difference threshold, indicating that most are slow moving landslides.

---

*In the Rules area, inventory polygons only partially align with the EGMS ADAs, likely because landslide activity may have changed since the inventory was created, and the initial inventory (initiated in 1997) was not fully exhaustive. Despite this, EGMS data successfully detects new potential landslide polygons. A more detailed analysis would be required to distinguish landslides from other types of movements within these polygons.*

---

#### 4.1.2.3 Arcos de la Frontera (Spain)

The EGMS Basic/L2a product is evaluated, for the ascending and descending orbits, in Figure 4.8. In this area, the landslide LOS motion is ten times faster than the regional motion (Bru et al., 2017).

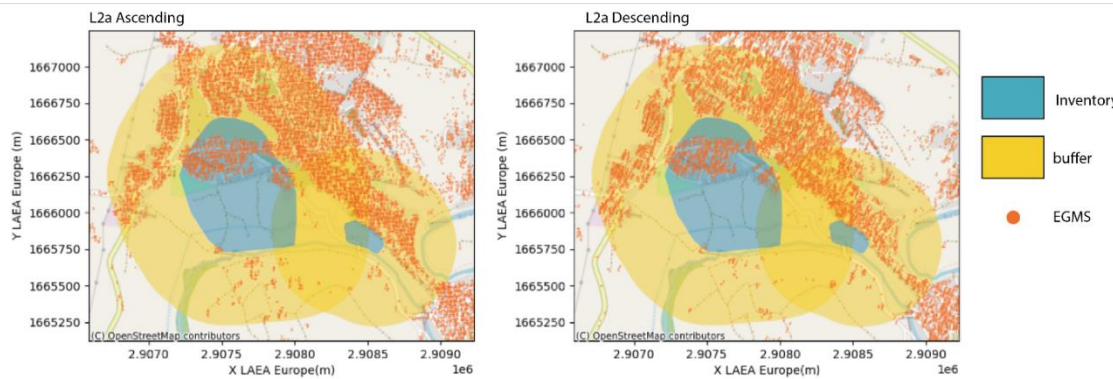


Figure 4.8: Inventory polygons with 300m buffer and EGMS Calibrated/L2b MPs coverage for ascending (left) and descending (right) orbits (EGMS data 2019-2023).

The Arcos de la Frontera landslide is partially covered by vegetation, resulting in changes to the land cover that affect the MP density. MPs are predominantly found in built-up areas however, the large-scale landslide located at the centre of the region, indicated in blue, has been accurately detected by EGMS in both orbits.

The central landslide polygon is further represented in Figure 4.9. The ADAs derived from EGMS measurements are shown in orange on this same figure.

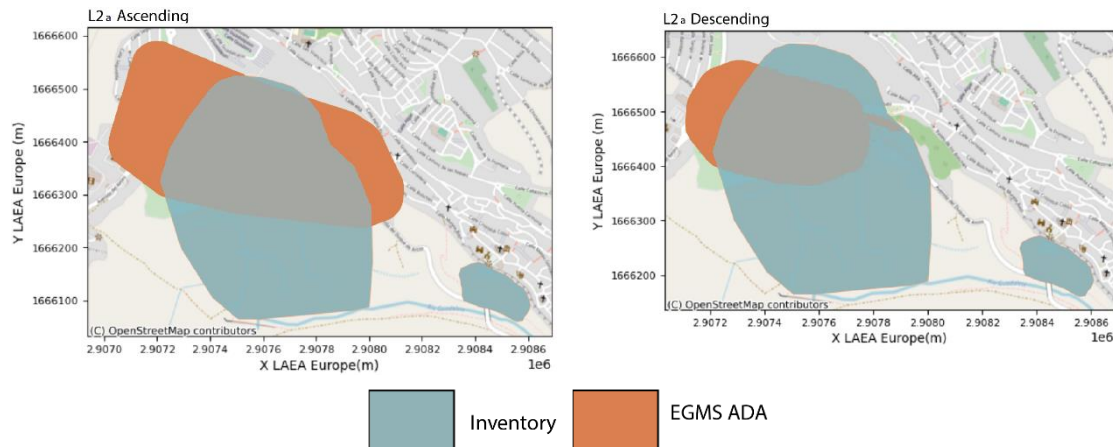


Figure 4.9: Inventory polygon compared with the ADAs generated from EGMS MPs

The intersection between the two polygons is further investigated with methodology described in Table 2.7. In the ascending orbit, the overlap area between inventory polygons and EGMS derived ADAs, in % of the total polygons area, is 55%.

In descending orbit, the overlap area between inventory polygons and EGMS derived ADAs, in % of the total polygons area, is 47%. This is a positive result given that the shape of the inventoried phenomena highly depends on land cover. Similar performances were obtained for the [2018-2022 release](#).

Table 4.3 summarises the achievements of the velocity analysis. EGMS Basic/L2a product effectively captures velocity differences between inventory polygons and their stable surroundings. The average EGMS velocity is slightly lower than the [previous release](#), likely due to the landslide's deceleration or a shift in movement direction. Another possible factor to consider could be changes in rainfall rates.

Note that EGMS MP density has increased, in the study areas, with respect to the [previous release](#) (see section 2.1.2).

Table 4.3: Summary of findings for Arcos de la Frontera landslides.

EGMS product	Velocity difference between inventory polygon and its surrounding buffer	Average velocity in the surrounding buffer (stable)	Number of EGMS measurement points inside the inventory polygon
Basic/L2a/ASC	3.3 mm/year	0.1 mm/year	1124
Basic/L2a/DESC	1.7 mm/year	0.4 mm/year	1054

*The detection is considered successful because the average difference in EGMS values between the inside/outside the inventory polygons is close to 2 mm/year, considering that landslide motion behaviour might have changed between the two EGMS releases. EGMS complements field observations to update inventories.*

## 4.2 Mining and post-mining

### 4.2.1 Comparison with inventories of phenomena

#### 4.2.1.1 French inventory (Lorraine region)

ADA-derived polygons were created using a velocity threshold of 2 mm/year, which is suitable considering the ground motion phenomenon encompasses a gradual uplift over more than 10 km. With no significant regional motion detected, the Calibrated/L2b EGMS product is used for analysis.

Figure 4.10 presents a comparative analysis between the local inventory, which consists of polygons derived from in-situ levelling measurements, and EGMS-derived ADA polygons obtained from the Calibrated/L2b product and Ortho/L3\_UD. The datasets show a high consistency with approximately 60% overlap for the L2b product and 70% for Ortho/L3\_UD vertical product.

The agreement with Ortho/L3\_UD ADAs is better likely because levelling also measures the vertical component of the motion. The product has moreover been resampled, which may reduce the impact of small velocity variations. Horizontal movements, especially at the edge of subsidence, may also more affect Calibrated/L2b measurements and accuracy.

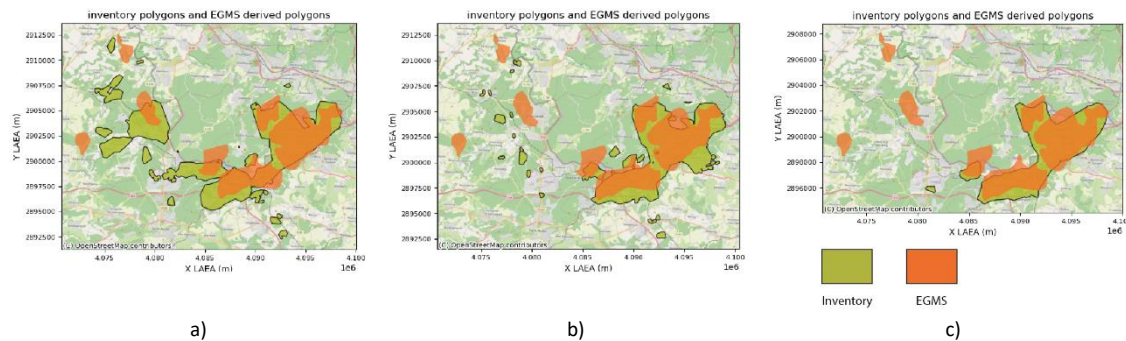


Figure 4.10: Inventory versus EGMS Calibrated/L2b (a) descending, b) ascending and c) Ortho/L3\_UD.

Table 4.4 provides a summary of the metrics resulting from the intersection between inventories and EGMS-derived ADAs. ADAs derived from EGMS are highly consistent with the vertical movements observed in the inventory for both ascending and descending orbits.

Table 4.4: Validation metrics for the Lorraine region.

	Overlap area between inventory polygons and EGMS derived ADAs. In % of the polygons area.	Difference area between inventory polygons and EGMS derived ADAs. In % of the polygons area.
Calibrated/L2b/ASC	63%	42%
Calibrated/L2b/DESC	56%	60%
Ortho/L3/Vertical	70%	22%

*Up to 70% of the EGMS-identified moving areas are consistent with the existing inventory, demonstrating the reliability of EGMS in detecting zones affected by post-mining ground motion. This includes areas where the inventory is incomplete or lacks detailed coverage. EGMS products—particularly the L3 product—provide valuable data for monitoring groundwater-related post-mining uplift phenomena, which typically occur on a kilometre scale with deformation rates of a few millimetres per year. These findings highlight the benefits of a cross-border monitoring service, capable of delivering comprehensive and consistent observations across national boundaries.*

## 4.2.2 Comparison with geo-information

### 4.2.2.1 La Unión (Spain)

The EGMS data over La Unión were compared to ancillary geoinformation to assess their usability in this complex mining terrain. Using the same ADA detection parameters as in the [previous validation update](#), ADA detection resulted in similar numbers of smaller ADAs. Figure 4.11 and Figure 4.12 show the EGMS velocity maps with detected ADAs for La Unión, based on Basic/L2a data from both ascending (track 103) and descending (tracks 8 and 110) orbits.

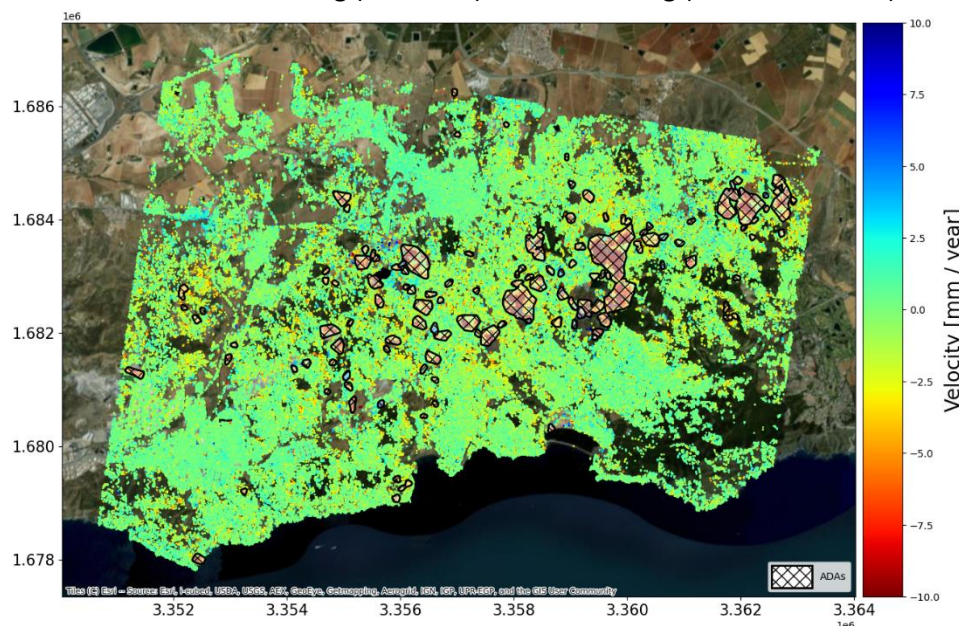


Figure 4.11: EGMS Basic/L2a velocity maps for ascending track 103 for La Unión, with detected ADAs marked as black polygons.

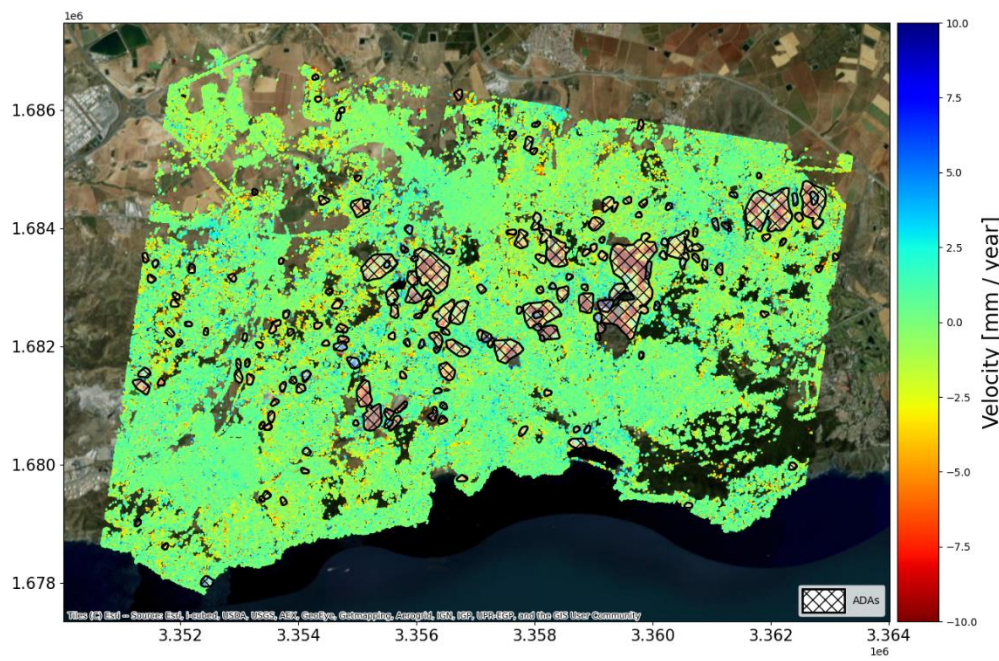


Figure 4.12: EGMS Basic/L2a velocity maps obtained by combining descending tracks 8 and 110 for La Unión, with detected ADAs marked as black polygons.

The location and characteristics of the detected ADAs were compared with external geoinformation, including Corine Land Cover (CLC) map and a mine waste inventory.

### Comparison with Corine Land Cover Map

The comparison with CLC aims to assess the consistency of land cover related factors causing ground displacement. Figure 4.13 and Figure 4.14 show the detected ADAs overlaid on the CLC categories for both ascending and descending orbits. Both images clearly show a significant overlap with the mineral extraction class.

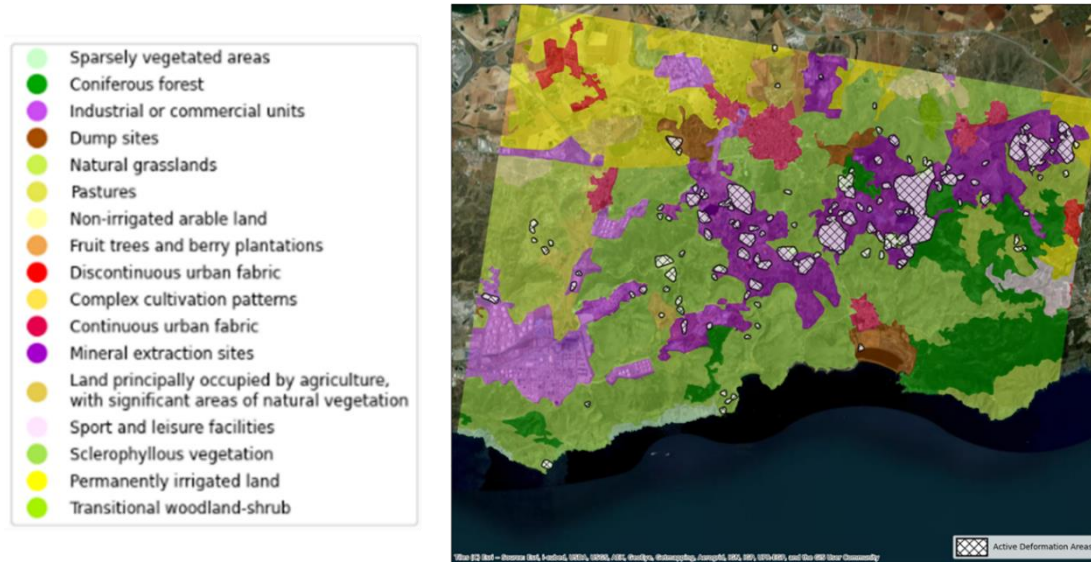


Figure 4.13: ADAs superimposed on the Corine Land Cover (CLC) map for Basic/L2a products in ascending orbit.

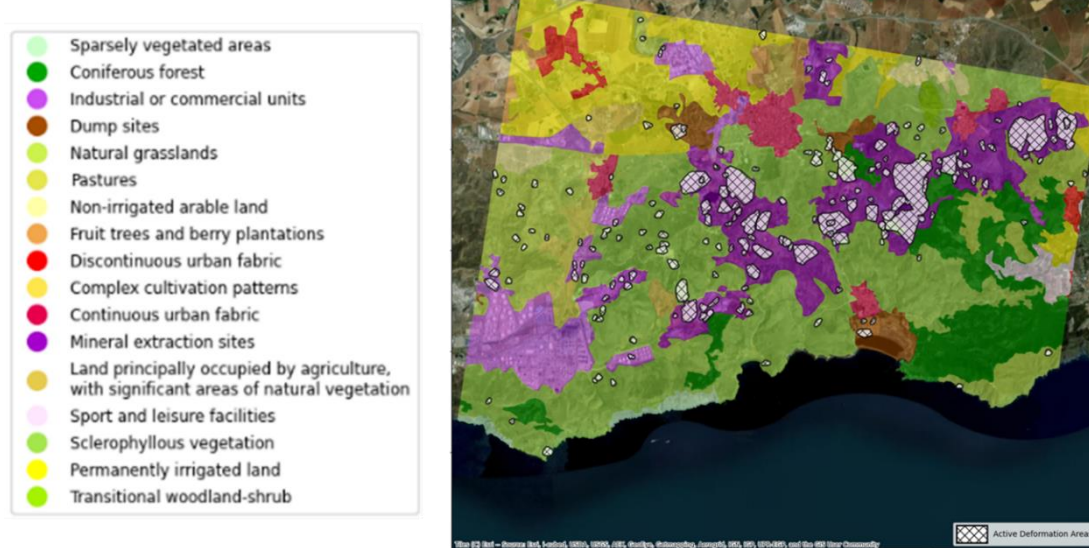


Figure 4.14: ADAs superimposed on the Corine Land Cover (CLC) map for Basic/L2a products in descending orbit.

In addition, the diagram in Figure 4.15 shows the areal coverage of ADAs (percentage) with respect to CLC classes. Different colour bars represent different EGMS product levels. As previously observed, the results confirm a strong correlation between the presence of ADAs and the “Mineral Extraction site” CLC class, consistent with the findings shown in Figure 4.14. Most ADAs not overlapping with mineral extraction sites overlap with “Sclerophyllous vegetation”. This can be attributed to the fact that this is the dominant CLC category in the area, surrounding most mineral extraction sites.

Overall, the EGMS products show strong consistency with the Corine Land Cover map, as the detected ADAs predominantly overlap with areas classified as mineral extraction sites.

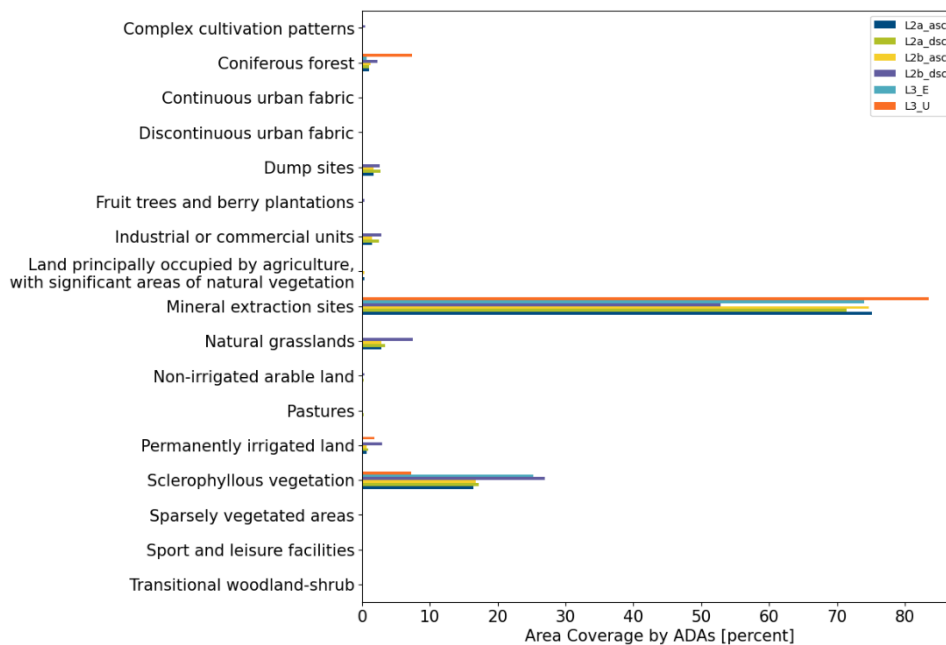


Figure 4.15: Measured overlap of ADAs derived from Basic/L2a data with Corine Land Cover (CLC) categories in La Union.

## Comparison with a mine waste inventory

The EGMS products were also compared with an inventory of “Mine waste” and “Tailings”, where mine waste covers various types of predominantly solid waste materials, and tailings are usually deposited as slurry, mixed with substantial amounts of water. Figure 4.16 shows the

overlap of ADAs detected for Basic/L2a ascending (a) and descending (b) datasets. In addition, Figure 4.17 provides an overview of the measured areal coverage of both mine waste and tailings by ADAs (expressed in percentage) for all EGMS products.

Figure 4.16 and Figure 4.17 show that most ADAs overlap with mine waste areas. The expected overlap with tailing areas, which typically exhibit significant subsidence due to the compaction, is not observed (Figure 4.17). Given that mining activities in this area ceased approximately two decades before the start of the EGMS dataset, it is likely that the tailings have consolidated over time, resulting in no significant motion.

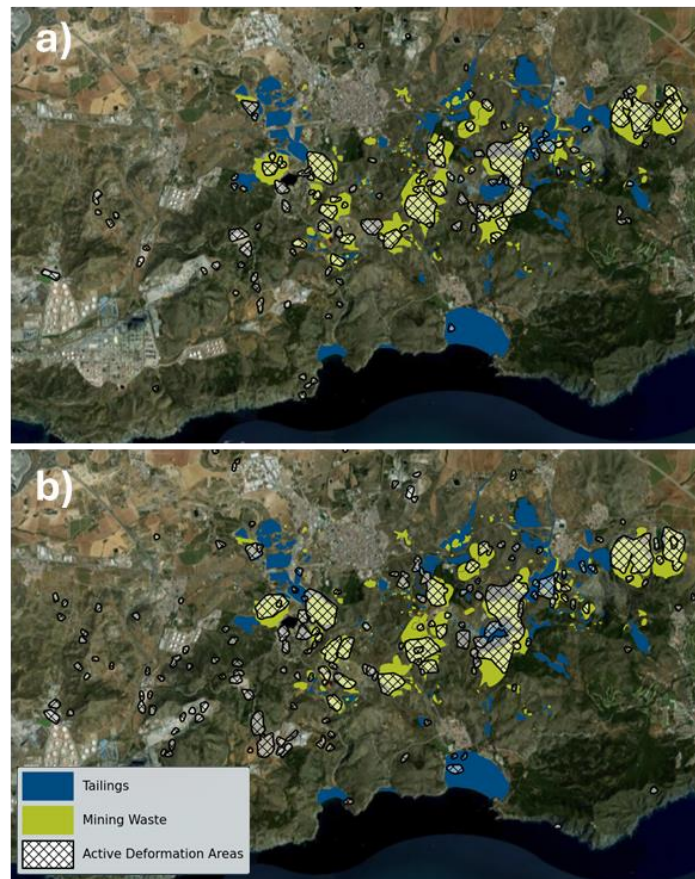


Figure 4.16: Basic/L2a Ascending (a) and Descending (b) EGMS ADAs versus mine waste land cover classes.

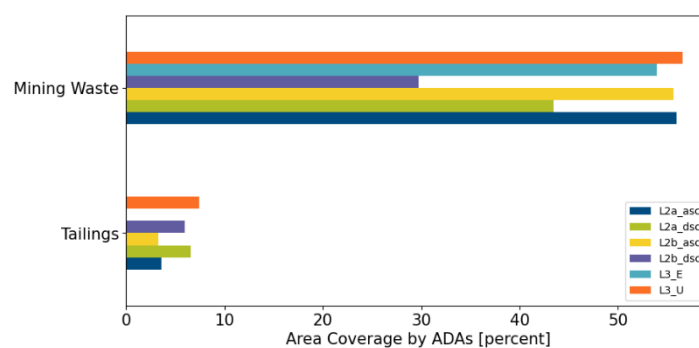


Figure 4.17: Measured overlap of ADAs with mine waste and tailings storage facilities.

Three additional datasets have been compared to EGMS: lithology, fault lines and topography. Since the motion in this region is mainly associated with post-mining phenomena, no significant correlation was found.

*EGMS-derived ground motion is consistent with CLC class “mineral extraction sites”. There is a significant overlap between the EGMS-derived ADAs and the location of mine waste sites, whereas this is not true for tailings. This suggests that EGMS can help differentiate the state of activity of tailings. This demonstrates the capability of the EGMS to map active motion (if any) in this kind of post-mining area.*

#### 4.2.2.2 Silesia (Czech Republic)

The validation site in Silesia, a region shared between Czech Republic and Poland, is one of the largest hard coal mining areas in Europe, with mining activity starting in the 19th century. Figure 4.18 and Figure 4.19 present the Basic/L2a velocity maps for ascending and descending, respectively, where all available orbits have been combined into a single dataset. Ascending tracks 73, 102, 175 are shown in Figure 4.18 while descending tracks 51, 124 are shown in Figure 4.19.

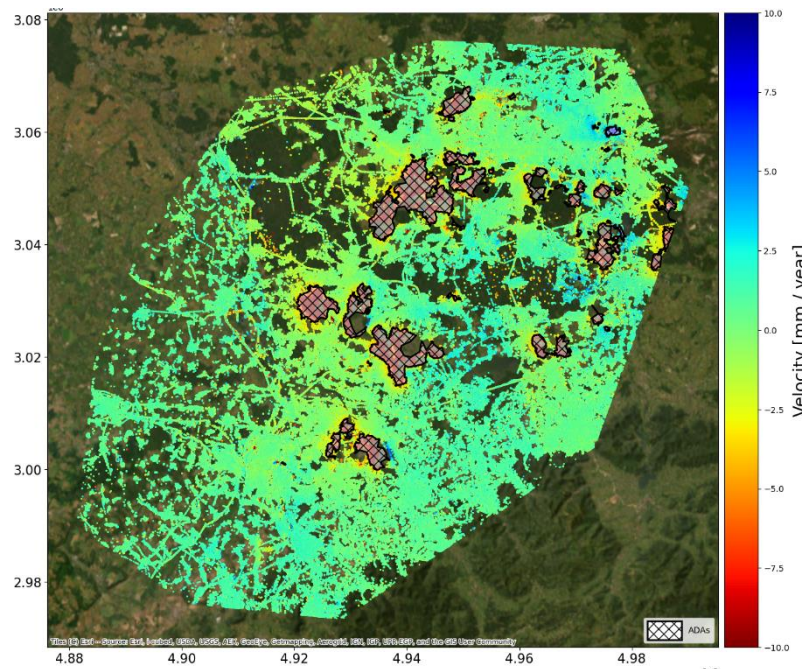


Figure 4.18: EGMS Basic/L2a velocity maps for the ascending tracks 73, 102, and 175 for the Silesia area with detected ADA polygons.

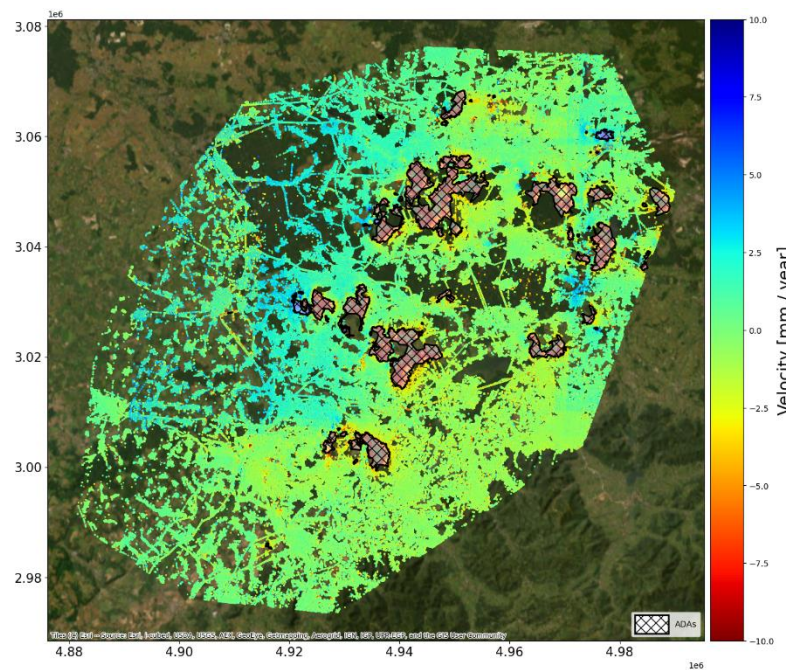


Figure 4.19: EGMS Basic/L2a velocity maps for the descending tracks 51 and 124 for the Silesia area with detected ADA polygons.

The location and characteristics of the detected ADAs were compared with external geo-information.

#### Comparison with an inventory of mining-related areas:

An inventory of mining-related areas in the Czech Republic was used to compare with the EGMS detected ADAs. No comparison was performed for ADAs located in Poland. Figure 4.20 illustrates the overlap between the ADAs detected in the Basic/L2a datasets — for ascending tracks 73, 102 and 175, and descending tracks 51 and 124, and the mapped mining areas.

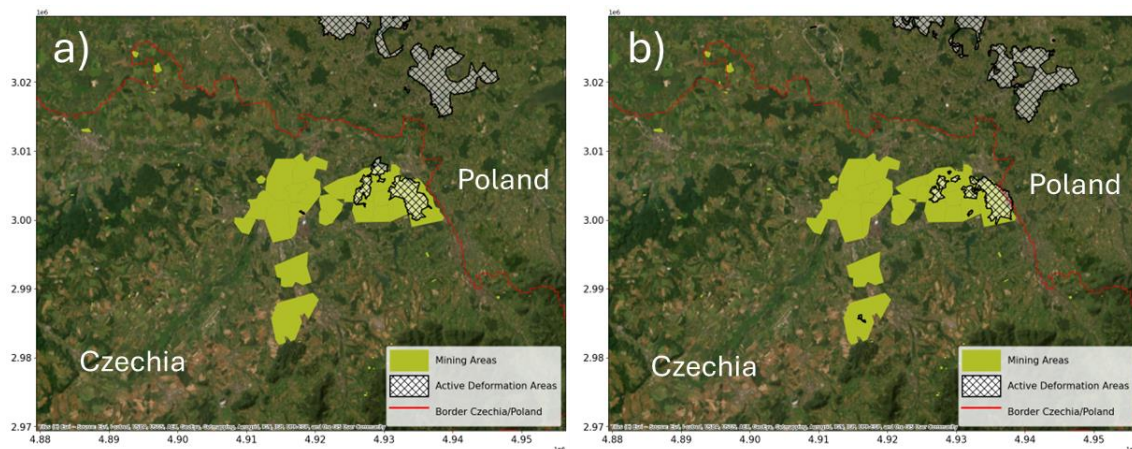


Figure 4.20: Locations of mining-related areas (light green) plotted together with Basic/L2a ADA locations for a) ascending tracks 73, 102, and 175, and b) descending tracks 51 and 124 (hatched polygons).

Both ascending and descending results show a good overlap. On the eastern portion of the area of interest, the boundaries of the ADA and the mining area show a very good overlap. The small ADA located further to the south correlates with a mining area only in descending orbit (Figure 4.20 b)).

The absence of ADAs in the other reported mining areas may be due to different mining activities or past activities that no longer cause ground motion. Detailed information regarding the status



or nature of mining activities is unfortunately unavailable. A comparison with the MP distribution shown in Figure 4.18 and Figure 4.19 suggests that the lack of ADAs in these areas cannot be attributed to a low MP coverage.

Four additional datasets have been compared to EGMS: Corine Land Cover, fault lines (Czechia only), a geologic map (Czechia only) and topography. Since the motion in this region is mainly associated with subsurface mining activity, no significant correlations were found, including for Corine Land Cover and the presence of fault lines, which are almost exclusively outside the mining affected areas.

---

*The comparison between EGMS and the mapped mining areas shows a good agreement, and there are no unexpected correlations with any other ancillary dataset (e.g. land cover).*

*This shows, that the EGMS is capable of mapping ground motion related to subsurface mining, within the technical boundaries of the product.*

---

## 4.3 Urban

### 4.3.1 Comparison with other GMS

#### 4.3.1.1 Thyborøn (Denmark)

For validation in Thyborøn, uncalibrated LOS data produced by the Technical University of Denmark (DTU) were used. The study focussed on the harbour, which is dominated by a single ADA.

Figure 4.21 and Figure 4.23 show the comparison of the datasets for ascending track 15 and descending track 37, respectively. Both motion measurements were resampled to match the same spatial grid and time period, but they were not re-referenced to a common reference point.

An initial analysis indicates that the EGMS data shows a higher MP density than the DTU dataset, primarily due to differences in the processing strategies applied. The figures also show a slight velocity offset of about 1 mm/year between the two datasets for both orbits, which is especially visible in the difference maps shown in Figure 4.21 c) and Figure 4.23 c). This offset may be related to the different reference point selections. Despite this discrepancy, there is an equal general delineation of the ground motion area in the two datasets. Some differences, particularly in the southern part of the town, are likely due to variations in point density rather than velocity values.

The comparison of the averaged ADA time series (Figure 4.22 a) and Figure 4.24 a)) also shows a good agreement between the two datasets. Both show almost linear trends, with minor deviations due to the observed velocity offset. The DTU time series exhibit a noisier behaviour, most likely linked to the use of different processing methods.

The velocity correlation plot in Figure 4.22 b) and Figure 4.24 b) exhibits roughly linear patterns, in both cases with only a slight shift from the diagonal. This is also consistent with the general slight offset between the velocity values observed above.

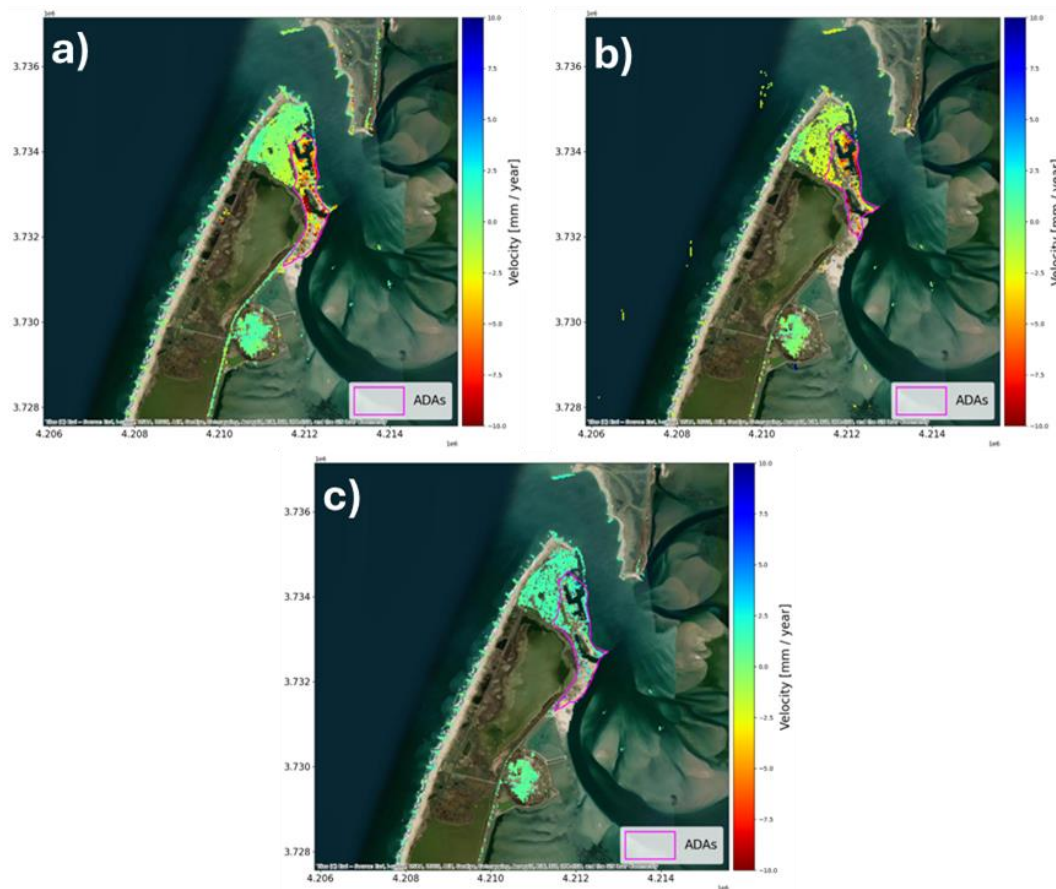


Figure 4.21: Comparison of Basic/L2a velocities from ascending track 15 for (a) the EGMS and (b) DTU-derived InSAR map; (c) velocity difference ( $dvel = \text{vel EGMS} - \text{vel DTU}$ ). ADAs are marked by magenta polygons.

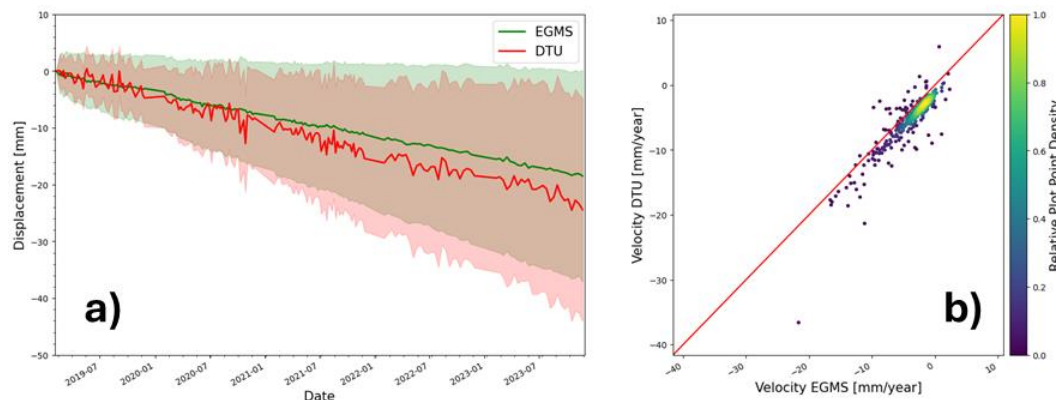


Figure 4.22: (a) Comparison of mean and standard deviation for the time series in the ADA indicated in Figure 4.21 for ascending track 15; (b) velocity correlation for the same ADA.

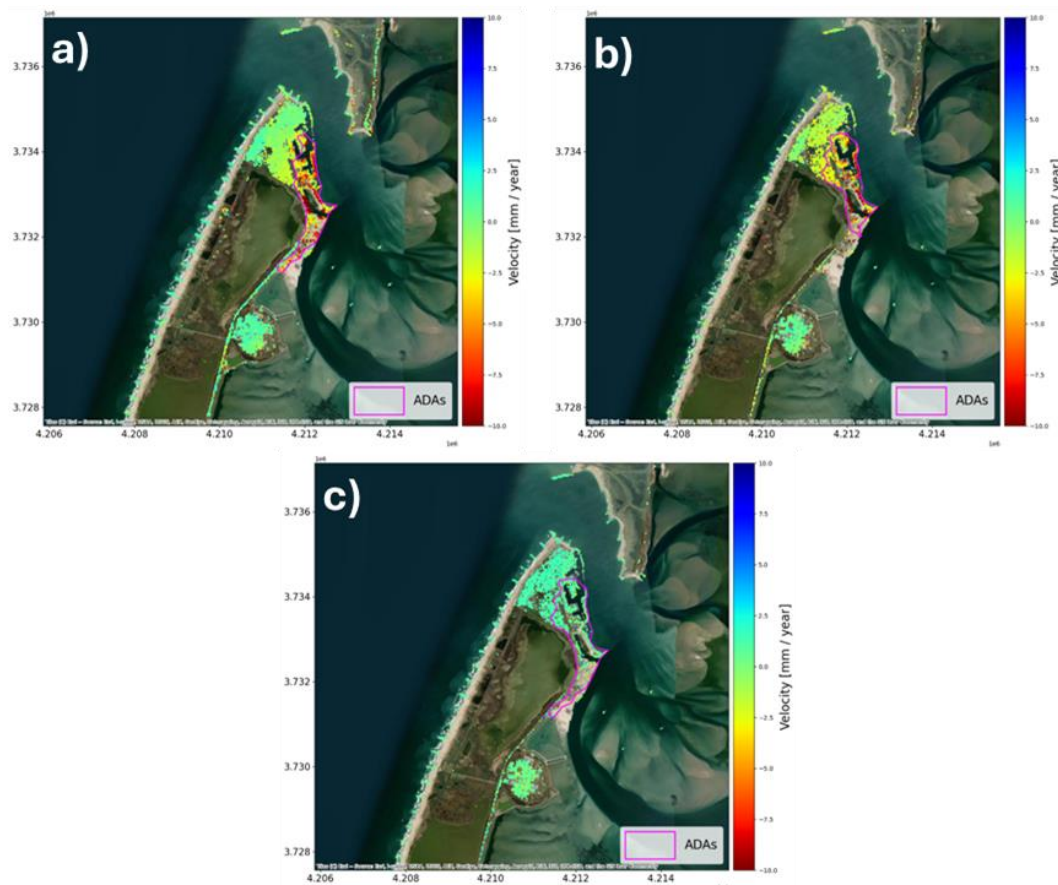


Figure 4.23: Comparison of Basic/L2a velocities from descending track 37 for (a) the EGMS and (b) DTU-derived InSAR map; (c) velocity difference ( $dvel = \text{vel EGMS} - \text{vel DTU}$ ). ADAs are marked by magenta polygons.

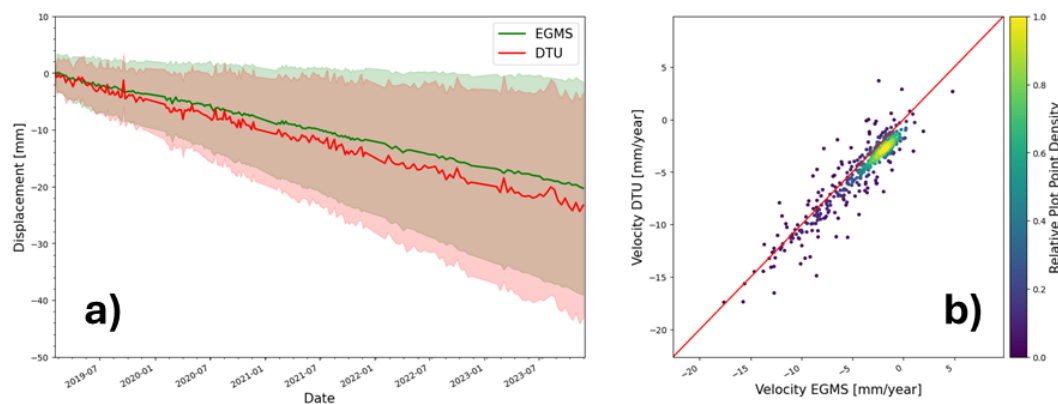


Figure 4.24: (a) Comparison of mean and standard deviation for the time series in the ADA indicated in Figure 4.23 for descending track 37; (b) velocity correlation for the same ADA.

Table 4.5 summarises the validation metrics (described in Table 2.6 and [D6-Validation Methodologies](#)) for the Thyborøn town. The ~1mm/year velocity offset does not affect the location and shape of the detected ADAs in the harbour area of the town. Thus, the spatial overlap is very good and significantly higher than in the [2018-2022 report](#), where a larger area around the town was considered. This confirms that the misfits for smaller ADAs outside of the town were mainly impacting the performance of the validation exercise.



Table 4.5: Validation metrics for Thyborøn, Denmark.

Description	Value
Spatial overlap [%]	80.71
Relative Velocity Difference [%]	36.94
Velocity Correlation	0.84
Displacement Time Series Correlation	0.87

---

*The comparison for this validation site, with a focus on the Thyborøn town area, shows very good agreement. Only slight velocity offsets were observed, which do not appear to affect the ability to map the displacements in the harbour area for either dataset. It can therefore be concluded that EGMS effectively identifies subsidence phenomena at the local scale, aligning with its intended fields of application.*

---

#### 4.3.1.2 Po delta (Italy)

The Po River delta, covering an approximate area of 400 km<sup>2</sup>, is a complex ecosystem shaped by sedimentary processes and influenced by human activities such as ground water pumping. Figure 4.25 shows a comparison of displacement velocities for the Po River delta between EGMS Basic/L2a ascending track 117 and the regional GMS provided by the Regione del Veneto (RDV, Veneto Region). The comparison reveals discrepancies across a broad area in the Po River delta, with the EGMS data indicating stronger subsidence rates than the RDV data. Subsequently, considerably more ADAs have been detected in the EGMS data compared to the RDV data. This difference has already been observed in the validation of the previous EGMS updates (see Figure 41 in the validation exercise [2015-2021](#) and Figure 46 in validation exercise [2018-2022](#)).

Figure 4.26 shows the same comparison for Basic/L2a descending track 95, which confirms that the EGMS measures higher subsidence in the delta area. As discussed in the report for the [2015-2021](#) update validation, existing literature has consistently documented subsidence in the Po River Delta [Faris et al., 2014; Faris et al., 2022; Cenni et al., 2021]. Therefore, it is reasonable to conclude that, for this region, the EGMS offers a more accurate representation of large-scale deformation patterns compared to the regional GMS.

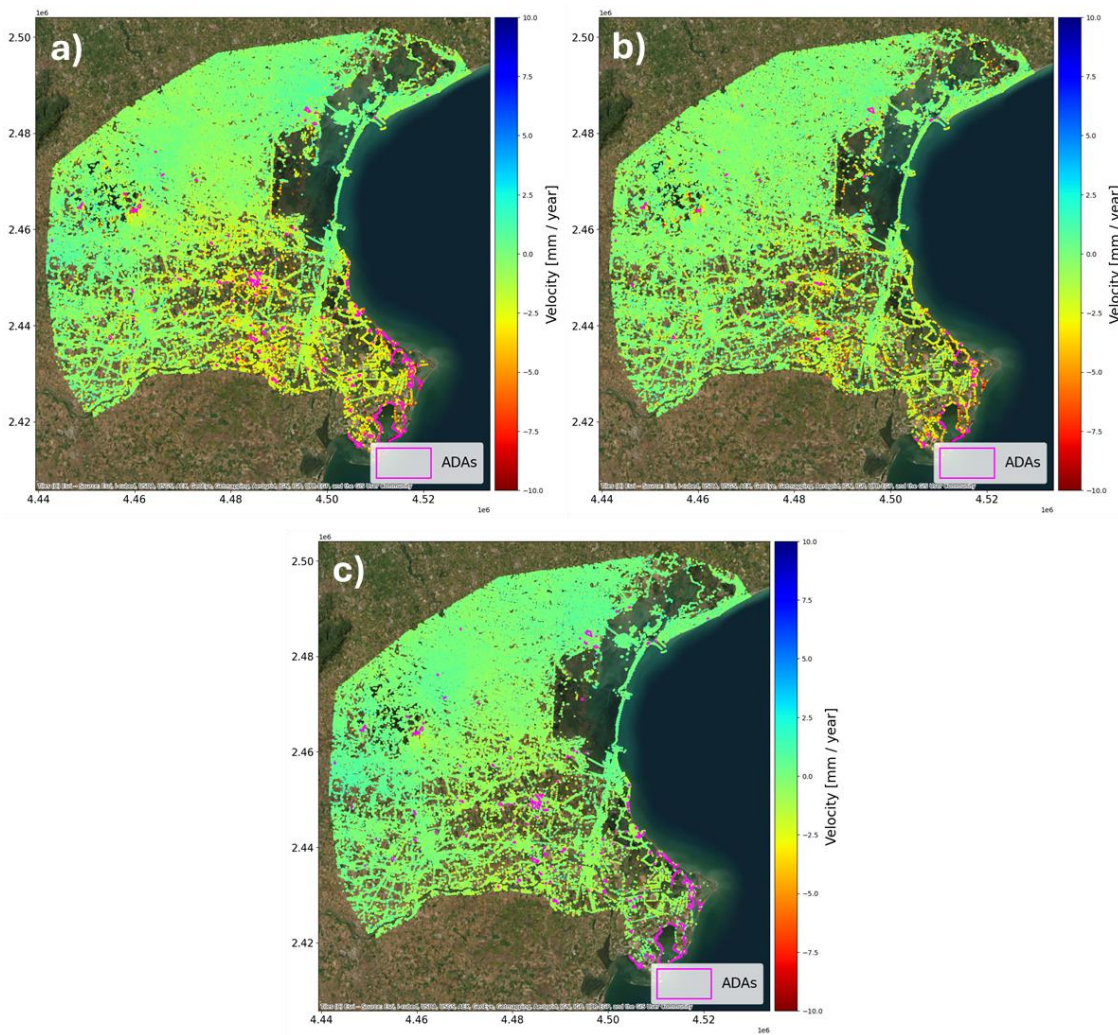


Figure 4.25: Comparison of displacement velocities for the Veneto validation site: a) EGMS Basic/L2a ascending track 117; b) Regione del Veneto GMS; c) Velocity difference between a) and b).

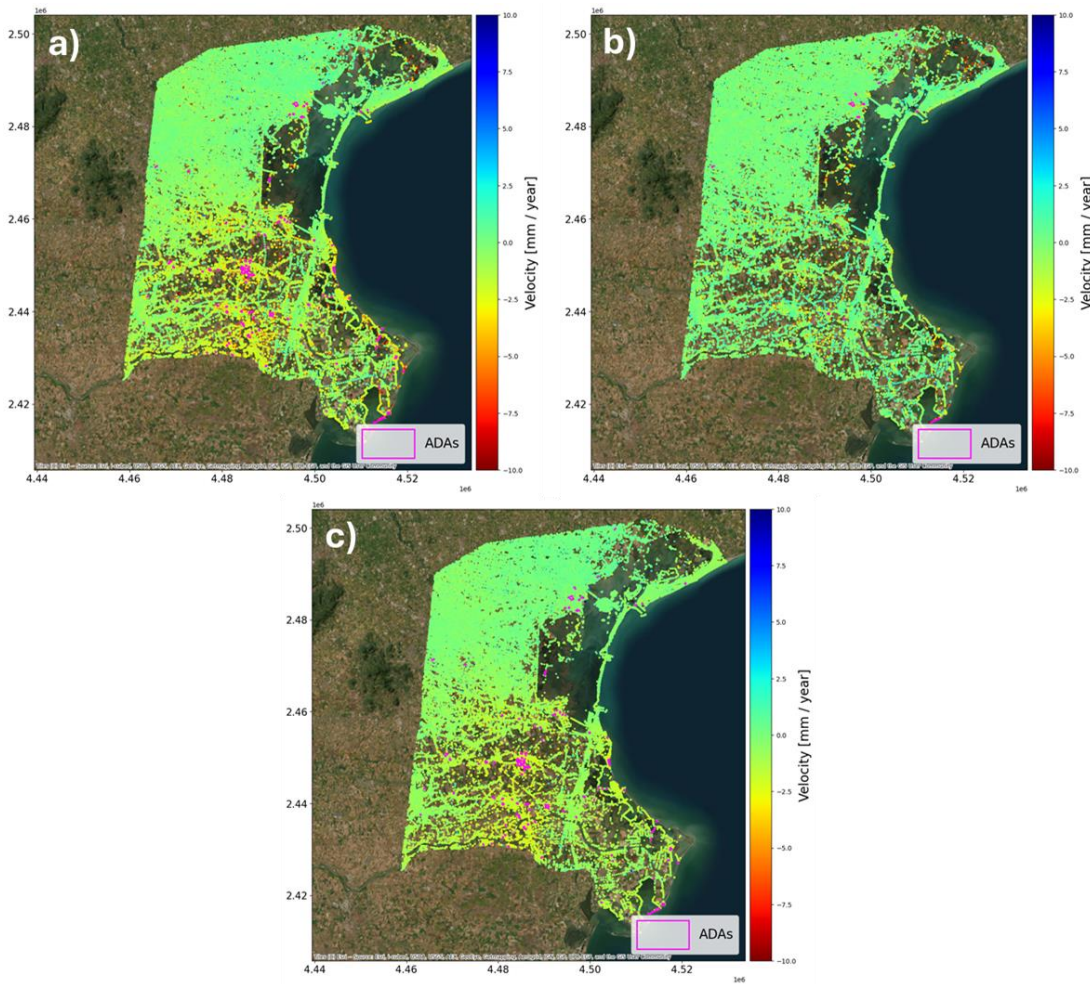


Figure 4.26: Comparison of displacement velocities for the Veneto validation site: a) EGMS Basic/L2a descending track 95; b) Regione del Veneto GMS; c) Velocity difference between a) and b).

Figure 4.27 shows a more detailed comparison over a larger ADA in the Po River Delta for ascending track 117. Despite the differences previously discussed, the velocity maps show a consistent match between the datasets, though the RDV velocities exhibit slightly more noise compared to those from EGMS.

Figure 4.28 a) shows the time series comparison, indicating a good match between the datasets, though RDV has a higher standard deviation compared to EGMS. This observation aligns with the velocity correlation depicted in Figure 4.28 b), which displays a broad non-linear distribution with several outliers in the RDV velocities.

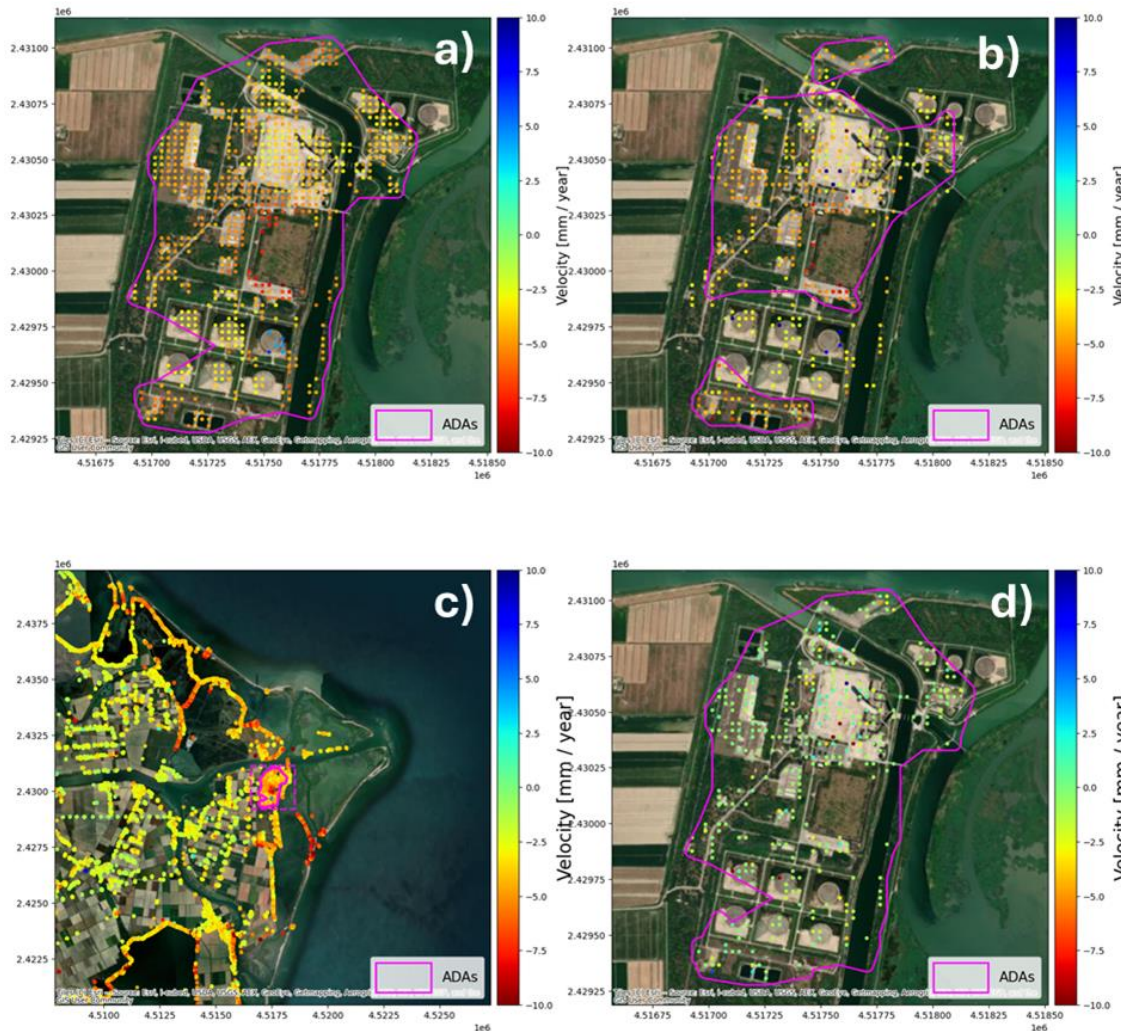


Figure 4.27: Comparison of EGMS Basic/L2a ascending track 117 for an ADA in the Po River delta: a) the EGMS and b) RDV GMS; c) location of ADA with EGMS velocities; d) velocity difference (dvel = vel EGMS – vel RDV). ADA marked by magenta polygons.

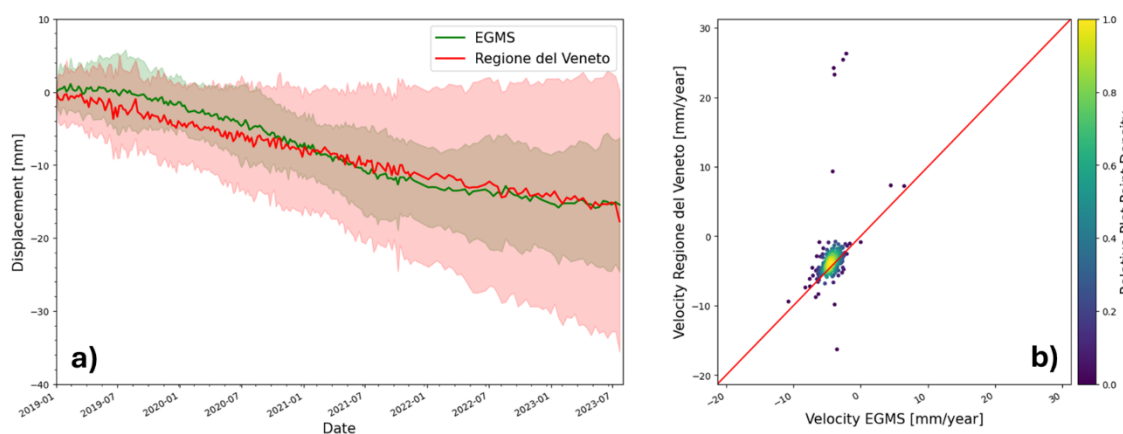


Figure 4.28: a) Comparison of mean and standard deviation for the timeseries in the ADA area indicated in Figure 4.27 d); b) velocity correlation for the same ADA.

Table 4.6 presents the validation metrics (described in Table 2.6 and [D6-Validation Methodologies](#)). As anticipated, given that most ADAs identified in the EGMS are not found in the RDV dataset, a low spatial overlap is observed. The relative velocity difference for the identified ADAs is approximately 45%. The velocity and time series correlation again indicate



relatively good agreement, which also can be attributed to the rather smooth and large-scale, but low amplitude nature of the velocity difference and the strong linearity of the time series.

Table 4.6: Validation metrics for Po River Delta

Description	Value
Spatial overlap [%]	36.02
Relative Velocity Difference [%]	45.26
Velocity Correlation	0.62
Displacement Time Series Correlation	0.79

---

*The comparison in the Veneto area reveals differences between the EGMS and RDV products. Based on literature characterising the subsidence phenomena in the Po River delta, it can be concluded that EGMS products are able to capture large-scale deformations patterns across the Po Plain, which cannot be captured by the regional dataset. This confirms the ability of the EGMS to detect both large and detailed scale ground motion patterns.*

---

### 4.3.2 Comparison with geo-information

#### 4.3.2.1 Oslo (Norway)

Figure 4.29 shows the EGMS Basic/L2a velocity maps for all available orbits in the area combined into a single dataset for both ascending (tracks 44 and 146) and descending (tracks 37, 66, and 139). ADA detection in the area results in a significantly higher number of ADAs compared to the previous validation ([2018-2022](#)), with an increase by a factor 2.0 for the ascending orbit and a factor 1.4 for the descending orbit. This increase is likely attributed to a higher level of noise in the velocity measurements. This is evidenced by the fact that the standard deviation of all velocity values, which were taken from the datasets resampled to a 15 m x 15 m grid before ADA detection, shows an increase from 1.9 to 2.9 mm/year, as illustrated by Figure 4.30 histograms.

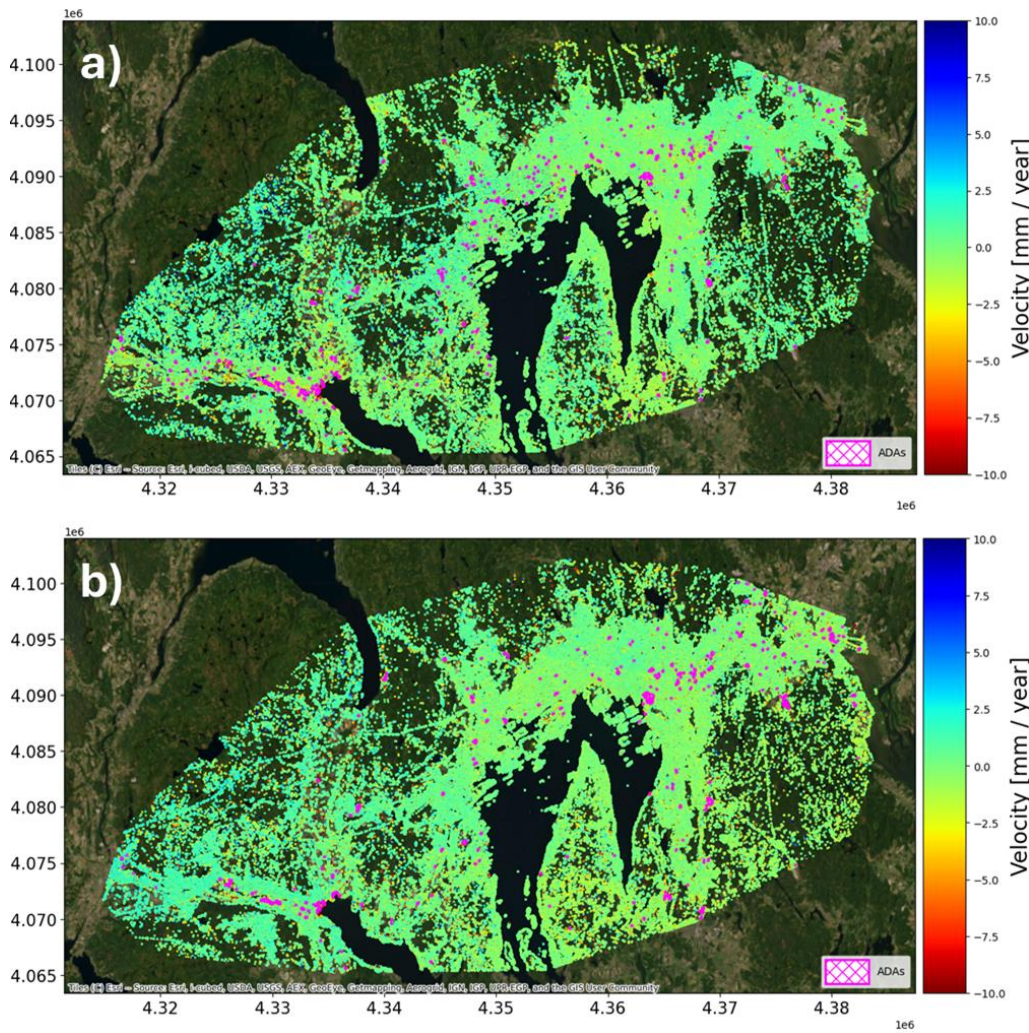


Figure 4.29: EGMS Basic/L2a velocity maps for the Oslo area with detected ADA marked as pink polygons : a) ascending tracks 44 and 146 and b) descending tracks 37, 66, and 139 (Basemap: ESRI).

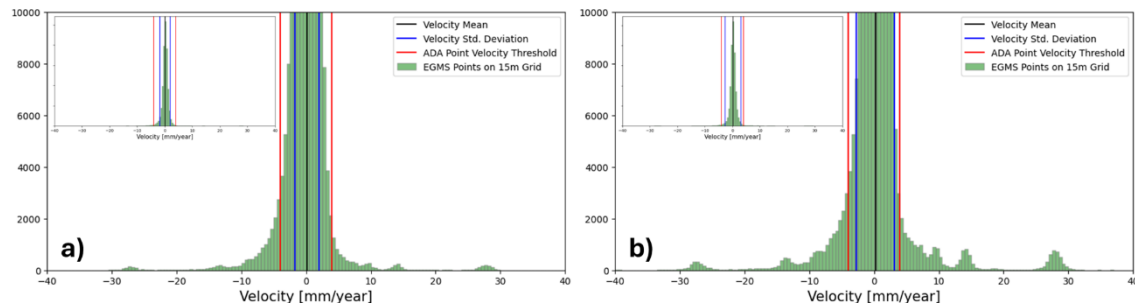


Figure 4.30: Histograms of Basic/L2a ascending velocity values computed from the 15 m x 15 m grid used for ADA detection: a) 2018-2022 EGMS update, b) 2019-2023 EGMS update.

#### Comparison with Corine Land Cover:

The comparison of displacement velocity patterns with the CLC map has been conducted to assess the consistency of ground displacement with land cover related factors contributing to ground displacement. Figure 4.31 a) shows an overview of the metropolitan area of Oslo, with detailed views of Drammen and Oslo City regions presented in Figure 4.31 (b) and (c), respectively.

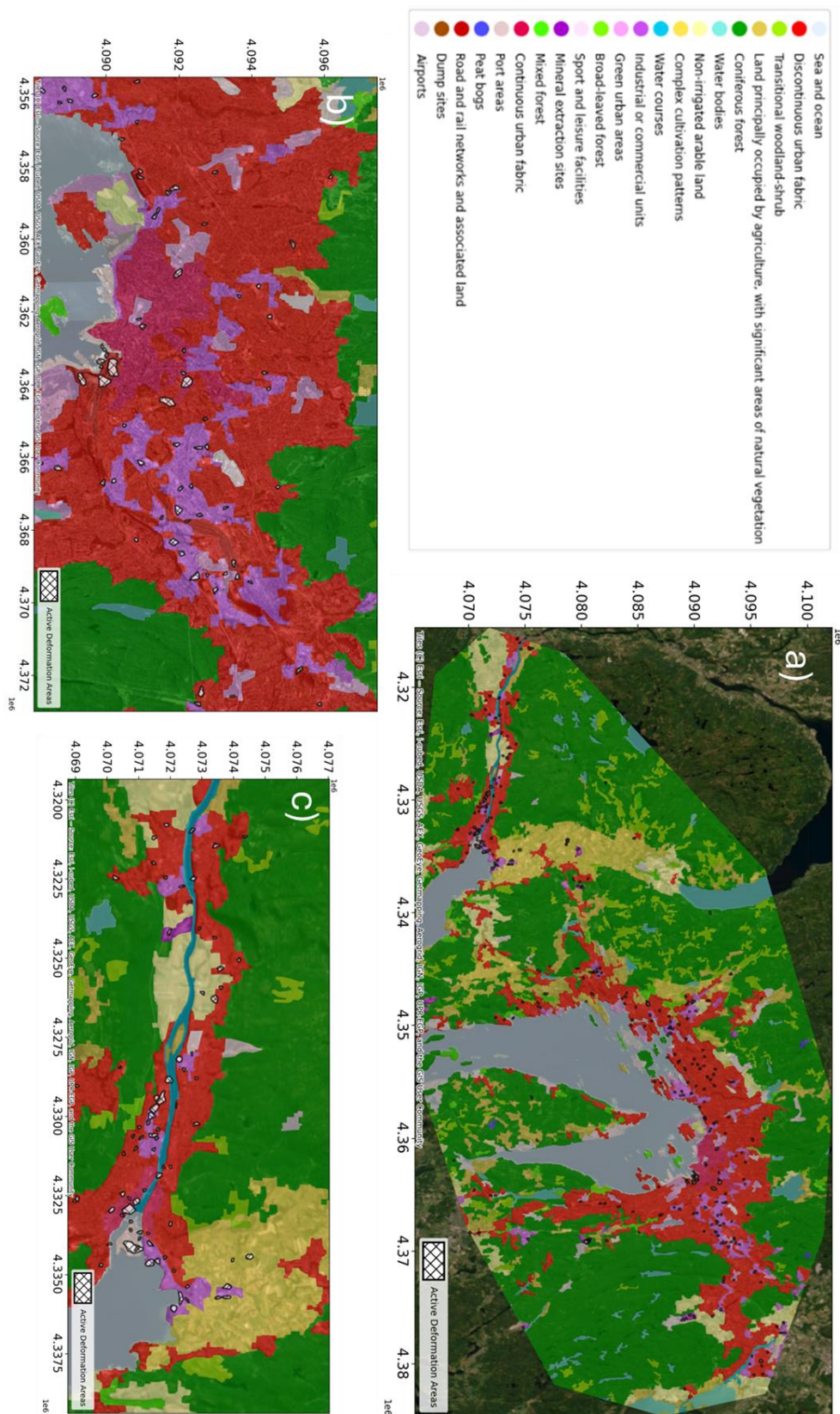


Figure 4.31: Comparison of Corine Land Cover (CLC) with Basic/L2a ascending ADAs for the Oslo municipal region. a) CLC with ADAs overlaid; b) Zoom-in of Oslo City region; c) Zoom-in of Drammen region.

Figure 4.32 provides an overview of the measured areal coverage of ADAs with respect to CLC classes (expressed as a percentage). There is a clear correlation, showing subsidence mainly

happening in areas influenced by human activities, particularly industrial and urban regions, as anticipated for this validation site.

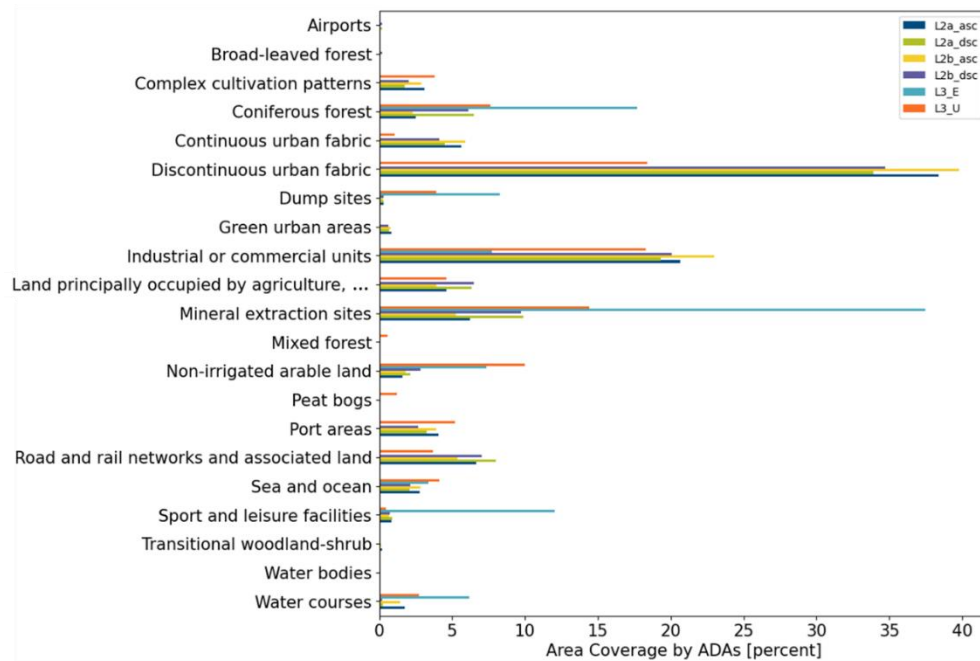


Figure 4.32: CLC area coverage with ADAs. Colour bars represent different EGMS product levels. The measured values represent the overlap of ADAs with the respective CLC category in percentage of the ADA's total area.

#### Comparison with Quaternary Geology Map:

A comparison with geological data is carried out to complete the validation of EGMS ground motion, ensuring its consistency with local geological or geomorphological characteristics. Figure 4.33 and Figure 4.34 show the comparison of a quaternary geology map with the detected ADAs. Across all products, a consistent correlation is observed between the locations of EGMS-derived ADAs and the presence of anthropogenic filling, as well as marine and fluvial deposits. These areas typically contain compressible soils with geotechnical properties that predispose them to long-term compaction, resulting in the subsidence measured by EGMS. Subsidence in the area is related to soft overburden, often in combination with construction activities that impact the pore pressure in these materials.

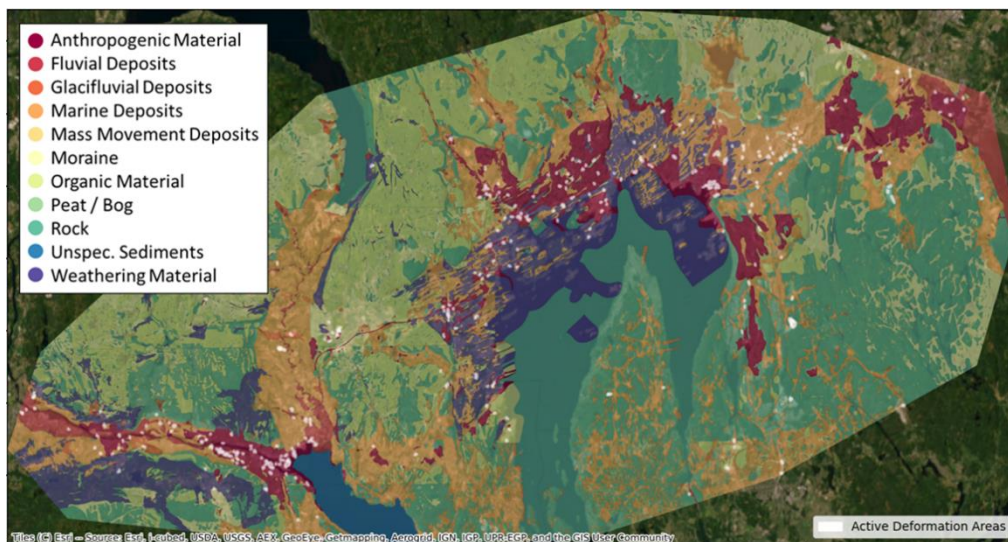


Figure 4.33: Comparison of detected ADAs with the quaternary geology for the Oslo metropolitan area.  
The map shows the ADAs from the Basic/L2a ascending orbits in white overlaid on the quaternary geology (Basemap: ESRI)

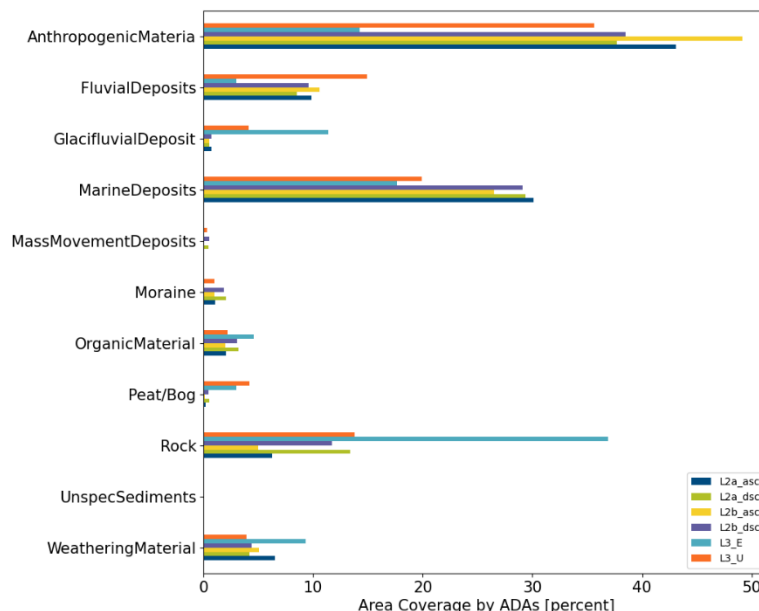


Figure 4.34: Bar plot showing the overlap between detected ADAs and various geological unit. The coloured bars represent different EGMS product levels. The values indicate the percentage of each ADA's total area that overlaps with the corresponding geological unit.

#### Comparison with Depth to Bedrock Map:

Figure 4.35 depicts the thickness of the overburden layer “depth to bedrock” for this area compared with the ADAs detected for the Basic/L2a ascending tracks 44 and 146. In areas with soft overburden layers, the thickness of these layers is expected to have an impact on the magnitude of subsidence. Assuming the same urban setting, an area with the maximum thickness of compressible soil will experience the highest subsidence rates. However, the presence of new buildings may accelerate this process. While the depth to bedrock map does not cover all identified ADAs, there is a clear correlation in several locations between the thickness of the overburden and the location and extent of the ADAs. This correlation is

particularly evident for the two larger ADAs near Oslo Central station, in the lower central part of the map, as indicated by the magenta arrow in Figure 4.35.

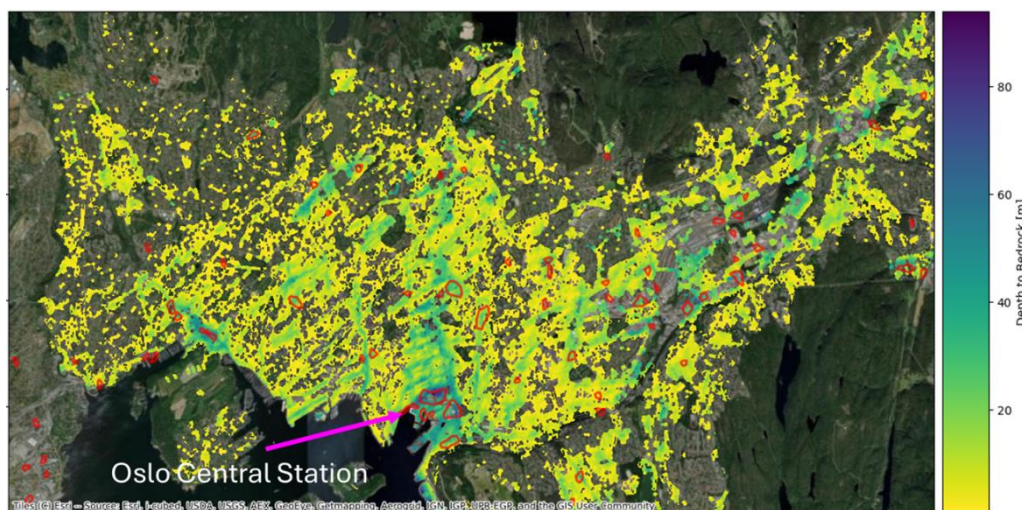


Figure 4.35: ADAs (red polygons) detected in the EGMS Basic/L2a ascending product (all tracks combined) overlaid on a map of soft soil thickness.

Two additional datasets, a bedrock map and a topographic map, have been compared to EGMS. The findings from both datasets confirm that ADAs are mostly located in areas hosting thick sedimentary sequences. The topography analysis reveals that ADAs are almost exclusively situated in flat areas.

---

*EGMS ground displacement data are highly consistent with ancillary geoinformation. The ADAs detected in EGMS mostly coincide with urban and industrial areas reported in CLC. They also overlap with thick sedimentary layers (marine and fluvial deposits) and anthropogenic materials. The comparison conducted also show a clear correlation between ADAs and increased depth to bedrock.*

*Those results demonstrate EGMS's capability to reliably map anthropogenic ground deformation phenomena within an urban environment.*

---

#### 4.3.2.2 Tagus Valley (Portugal)

Previous studies documented ground displacements associated with or correlated to the presence of fault lines. These displacements are often attributed to the influence of fault lines on local geology and their function as hydrogeological barriers (Heleno et al, 2011). However, it is important to note that the fault lines have been identified through geological interpretation, but that they are not classified as sources of seismic activity. The measured ground motion can then also result from various other factors, including human activities.

The correlation between EGMS measurements and fault lines' presence is investigated here. Observed displacements in the Tagus Valley area are generally small. Therefore, during the [2018-2022 update](#) validation activities, the point-velocity threshold for the ADA detection was set low at 1.5 mm/year, close to the expected noise level of the velocity data (see histogram in Figure 4.36 a)).

The general noise in the 2019-2023 EGMS update appears to have slightly increased compared to the [2018-2022](#) update and, as it can be seen in Figure 4.36 b), the +/-1.5 mm/year threshold falls now within one standard deviation from the mean velocity (based on resampled datasets

at a 30 m x 30 m grid before ADA detection). To account for those new statistics, the threshold for point-velocity values was raised to 2.5 mm/year and the cluster velocity increased accordingly from 2.0 mm/year to 3.0 mm/year.

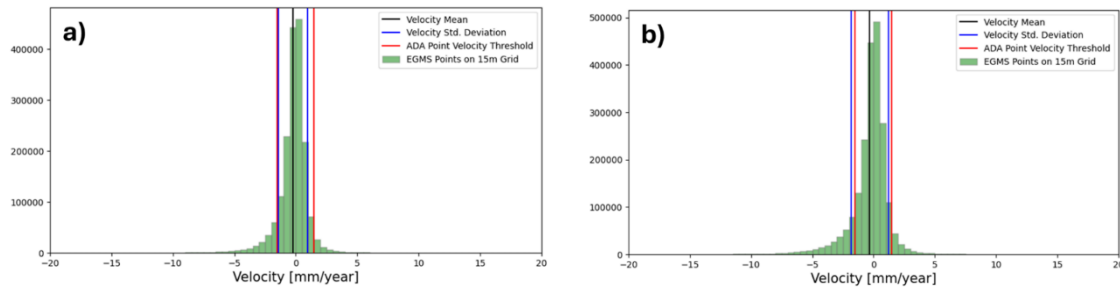


Figure 4.36: Histograms of Basic/L2a ascending velocity values computed from the 30 m x 30 m grid used for ADA detection: a) 2018-2022 EGMS update, b) 2019-2023 EGMS update.

Figure 4.37 shows velocity maps for Basic/L2a (combined for tracks 45 and 147) for the entire Tagus Valley as well as for some snapshots. The lower left and the upper left (river delta area) maps show a clear correlation between fault lines and ADA delineation. The top right map also shows good correlation between the fault lines and the ADAs, however, some of the ADAs are crossed by the geological features.

As mentioned above, it should be emphasized that a correlation of ground deformation with a fault line does not necessarily mean that the fault is the direct cause of the observed deformation. A fault may also act as a geological “barrier” for, e.g., groundwater flow, either facilitating or hindering the extraction of water and, thus, potentially acting as a predisposing factor for subsidence. However, the overlap between ADAs and inactive faults does not necessarily indicate a correlation between the two, which can be observed in Figure 4.37 where fault lines are crossing some of the ADAs.

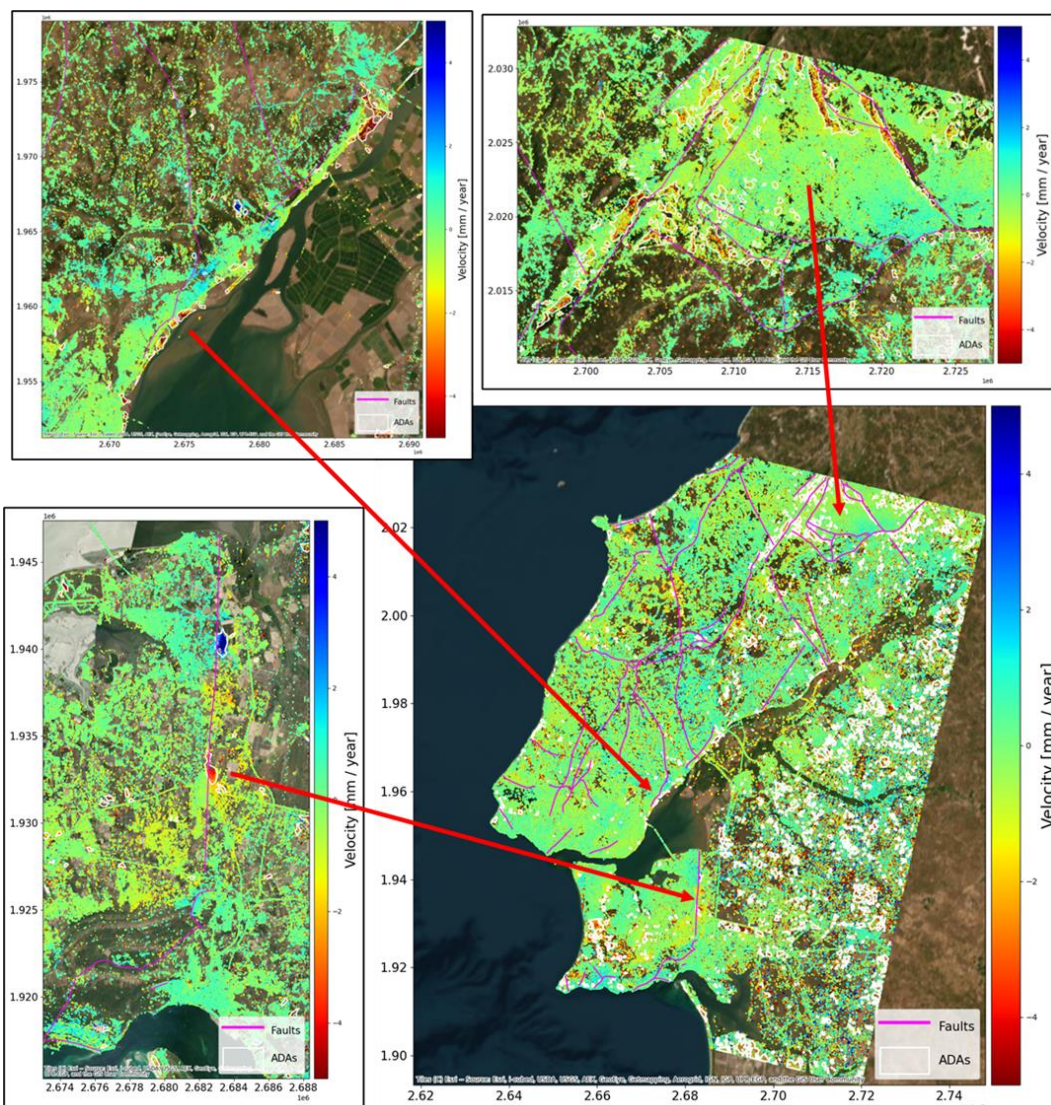


Figure 4.37: EGMS Basic/L2a velocity maps (ascending tracks 45 and 147) for the Tagus Valley highlighting fault lines (magenta) alongside detected ADAs (white polygons). Zoom-in views show the locations indicated by the red arrows.

Three additional datasets have been compared to EGMS: CLC, a geological map and topography. These datasets have been investigated for any unexpected correlations; however, none were observed.

*The comparison between detected ADAs and fault lines in the Tagus Valley shows some ADAs align with fault lines. Since these faults are not classified as sources of seismic activity, the EGMS displacements likely result from other factors like groundwater exploitation, with faults acting as geological barriers. Not all fault lines show a correlation with displacement, which is also expected considering that external deformation sources do not always align with fault lines.*

## 4.4 Groundwater exploitation

### 4.4.1 Comparison with geo-information

#### 4.4.1.1 Lorca (Spain)

Figure 4.38 presents the soft soil thickness dataset available for the Alto Guadalentín Valley, clipped at the 5 m thickness contour. The EGMS Ortho/L3 vertical displacement velocities and the derived ADAs are overlaid on the soft soil thickness map. The ADA closely aligns with the 5 m thickness contour, indicating a strong correlation between the soft soils thickness and measured subsidence velocity. This correlation is evident in the central region of the ADA, where thickness and subsidence rates are the highest, and near the southwest border of the ADA, where a slight increase in thickness coincides with an increase in subsidence rates.

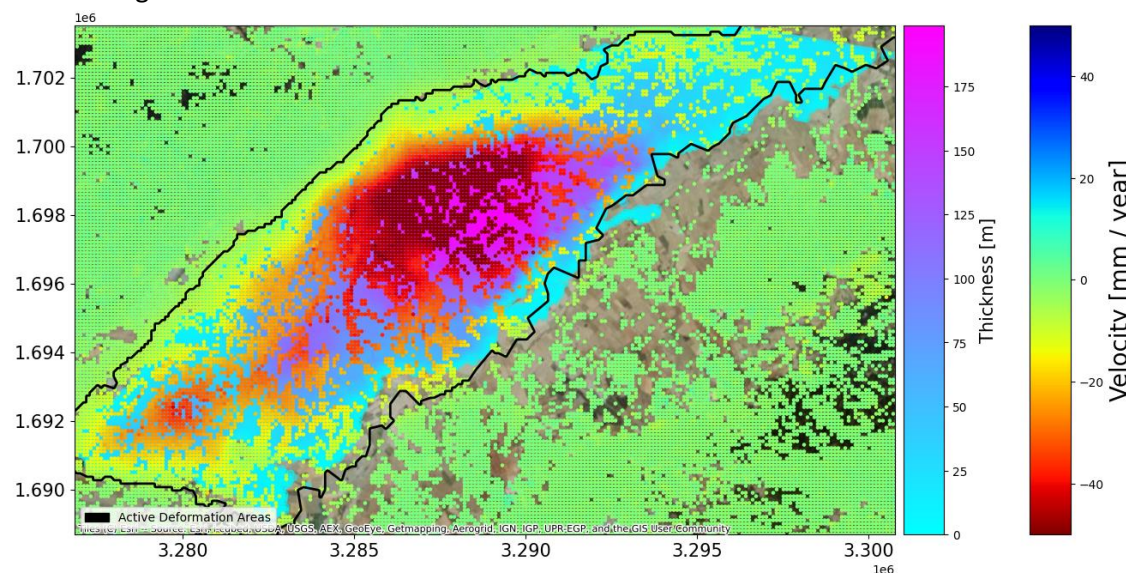


Figure 4.38: EGMS Ortho/L3 vertical and detected ADA (black line) co-plotted with soft soil thickness.

Figure 4.39 illustrates a comparison between the detected ADAs and the EGMS displacement velocities (Ortho/L3 vertical dataset) with a ground water model derived from piezometric levels (further assessed in the accuracy section 3.2.3).

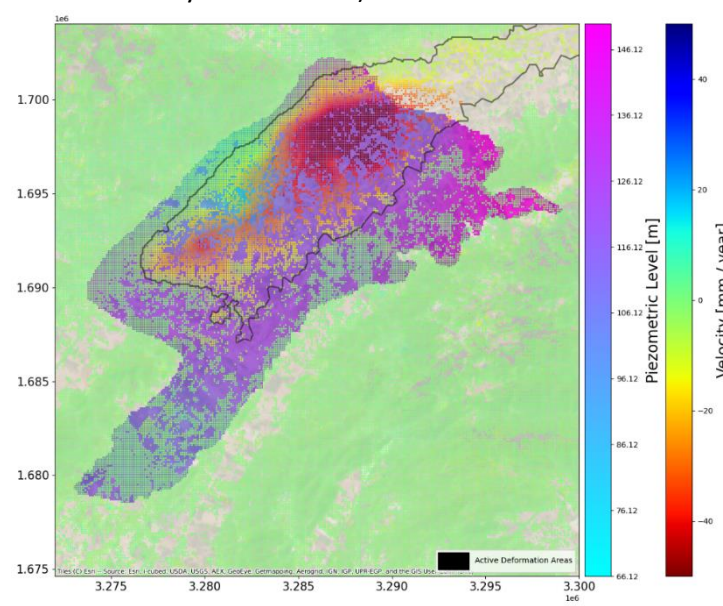


Figure 4.39: EGMS velocity maps from the Ortho/L3 vertical product compared with a ground water model represented by piezometric levels in the Lorca area.

It is worth highlighting that the groundwater model dates back to 2012, which is seven years prior the beginning of the EGMS time series. Despite this, subsidence patterns in the EGMS data should generally align with piezometric contours. Although there is a general correlation between the datasets, the highest piezometric levels and highest subsidence rates do not match spatially—the area with the lowest piezometric level lies just west of where maximum subsidence is observed in the EGMS data. This discrepancy could be attributed to the time gap between the ground water model and EGMS data or may indicate that variations in the soft soil thickness has more influence on displacement than piezometric levels.

Three additional datasets were compared to the EGMS products: CLC, groundwater well locations and topography. These datasets were investigated for any unexpected correlations; however, none were observed.

*The comparison of the EGMS products with ancillary geoinformation for the Lorca area shows the expected correlations. The most significant correlation is observed with soft soil thickness, indicating that this factor is likely primarily influencing the amplitude of the subsidence. The groundwater model also shows a correlation, although the peak values in both datasets are not perfectly aligned. Nonetheless, the analysis for Lorca clearly demonstrates the ability of the EGMS to accurately map ground displacements induced by groundwater extraction.*

## 4.5 Volcanism

### 4.5.1 Comparison with other GMS

#### 4.5.1.1 Etna Volcano (Italy)

For this analysis, IREA carried out a dedicated InSAR processing, providing all product levels for comparison with EGMS products. It is important to note that a large-scale continental processing strategy (EGMS) is being compared to a site-specific InSAR processing tailored to the phenomena of interest (IREA data). Figure 4.40 shows the comparison of Basic/L2a displacement velocities for ascending track 44, indicating a good spatial agreement between the datasets, despite differences in MP coverage, particularly in the crater region. The detected ADAs exhibit some degree of similarity.

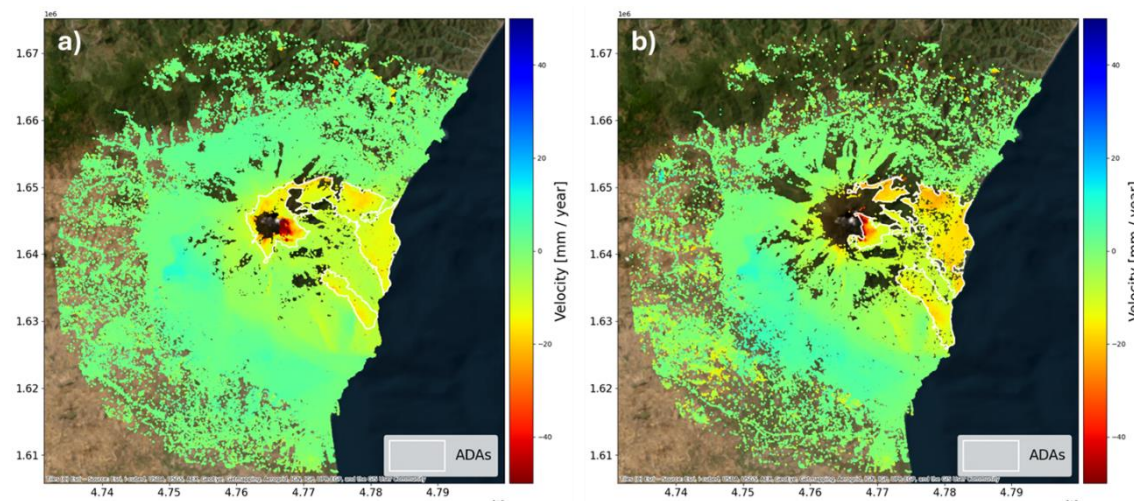


Figure 4.40: Comparison of EGMS velocities with those provided by IREA for the Basic/L2a ascending track 44: a) EGMS velocities; b) IREA velocities; ADAs are marked by white polygons.

Figure 4.41 displays a zoomed-in view of the eastern flank of the volcano. The map in Figure 4.41 c) shows that the subsidence rates in the IREA dataset are approximately 3-4 mm/year higher compared to the EGMS.

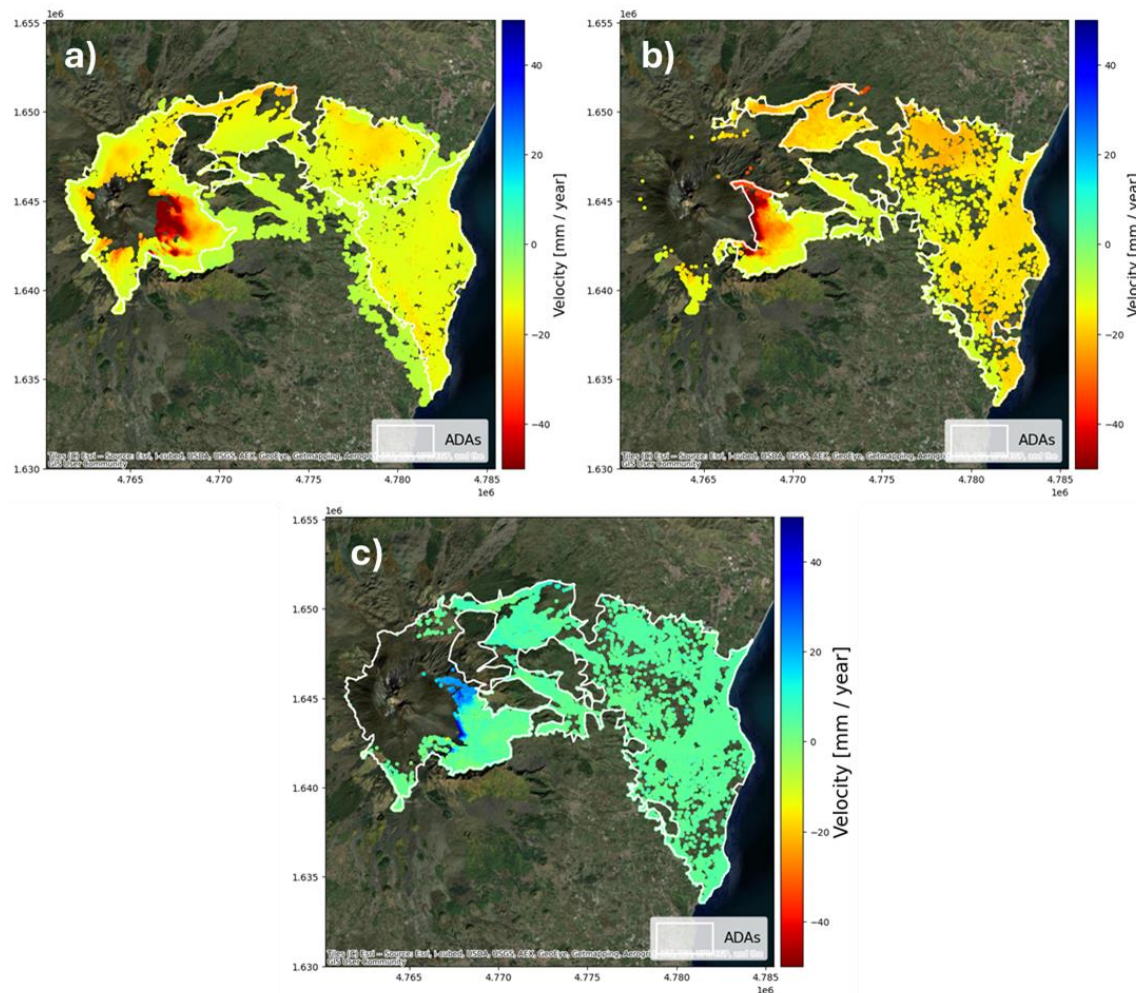


Figure 4.41: Detailed maps for the eastern ADA (white polygon) in Figure 4.40: a) EGMS velocities; b) IREA velocities; c) velocity difference (dvel = vel<sub>EGMS</sub> - vel<sub>IREA</sub>).

Figure 4.42a) presents the comparison of the averaged displacement time series for all MPs within the combined ADA area, obtained merging the ADAs detected in both datasets (Figure 4.41). The time series show a moderate level of similarity, with both datasets following the same overall trend. The IREA time series are shifted towards more negative displacement values, that aligns with the previously observed velocity offset. The IREA dataset moreover shows more pronounced short-term fluctuations compared to the EGMS time series. The velocity correlation plot in Figure 4.42 b) further confirms this, showing a nearly linear relationship for most MPs with a slight offset from the diagonal (red line), indicating the globally higher velocities observed in the ADA in Figure 4.41.

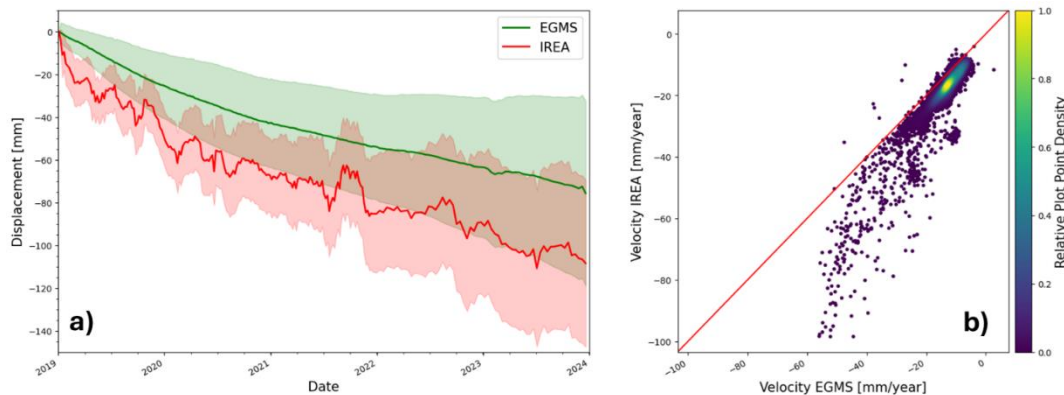


Figure 4.42: Time series and velocity correlation for measurement points within the ADA shown in Figure 4.41 - a) average and standard deviation of displacement time series; b) velocity correlation.

Table 4.7 provides a summary of the validation metrics (described in Table 2.6 and [D6-Validation Methodologies](#)) averaged across all products. The observed velocities are significantly high (>20 mm/year) for most parts of the volcano; for this reason, the velocity difference of 3-4 mm/year, that has been observed between EGMS and IREA, has a minimal impact on the “Relative Velocity Difference” metric (equal to 21%). Differences in spatial coverage of ADAs in the crater region do not significantly affect the spatial overlap measure, as the overlap is very good in the much larger area of the volcanic slopes. The metrics for velocity and time series correlation show very good agreement.

Table 4.7: Validation metrics for Etna.

Description	Value
Spatial overlap [%]	79.36
Relative Velocity Difference [%]	20.86
Velocity Correlation	0.90
Displacement Time Series Correlation	0.96

---

*Although the comparison of the EGMS and IREA products shows differences, the match between the datasets can still be regarded as very good for such a dynamic volcanic system. This demonstrates the EGMS’s capability to reliably map displacements under such challenging conditions.*

---



## 5 CONCLUSION

The **EGMS Validation Report** provides a comprehensive overview of the validation activities conducted for the EGMS 2019-2023 update. The validation exercise aimed to assess the agreement between EGMS products and various reference datasets, including ground-based measurements, GNSS, and other Earth Observation data. The report details the methodologies employed, discusses key results, and presents conclusions drawn from validation activities conducted at multiple sites across Europe.

The validation focused on two main objectives: assessing the consistency and accuracy of EGMS products and verifying their applicability and usability for across a range of applications. These objectives were addressed through two main validation components.

The validation activities were thus organized into two main activities:

- Validation for Consistency and Accuracy, which involved assessing the consistency and accuracy of key parameters such as displacement velocity, time series, and geolocation.
- Validation for Applicability and Usability, which focused on evaluating how well the EGMS products support various use cases and geohazard types, ensuring that the data are complete, coherent and fit for purpose.

The validation activities conducted demonstrate that the EGMS products meet the required technical specifications and are suitable for various applications related to ground motion monitoring and analysis.

EGMS data has shown good correlation with GNSS and CRs measurements, confirming the accuracy of velocity estimates and the ability of EGMS to capture seasonal variations, such as those induced by groundwater exploitation. Basic/L2a and Calibrated/L2b products have also proven particularly effective in delineating ground motion areas, particularly for landslide phenomena. Despite the low density of MPs in some areas due to vegetation cover, EGMS can detect landslides and accurately follow their evolution over time. These results highlight the importance of EGMS in improving national inventories and supporting efforts in geological risk management. Promising results have also been achieved in detecting motion induced by large-scale mining activities and post-mining effects. Finally, in urban areas, a high density of MPs has been obtained, effectively capturing significant man-made construction settlements.

In conclusion, the EGMS proves to be a valuable tool for monitoring ground motion in Europe, offering high-quality data and reliable accuracy for various geotechnical and geological applications.



## 6 REFERENCES

- Aslan G., Foumelis M., Raucoules D., de Michele M., Bernardie S., Cakir Z., 2020, « Landslide Mapping and Monitoring Using Persistent Scatterer Interferometry (PSI) Technique in the French Alps », *Remote Sensing*, 12(8), 1305
- Bonì, R., Cigna, R., Bricker, S., Meisina, C., McCormack, H., Characterisation of hydraulic head changes and aquifer properties in the London Basin using Persistent Scatterer Interferometry ground motion data, *Journal of Hydrology*, Volume 540, 2016, Pages 835-849, ISSN 0022-1694, <https://doi.org/10.1016/j.jhydrol.2016.06.068>.
- Brewer, C.A.; Marlow, K. A. Color representation of aspect and slope simultaneously, 11<sup>th</sup> International Symposium on Computer, Assisted Cartography (Auto-Carto-11), Minneapolis, Minnesota, 1983.
- Bru, G.; González, P.J.; Mateos, R.M.; Roldán, F.J.; Herrera, G.; Béjar-Pizarro, M.; Fernández, J. A-DInSAR Monitoring of Landslide and Subsidence Activity: A Case of Urban Damage in Arcos de la Frontera, Spain. *Remote Sens.* **2017**, *9*, 787. <https://doi.org/10.3390/rs9080787>.
- Cappello, A., Bilotta, G., Neri, M., & del Negro, C., 2013. Probabilistic modelling of future volcanic eruptions at Mount Etna. *Journal of Geophysical Research: Solid Earth*, 118, 1925–1935. <https://doi.org/10.1002/jgrb.50190>
- Carvalho, J., Pinto, C., Dias, R., Rabeh, T., Torres, L., Borges, J., Torres, R., Duarte, H., 2017. Tectonic Evolution of an Intraplate Basin: the Lower Tagus Cenozoic Basin, Portugal. *Basin Research*. 29. n/a-n/a. 10.1111/bre.12193.
- Cenni, N., Fiaschi, S., Fabris, M. Monitoring of Land Subsidence in the Po River Delta (Northern Italy) Using Geodetic Networks. *Remote Sens.* 2021, *13*, 1488. <https://doi.org/10.3390/rs13081488>
- Collilieux, X., Courde, C., Fruneau, B., Aimar, M., Schmidt, G., Delprat, I., Pesce, D., and Wöppelmann, G.: Radar corner reflector installation at the OCA Geodetic Observatory (France). In EGU General Assembly Conference Abstracts (p. 5201).
- Collilieux, X., Courde, C., Fruneau, B., Aimar, M., Schmidt, G., Delprat, I., Pesce, D., and Wöppelmann, G. (2022). Validation of a Corner Reflector installation at Côte d'Azur multi-technique geodetic Observatory. *Advances in Space Research*, 70(2), 360-370.
- Congalton, Russell. (2001). Accuracy assessment and validation of remotely sensed and other spatial information. *International journal of wildland fire*. 10. 321-328. 10.1071/WF01031.
- Del Soldato, M., Solari, L., Poggi, F., Raspini, F., Tomás, R., Fanti, R., Casagli, N. (2019) Landslide-Induced Damage Probability Estimation Coupling InSAR and Field Survey Data by Fragility Curves. *Remote Sensing* 2019, *11*(12), 1486; <https://doi.org/10.3390/rs11121486>
- Escolano Sánchez F, Bueno Aguado M, Melentijevic S (2019) Stress-strain behavior of blue marls from the Guadalquivir river basin in Spain. *Acta Geotechnica Slovenica* 16(1):30–42
- European Environment Agency, 2021. European Ground Motion Service (EGMS) Quality Assurance & Control Report – Harmonisation Tests. [land.copernicus.eu/user-corner/technical-library//quality-assurance-and-control-report-2013-harmonisation-test](http://land.copernicus.eu/user-corner/technical-library//quality-assurance-and-control-report-2013-harmonisation-test)
- Ezquerro, P., Tomás, R., Béjar-Pizarro, M., Fernández-Merodo, J.A., Guardiola-Albert, C., Staller, A., Sánchez-Sobrino, J.A. Herrera, G. Improving multi-technique monitoring using Sentinel-1 and Cosmo-SkyMed data and upgrading groundwater model capabilities. *Science of the Total Environment* 703 (2020) 134757 13
- Fabris, M, Achilli, V, Menin, A, Estimation of Subsidence in Po Delta Area (Northern Italy) by Integration of GPS Data, High-Precision Leveling and Archival Orthometric Elevations. *International Journal of Geosciences*, 2014, *5*, 571-585 <http://dx.doi.org/10.4236/ijg.2014.56052>
- Fabris, M., Battaglia, M., Chen, X., Menin, A., Monego, M., Floris, M., 2022. An Integrated InSAR and GNSS Approach to Monitor Land Subsidence in the Po River Delta (Italy). *Remote Sensing*. 14. 5578. <https://doi.org/10.3390/rs14215578>.
- Hauser, C., Kalströh, M., Karlsrud, K., Fosseide Boman, J.C., Guzman Sandoval, J., 2019. Effects from extensive construction activities on pore pressure and settlements in central Oslo. *Proceedings of the XVII ECSMGE-2019*. ISBN 978-9935-9436-1-3. [https://www.ecsmge-2019.com/uploads/2/1/7/9/21790806/0259-ecsmge-2019\\_hauser.pdf](https://www.ecsmge-2019.com/uploads/2/1/7/9/21790806/0259-ecsmge-2019_hauser.pdf)
- Heleno, S.I.N., Oliveira, L.G.S., Henriques, M.J., Falcão, A.P., Lima, J.N.P., Cooksley, G., Ferretti, A., Fonseca, A.M., Lobo-Ferreira, J.P., Fonseca, J.F.B.D., 2011. Persistent Scatterers Interferometry detects and measures ground subsidence in Lisbon. *Remote Sensing of Environment*, Volume 115, Issue 8, 2152-2167, ISSN 0034-4257, <https://doi.org/10.1016/j.rse.2011.04.021>.



Hermanns, R. L., Oppikofer, T., Böhme, M., Dehls, J. F., Molina, F. Y., & Penna, I. M. (2018). Rock slope instabilities in Norway: First systematic hazard and risk classification of 22 unstable rock slopes from northern, western, and southern Norway. In *Landslides and Engineered Slopes. Experience, Theory and Practice* (pp. 1107-1114). CRC Press.

Hofmann, R.; Sausgruber, J.T. Creep behaviour and remediation concept for a deep-seated landslide, Navistal, Tyrol, Austria, Geomechanics and Tunnelling 10 (2017), No. 1. <https://onlinelibrary.wiley.com/doi/10.1002/geot.201600066>.

Hungr, O., Leroueil, S. and Picarelli, L., 2014. The Varnes classification of landslide types, an update. *Landslides*, 11, pp.167-194.

Pereira, N., Carneiro, J.F., Araújo, A., Bezzeghoud, M., Borges, J. 2013. Seismic and structural geology constraints to the selection of CO<sub>2</sub> storage sites—The case of the onshore Lusitanian basin, Portugal, *Journal of Applied Geophysics*, 102, pp. 21-38, <https://doi.org/10.1016/j.jappgeo.2013.12.001>.

Pfeiffer, J., Zieher, T., Schmieder, J., Rutzinger, M. Strasser 2Hyndman, R., Newnham, G. & Culvenor, D. Spatio-temporal assessment of the Hydrological drivers of an active deep-seated gravitational slope deformation: The Voegelsberg landslide in Tyrol (Austria). *Earth Surf. Process. Landforms*. 2021;1–17.

Reyes-Carmona, C.; Barra, A.; Galve, J.P.; Monserrat, O.; Pérez-Peña, J.V.; Mateos, R.M.; Notti, D.; Ruano, P.; Millares, A.; López-Vinielles, J.; et al. Sentinel-1 DInSAR for Monitoring Active Landslides in Critical Infrastructures: The Case of the Rules Reservoir (Southern Spain). *Remote Sens.* 2020, 12, 809. <https://doi.org/10.3390/rs12050809>

Reyes-Carmona, C., Galve, J.P., Pérez-Peña, J.V. et al. Improving landslide inventories by combining satellite interferometry and landscape analysis: the case of Sierra Nevada (Southern Spain). *Landslides* **20**, 1815–1835 (2023). <https://doi.org/10.1007/s10346-023-02071-1>.

Cristina Reyes-Carmona; Jorge Pedro Galve; Anna Barra; Marcos Moreno-Sánchez; Oriol Monserrat; Adrian Riquelme; Teresa Teixido; Patricia Ruano; Agustín Millares; Roberto Sarro; Jose Vicente Perez-Pena; Pablo Ezquerro; Juan Lopez-Vinielles; Marta Bejar-Pizarro; Jose Miguel Azanon; Rosa Maria Mateos, Satellite Watching to Unstable Slopes for a Safe Water Management: The Case of the Rules Reservoir (Southern Spain), [Proceedings of the 39th IAHR World Congress \(Granada, 2022\)](https://doi.org/10.3850/IAHR-39WC2521711920221384), <https://doi.org/10.3850/IAHR-39WC2521711920221384>

Rosi, A., Tofani, V., Tanteri, L., Tacconi Stefanelli, C., Agostini, A., Catani, F., Casagli, N. (2018) The new landslide inventory of Tuscany (Italy) updated with PS-InSAR: geomorphological features and landslide distribution. *Landslides* 15, 5-19. doi: 10.1007/s10346-017-0861-4

Rouyet, L., Lilleøren, K. S., Böhme, M., Vick, L. M., Delaloye, R., Etzelmüller, B., ... & Blikra, L. H. (2021). Regional morpho-kinematic inventory of slope movements in northern Norway. *Frontiers in Earth Science*, 9, 681088.

Solari L, Del Soldato M, Raspini F, Barra A, Bianchini S, Confuorto P, Casagli N, Crosetto M (2020) Review of satellite interferometry for landslide detection in Italy. *Remote Sens* 12(8):1351. <https://doi.org/10.3390/rs12081351>

Teunissen, P. J. G. (2000a). Adjustment theory; an introduction (1 ed.). Delft: Delft University Press.,

Teunissen, P. J. G. (2000b). Testing theory; an introduction (1 ed.). Delft: Delft University Press.

Tsige M, Corral M (2013) Ángulo Estable y Tratamientos y Mejora de Taludes en las Arcillas Azules del Guadalquivir (AAG). VIII Simposio Nacional Sobre Taludes y Laderas Inestables, CIMNE, Barcelona, 3:997–1008, ISBN 978-84-941407-1-6 (in Spanish)

Varnes, D.J., 1978. Slope movement types and processes. Special report, 176, pp.11-33.

Vick, L. M., Berg, J. N., Eggers, M., Hormes, A., Skrede, I., & Blikra, L. H. (2021). Keynote Lecture: The Jettan Rockslide—An Engineering Geological Overview. Understanding and Reducing Landslide Disaster Risk: Volume 6 Specific Topics in Landslide Science and Applications 5th, 289-315.

Vradi, A., Sala, J., Solari, L., & Balasis-Levinsen, J. (2023). Validating the European Ground Motion Service: an assessment of measurement point density. *The International Archives of the Photogrammetry, Remote Sensing and Spatial Information Sciences*, 48, 247-252.



## 7 LIST OF ABBREVIATIONS

ADA	Active Deformation Area
AVGS	Aosta Valley Geological Survey
ASC	Ascending
ATTS	Automatic Tracking Total Station
BLUE	Best Linear Unbiased Estimation
CLC	Corine Land Cover
CLMS	Copernicus Land Monitoring Service
CR	Corner Reflector
CRS	Coordinate Reference System
IoA	Index of agreement
DEM	Digital Elevation Model
DESC	Descending
DSGSD	Deep-Seated Gravitational Slope Deformation
DTU	Technical University of Denmark
EEA	European Environment Agency
EGMS	European Ground Motion Service
GMS	Ground Motion Service
GNSS	Global Navigation Satellite System
InSAR	Interferometric Synthetic Aperture Radar
LOS	Line-of-Sight
MAE	Mean Absolute Error
MP	Measurement Point
OMT	Overall Model Test
PS / DS	Persistent Scatterer / Distributed Scatterer
R <sup>2</sup>	Coefficient of Determination
RDV	Regione del Veneto
RMSE	Root Mean Square Error
RT	Regione Toscana
S1	Sentinel-1
TS	Time Series



## 8 LIST OF FIGURES

Figure 2.1: Land cover and land use classes for Urban Atlas 2018 at the 12 sites selected to verify MP density.....	9
Figure 2.2: Global land cover type distribution over the 12 sites selected to verify MP density. ....	9
Figure 2.3: MP density over the 12 sites selected for specific UA18 classes based on the Basic/L2a and Calibrated/L2b products.....	10
Figure 2.4: EGMS 2019-2023 results – Comparison of ascending and descending Basic/L2a MP densities for the Urban Atlas classes over the selected 12 sites.....	11
Figure 2.5: EGMS MP density for Basic/L2a and Calibrated/L2b products across the 12 selected sites. The previous release 2018-2022 density values (grey) with the increase percentages in the current update (indicated by coloured bars and numerical labels). Land cover/land use classes from the Urban Atlas are grouped according to the 2 <sup>nd</sup> level of the CLC nomenclature. ....	11
Figure 2.6: Overview of the main components of the EGMS validation framework.....	12
Figure 2.7: Overview of the workflow used for EGMS and GNSS data comparison. ....	13
Figure 2.8: Distribution of the validation sites selected for the EGMS product consistency and accuracy assessment. ....	17
Figure 2.9: Distribution of the validation sites selected for the EGMS product applicability and usability assessment. ....	22
Figure 3.1: La Palma Island and location of the GNSS stations (basemap: Google). ....	26
Figure 3.2: Double differences comparison between pairs of stations for EGMS Basic/L2a ascending track 060.....	27
Figure 3.3: Double differences between pairs of stations with EGMS Basic/L2a descending track 069. ....	27
Figure 3.4 Single differences between GNSS and EGMS for Calibrated/L2b ascending track 060. ....	28
Figure 3.5: Single differences between GNSS and EGMS for Calibrated/L2b descending track 169. ....	28
Figure 3.6: Summary of all IoAs per station and EGMS products.....	29
Figure 3.7: Grand Canaria, in Spain, and GNSS stations distribution. (basemap: Google) .....	30
Figure 3.8: Examples of GNSS and EGMS time series used to assess velocity performance for Basic/L2a and Calibrated/L2b products. ....	31
Figure 3.9: Examples of GNSS and EGMS time series used to assess seasonality performance for Basic/L2a and Calibrated/L2b products. ....	32
Figure 3.10: Ortho/L3 products comparison in the E-W (top row) and Vertical direction (bottom row). ....	32
Figure 3.11: IoAs for Basic/L2a, Calibrated/L2b and Ortho/L3 EGMS products. ....	33
Figure 3.12: Lorca, in Spain, and the GNSS station distribution. (basemap: Google).....	34
Figure 3.13: Example of double differences between pairs of stations of Basic/L2a ascending and descending orbits. ....	35
Figure 3.14: Comparison between EGMS and GNSS for Calibrated/L2b ascending orbit 103. ....	35
Figure 3.15: Correlation between EGMS and GNSS velocity estimations for the three EGMS products along ascending track 103. ....	36
Figure 3.16: Correlation between EGMS and GNSS velocity estimations for the three EGMS products along descending track 088. ....	36
Figure 3.17: IoAs for Basic/L2a, Calibrated/L2b and Ortho/L3 products.....	37
Figure 3.18: Comparison between GNSS and EGMS for Ortho/L3 products in the vertical direction.....	38
Figure 3.19: The Jutland peninsula in Denmark and the distribution of GNSS stations (basemap: Google). ....	38
Figure 3.20: Double differences comparison between pairs of stations for EGMS Basic/L2a from ascending orbit (tracks 117 and 044). ....	39
Figure 3.21: Double differences comparison between pairs of stations for EGMS Basic/L2a from descending orbit (tracks 066 and 139). ....	40
Figure 3.22: Examples of double differences for Basic/L2a products, highlighting comparisons for ascending and descending orbits for the stations that did not pass the velocity statistical test. ....	40
The diagrams confirm previous observations about velocity differences. The correlations indicate a good agreement between GNSS and EGMS estimated velocities for most EGMS products and orbits, except for isolated stations (e.g. HIRS and BUDP). The highest velocity differences observed between EGMS and GNSS are around 2 mm/year for Basic/L2a products (see station HIRS Figure 3.23, Figure 3.21 and Figure 3.22) and about 3 mm/year for Calibrated/L2b products (see GESR station Figure 3.24 Calibrated/L2b descending track 066).....	41



Figure 3.24: Correlation between EGMS and GNSS velocities for the Basic/L2a and Calibrated/L2b EGMS products.	41
Figure 3.25: IoAs for all the EGMS products.	42
Figure 3.26: EGMS Basic/L2a ascending orbit (track 088) over Lorraine overlaid to the in-situ levelling stations available for validation shown in blue circles. (Basemap: OpenStreetMap).	44
Figure 3.27: Plot showing the mean velocity measured by the totality of levelling points against the mean value of EGMS update 2019-2023 MPs that fall within 50m of the in-situ data.	44
Figure 3.28: Plot showing the measurements (in cm/year) of eight different levelling stations distributed over the study site - Stations 10164 and 10043 are located in "Le Porcelette" area.	45
Figure 3.29: IoAs metrics for the comparison between levelling points average velocity and EGMS velocity for the MP falling inside the 50 m buffer of each station.	45
Figure 3.30: IoAs for time series comparison – 10 selected levelling stations are considered.	46
Figure 3.31: Comparison of in-situ levelling time series at station 5741 with EGMS Calibrated/L2b data for descending track 037.	46
Figure 3.32: Comparison of in-situ levelling time series at station 3156 with EGMS Calibrated/L2b data for descending track 037.	47
Figure 3.33: IoAs for the time series results for the Lorraine case study (In-situ levelling versus EGMS Basic/L2a, Calibrated/L2b and Ortho/L3 products).	47
Figure 3.34: Turow validation site showing the Calibrated/L2b EGMS product track 095, the piezometer position, and the 500-m buffer drawn around it.	48
Figure 3.35: IoAs for time series comparison of the 15 piezometers for Calibrated/L2b track 073.	48
Figure 3.36: Comparison between EGMS Calibrated/L2b measurements calculated along the ascending track 073 and in-situ piezometer time series TS5-H-3b.	49
Figure 3.37: Comparison between EGMS Calibrated/L2b measurements calculated along the ascending track 073 and in-situ piezometer time series TS12-H-9.	49
Figure 3.38: Comparison between EGMS Calibrated/L2b measurements calculated along the ascending track 073 and in-situ piezometer time series TS9-H-6.	49
Figure 3.39: Comparison between EGMS Calibrated/L2b measurements calculated along the ascending track 073 and in-situ piezometer time series TS4-H-3.	50
Figure 3.40: Indexes of Agreement for the time series results for Turow: Basic/L2a, Calibrated/L2b and Ortho/L3 compared to the in-situ piezometer dataset.	50
Figure 3.41: Lorca study case showing levelling, GNSS and piezometer positions.	51
Figure 3.42: IoAs for time series comparison of the 3 piezometers for the L3/Ortho.	51
Figure 3.43: Time series plot of piezometer number PA12213 against the EGMS Ortho/L3 MP.	52
Figure 3.44: Time series plot of piezometer number PA12272 against the EGMS Ortho/L3 MP.	52
Figure 3.45: IoA corresponding to the time series results for the Lorca case study (in-situ versus EGMS Ortho/L3 products).	52
Figure 3.46: EGMS Calibrated/L2a Descending track 168 MP distribution in Navis and position of the in-situ stations.	53
Figure 3.47: ATTS time series for station TS1 – PF5S (filtered data). Source: <a href="https://geoinformation.tirol.gv.at/client/?projekt=kerschbaumsiedlung">https://geoinformation.tirol.gv.at/client/?projekt=kerschbaumsiedlung</a> .	53
Figure 3.48: Indexes of Agreement for the velocity inter-comparison results in the Navis case study: Basic/L2a Calibrated/L2b and Ortho /L3 data.	54
Figure 3.49: Indexes of Agreement for the time series results in the Navis case study: Basic/L2a (descending orbit 168) compared with 5 total stations (H19, HK08, HK21, HK25, PF5S).	54
Figure 3.50: Comparison of in-situ TS1-PF5S time series against the against the EGMS Basic/L2a descending track 168.	55
Figure 3.51: Indexes of Agreement for the time series results in the Navis case study: Basic/L2a (ascending track 117) compared with 5 total stations (H19, HK08, HK21, HK25, PF5S).	55
Figure 3.52: Comparison of in-situ TS5-H19 time series against the against the EGMS Basic/L2a ascending track 117.	56
Figure 3.53: Indexes of Agreement for time series inter-comparison results in the Navis case study: Basic/L2a, Calibrated/L2b and Ortho/L3 data.	56
Figure 3.54: Map of the Thyborøn Peninsula with the eight corner reflectors (CRs) locations.	57
Figure 3.55: Example of time series and location of EGMS MPs around the 'LVS4' and 'LVS5' corner reflectors (CRs).	58



Figure 3.56: Example of time series and location of EGMS MPs around the 'RR18' (descending track 037) and 'RR14' (descending track 139) corner reflectors (CRs). ....	59
Figure 3.57: Correlation between EGMS and levelling velocities.....	60
Figure 3.58: Examples of time series displacements of stations with high velocity correlation between EGMS and levelling for ascending and descending orbits. ....	61
Figure 3.59: Examples of time series displacements of stations with low velocity correlation between EGMS and levelling time series for ascending and descending orbits. ....	61
Figure 3.60: Map of the Norwegian corner reflector (CR) site.....	62
Figure 3.61: Examples of time series double differences between three of the stations for Basic/L2a descending track 095. ....	63
Figure 3.62: Differences between the EGMS and the GNSS double differences time series. ....	64
Figure 3.63: Correlation between EGMS and GNSS velocities. ....	64
Figure 4.1: Displacement comparison for Aosta Valley (Italy): (a) Basic/L2a displacement velocities (EGMS, track 88/ASC); (b) AVGS displacement velocities. For the ADA marked by red arrows: (c) and (d) close-ups of corresponding velocity maps. ....	67
Figure 4.2: (a) Average and standard deviation of ADA time series for EGMS and AVGS for the ADA shown in Figure 4.1; (b) velocity correlation for area the same ADA.....	68
Figure 4.3: Displacement comparison for Tuscany (Italy): (a) EGMS Basic/L2a displacement velocities (track 168, descending); (b) RT displacement velocities. For the ADA marked by red arrows: (c) and (d) close-ups of corresponding velocity maps. ....	69
Figure 4.4: (a) Average and standard deviation time series calculated from all the MPs making the ADA represented in Figure 4.3c), for EGMS and RT; (b) velocity correlation for the same ADA. ....	70
Figure 4.5: EGMS Calibrated/L2b ADAs in descending orbit compared with updated national inventory (blue dots) on the French Alpes Maritimes department.....	71
Figure 4.6: EGMS Calibrated/L2b ADAs in descending orbit compared with updated national inventory (blue dots) on the French Alpes Maritimes department. ....	72
Figure 4.7: Basic/L2a ascending and descending Active Deformation Areas (green) and inventory polygons (orange). ....	73
Figure 4.8: Inventory polygons with 300m buffer and EGMS Calibrated/L2b MPs coverage for ascending (left) and descending (right) orbits (EGMS data 2019-2023). ....	74
Figure 4.9: Inventory polygon compared with the ADAs generated from EGMS MPs .....	74
Figure 4.10: Inventory versus EGMS Calibrated/L2b (a) descending, b) ascending and c) Ortho/L3_UD. ....	75
Figure 4.11: EGMS Basic/L2a velocity maps for ascending track 103 for La Unión, with detected ADAs marked as black polygons.....	76
Figure 4.12: EGMS Basic/L2a velocity maps obtained by combining descending tracks 8 and 110 for La Unión, with detected ADAs marked as black polygons. ....	77
Figure 4.13: ADAs superimposed on the Corine Land Cover (CLC) map for Basic/L2a products in ascending orbit. ...	77
Figure 4.14: ADAs superimposed on the Corine Land Cover (CLC) map for Basic/L2a products in descending orbit. .	78
Figure 4.15: Measured overlap of ADAs derived from Basic/L2a data with Corine Land Cover (CLC) categories in La Union.....	78
Figure 4.16: Basic/L2a Ascending (a) and Descending (b) EGMS ADAs versus mine waste land cover classes. ....	79
Figure 4.17: Measured overlap of ADAs with mine waste and tailings storage facilities. ....	79
Figure 4.18: EGMS Basic/L2a velocity maps for the ascending tracks 73, 102, and 175 for the Silesia area with detected ADA polygons. ....	80
Figure 4.19: EGMS Basic/L2a velocity maps for the descending tracks 51 and 124 for the Silesia area with detected ADA polygons. ....	81
Figure 4.20: Locations of mining-related areas (light green) plotted together with Basic/L2a ADA locations for (a) ascending tracks 73, 102, and 175, and (b) descending tracks 51 and 124 (white). ....	81
Figure 4.21: Comparison of Basic/L2a velocities from ascending track 15 for (a) the EGMS and (b) DTU-derived InSAR map; (c) velocity difference (dvel = vel EGMS – vel DTU). ADAs are marked by magenta polygons.....	83
Figure 4.22: (a) Comparison of mean and standard deviation for the time series in the ADA indicated in Figure 4.21 for ascending track 15; (b) velocity correlation for the same ADA. ....	83
Figure 4.23: Comparison of Basic/L2a velocities from descending track 37 for (a) the EGMS and (b) DTU-derived InSAR map; (c) velocity difference (dvel = vel EGMS – vel DTU). ADAs are marked by magenta polygons.....	84



Figure 4.24: (a) Comparison of mean and standard deviation for the time series in the ADA indicated in Figure 4.23 for descending track 37; (b) velocity correlation for the same ADA. ....	84
Figure 4.25: Comparison of displacement velocities for the Veneto validation site: (a) EGMS Basic/L2a ascending track 117; (b) Regione del Veneto GMS; (c) Velocity difference between (a) and (b). ....	86
Figure 4.26: Comparison of displacement velocities for the Veneto validation site: (a) EGMS Basic/L2a descending track 95; (b) Regione del Veneto GMS; (c) Velocity difference between (a) and (b). ....	87
Figure 4.27: Comparison of EGMS Basic/L2a ascending track 117 for an ADA in the Po River delta: (a) the EGMS and (b) RDV GMS; (c) location of ADA with EGMS velocities; (d) velocity difference (dvel = vel EGMS – vel RDV). ADA marked by magenta polygons. ....	88
Figure 4.28: (a) Comparison of mean and standard deviation for the timeseries in the ADA area indicated in Figure 4.27c; (b) velocity correlation for the same ADA. ....	88
Figure 4.29: EGMS Basic/L2a velocity maps for ascending tracks 44 and 146 (a) and descending tracks 37, 66, and 139 (b) for the Oslo area with detected ADA marked as pink polygons (Basemap: ESRI). ....	90
Figure 4.30: Histograms of Basic/L2a ascending velocity values computed from the 15 m x 15 m grid used for ADA detection: a) 2018-2022 EGMS update, b) 2019-2023 EGMS update. ....	90
Figure 4.31: Comparison of Corine Land Cover (CLC) with Basic/L2a ascending ADAs for the Oslo municipal region. (a) CLC with ADAs overlain; (b) Zoom-in of Oslo City region; (c) Zoom-in of Drammen region. ....	91
Figure 4.32: Corine Land Cover area (CLC) coverage with Active Deformation Areas (ADA). Colour bars represent different EGMS product levels. The measured values represent the overlap of ADAs with the respective CLC category in percentage of the ADA's total area. ....	92
Figure 4.33: Comparison of detected ADAs with the quaternary geology for the Oslo metropolitan area. The map shows the ADAs from the Basic/L2a ascending orbits in white overlaid on the quaternary geology (Basemap: ESRI) ....	93
Figure 4.34: Bar plot showing the overlap between detected ADAs and various geological unit. The coloured bars represent different EGMS product levels. The values indicate the percentage of each ADA's total area that overlaps with the corresponding geological unit. ....	93
Figure 4.35: ADAs (red polygons) detected in the EGMS Basic/L2a ascending product (all trackss combined) overlaid on a map of soft soil thickness. ....	94
Figure 4.36: Histograms of Basic/L2a ascending velocity values computed from the 30 m x 30 m grid used for ADA detection: a) 2018-2022 EGMS update, b) 2019-2023 EGMS update. ....	95
Figure 4.37: EGMS Basic/L2a velocity maps (ascending tracks 45 and 147) for the Tagus Valley highlighting fault lines (magenta) alongside detected ADAs (white polygons). Zoom-in views show the locations indicated by the red arrows. ....	96
Figure 4.38: EGMS Ortho/L3 vertical and detected ADA (black line) co-plotted with soft soil thickness. ....	97
Figure 4.39: EGMS velocity maps from the Ortho/L3 vertical product compared with a ground water model represented by piezometric levels in the Lorca area. ....	97
Figure 4.40: Comparison of EGMS velocities with those provided by IREA for the Basic/L2a ascending track 44: a) EGMS velocities; b) IREA velocities; ADAs are marked by white polygons. ....	98
Figure 4.41: Detailed maps for the eastern ADA (white polygon) in Figure 4.40: a) EGMS velocities; b) IREA velocities; c) velocity difference (dvel = vel <sub>EGMS</sub> – vel <sub>IREA</sub> ). ....	99
Figure 4.42: Time series and velocity correlation for measurement points within the ADA shown in Figure 4.41. a) average and standard deviation of displacement time series; b) velocity correlation. ....	100



## 9 LIST OF TABLES

Table 2.1: Quality criteria for the QC checks (see EGMS Quality Assurance and Control Report). ....	8
Table 2.2: IoAs defined for the validation by comparison with GNSS measurements. ....	14
Table 2.3: IoAs defined for the validation by comparison with in-situ measurements.....	15
Table 2.4: IoAs defined for the validation by comparison with CRs. ....	16
Table 2.5: Overview of validation sites (Consistency/Accuracy). ....	17
Table 2.6: IoAs defined for the validation by comparison with other GMSSs.....	20
Table 2.7: IoAs defined for the validation by comparison with inventories of phenomena. ....	21
Table 2.8: IoAs defined for the validation by consistency checks with ancillary data.....	21
Table 2.9: Overview of validation sites (Applicability/Usability). ....	22
Table 3.1: Probability estimation of each MP being the CR for 'LVS4' and 'LVS5' corner reflectors (CRs). MSE is the Mean Squared Error.....	58
Table 3.2: Probability estimation of each MP being the CR for 'RR18' and 'RR14' corner reflectors (CRs). ....	59
Table 4.1: Validation metrics for Aosta valley. ....	68
Table 4.2: Validation metrics for Tuscany. ....	70
Table 4.3: Summary of findings for Arcos de la Frontera landslides. ....	75
Table 4.4: Validation metrics for the Lorraine region. ....	76
Table 4.5: Validation metrics for Thyborøn, Denmark. ....	85
Table 4.6: Validation metrics for Po River Delta .....	89
Table 4.7: Validation metrics for Etna.....	100